

Referee #1: Referee's comments are in blue, authors' response is in black

We thank the referee for his comments that helped to significantly sharpen our manuscript. We fully implemented the suggested changes.

The following main changes were incorporated: Description of the semivariogram analysis was incorporated in the Methods Sect. (see below); REV analysis in the Results Sect. was extended by the semivariogram analysis, including the new figures (see comments 2, 6-8 below); the evaluation of the permeability tensors at the multiple sub-volumes of S3 and on the entire sample (comment 8) are discussed in the Discussion Sect. and included in Appendix C; Conclusions and Abstract are adjusted accordingly (see the details below),

- 1. Please use "semivariogram" instead of "variogram", or state in the text that you are using "variogram" to intend "semivariogram", as I will do from now on in this review.*

The “variogram” was changed to “semivariogram” throughout the entire manuscript as suggested.

- 2. Is the support used to compute the experimental variograms the whole image plane orthogonal to the computed direction? It is not completely clear to me at the moment. I find the Methods description misleading in this regard. If it's the case, I strongly advice to use for variography at least squares and not the full slices, and even better yet would be to do a full 3D variography, doing cubic supports as you did in the "classical" REV analysis of figure B1. Though, this is much more computationally intensive and may require ad-hoc coding. This may have a potentially large effect on the results, depending on the chosen "box side", especially for the sample S2, and if done properly also actually hint at the true principal axes of anisotropy for the samples, which may not be aligned with their sides.*

Methods Sect. was extended by description of the conducted semivariogram analysis (see lines 326-495). REV analysis in the Results Sect. was extended by the semivariogram analysis (lines 871-1788).

Sample sizes, at which the 1D porosity profiles in each x- y and z- direction are calculated and the semivariogram analysis is conducted, as indicated in lines 873, 1157, 1299 (Sect. 4.3.1), for S1, S3, and S2, respectively.

In addition, following your suggestion, we used multiple support sub-volumes of different sizes for S2, and evaluated them for the stationarity, variance and for the range of correlation (see lines 1571-1695 and Fig.19). Figure 9 was added for a 3D visualization of the CT segmented images of the samples.

As it was indicated previously, we did not calculate the semivariogram for 1D porosities in directions different from the main orthogonal axes of the cube. We made large efforts to take the samples in the field as accurate as possible to achieve a sub-sampling procedure in line with the visible foliation of the different layers (see lines 387-389). The evidence that the resulting “coordinate system” of the samples and of their images are in a very good alignment with the true principle axis of anisotropy, is presented by the exceptionally good results of measured and modelled permeability values and tensors (Table 2).

Accordingly, we have chosen the “less challenging” 2D variography path for our study, since we are familiar with all the features and textures of the rock samples' very well. The histogram variances and ranges are larger for z-direction (e.g. Figs.11-14, 17-18). Moreover, for the smaller sub-volumes, non-stationarity is also more apparent in z direction (Fig. 19). This confirms our initial assumption of the principal direction perpendicular to the deposition plane.

We believe that the application and comparison of results from the different variography methods is a big stand-alone topic. It will be of a great impact and thus deserves to be

addressed within a new topical manuscript applicable to samples with various (not known) directions of the principal anisotropy axes.

3. *Fig 9-11: if you are showing the fitted variograms, based upon which you define the apparent ranges, I believe you should also state which variogram model was fitted. From the legend I may assume it's an exponential model but or spherical or something else, and the "expo. fit". If it's the case, then you need to specify if the reported "range" is the actual coefficient in the exponential model or the "practical range" of the asymptotic function.*

Now the (nested) variogram models (see description in lines 377-386) and their corresponding calibrated sills and ranges are reported on the figure panels (e.g., Figs. 12, 14, 18).

4. *All three samples represents exemplary cases for zonal anisotropy, where the sills of the variograms are not constant following different directions. This reinforce my suggestion of making the samples available to the public.*

All data are available at the PANGÄA-repository as explained in the "Supplementary materials Sect. S1". The doi is also added at the end of the manuscript, lines 2302-2304.

5. *It is to me however striking - and this may hint to a too large support definition, cfr comment 2, or else to a graphical imprecision - that no experimental variogram displays any nugget effect. This could mean that the variable has been excessively regularised. Please state in the text how the lags for the calculation of the experimental variograms were chosen, and if the computed pairs at each lag bin are comparable.*

Obviously, the nugget effect can be attributed to measurement errors or spatial sources of variation at distances smaller than the sampling interval or both. Measurement error occurs because of the error inherent in measuring devices. Natural phenomena can vary spatially over a range of scales. Variations at microscales smaller than the sampling distances will appear as part of the nugget effect. Nevertheless, this is more or less impossible to achieve for "mining" spatial data from μ -CT images since we have a fixed resolution limit. Hence, all variation below that "hard resolution boundary" is "invisible" for the variography analysis. This clearly is a drawback of the image analysis, and hence it is important to gain detailed understanding of the scales of spatial variation from multiple methods. Accordingly, the smallest lags are related to the resolution, i.e. the smallest segmented feature of the 3D scan.

These issues are addressed in lines 338-342, 879, 1154, 1279, 1565.

6. *Fig 11. Regarding the variograms of sample S2, they are clearly linear, especially the xy plane, which is a clear sign of non-stationarity, as also clear from the strong trend in subfigure (c). However, you also correctly recognised the "external drift" represented by the clay content. This is possibly a textbook example of external drift, which makes the de-trending of porosity worth. My point here is that the fact that the sample is clearly strongly anisotropic and non-stationary does not mean that it is not possible to extract a REV from it, at least for the two other directions, but with some manipulation, also in the xy plane. Moreover, a full 3D variography (if my 2. comment is valid) may give different insights and results.*

New semivariogram analysis was conducted (see our response to the comment #2 above). Figures of slice-by-slice porosity 1D profiles were improved (Figs.11,13, 15). The trends in the data were modelled and removed, and the residuals are presented (Figs. 11, 17). The histograms of the 1D profiles are now presented (Figs.11,13, 17). Semivariograms (Figs. 12, 14, 18) were calculated from the standardized histograms.

Wherever hole-effect was identified, it was modelled as a part of a nested semivariogram model (e.g. Figs.12, 18).

7. *No histogram of apparent image porosity is displayed, neither from the slices used for the variographic REV nor from the subsets of figure B1, although from that figure we get an idea of the "density" (however there is sampling involved here, I assume). Is it possible that the "cube" porosity - at a given cube size - is also lognormally distributed? Possibly then it could be worth to perform the variographic analysis on a log porosity.*

The histograms of porosity are now added (see Figs. 11,13, 17). They show a normal distribution. Therefore, there is no need to calculate the semivariograms on log porosity.

8. *For sample S3 the REV is identified at 350 voxels, though only one permeability simulation is conducted. It would be nice to demonstrate that the calculated permeability is somewhat "continuous" by repeating the flow simulations on different subsets of that size of the original microCT image.*

These calculations were performed. The results demonstrating a “continuity” of permeability in the different REV sub-volumes and in the entire segmented volume are presented in Appendix C and addressed in lines 1942-1955, 2115-2120 in the Discussion Sect.

An outlook on relation of the spatial variability of structures (semivariogram range of correlation) at the different scales to the spatial distribution of local permeability connected to generation of preferential flow paths, is added (lines 2185-2200).

Response to the Referee #2:

We thank the reviewer for handling our manuscript. Our response to the specific comments is presented below:

General Comments

This paper has made commendable efforts to using a multi-scale, multi-methodological approach for the petrophysical characterization of reservoir sandstones. The strength of the study lies in its multiple datasets generated and used. However, the paper requires improvements before it can be ready for publication.

1.Comment:

*The main aims/objectives of this study should be made very clear from the start. Are you proposing **multi-methodological approach** for the petrophysical characterization of reservoir sandstones as the best or only **method**? Or what exactly are you aiming for?*

Response:

The objective of the paper is formulated in lines 106-107 in the introduction:

“The present paper provides a detailed description and evaluation of a **multi-methodological** petrophysical approach for the comprehensive multiscale characterization of reservoir sandstones.”

The word “**method**” questioned by the reviewer appears in lines 79 and 111 in the introduction in the following context:

Line 79: “Over the past few decades, pore-scale imaging and flow simulations (citations...) have started to serve as a reliable **method** for rock characterization.”

Line 111: “The suggested computational workflow enables the identification of Darcy-scale permeability links to an extensive set of geometrical, textural and topological rock descriptors, quantified at the pore scale by deterministic and probabilistic (statistical) **methods**.”

These **methods** are the parts of **the multi-methodological approach**, which is specified in lines 107-109 in the Introduction: “The proposed approach includes petrography, gas porosimetry and permeametry, mercury intrusion porosimetry, 3D imaging and image analysis, semivariogram analysis and flow modelling at the pore-scale.”

2.Comment:

How the achievement of these aims/objectives contribute to the current knowledge gaps should be clearly discussed in the relevant section of the paper.

Response:

This contribution of the objectives questioned above is presented in detail in the last paragraph of the introduction (lines 114-120):

“The approach presented herein is especially important for the detection of anisotropy and the identification of its origin at various rock scales. The multi-methodological validation procedure is significant for properly upscaling permeability from the micro scale to the macro scale (Ringrose and Bentley, 2015). This validation, thereby, allows an accurate petrophysical analysis of reservoir sandstones with broad ranges of textural and topological characteristics. The findings contribute also to the current geological knowledge regarding non-marine sandstones of Lower Cretaceous age (e.g., Akinlotan, 2016; 2017; 2018; Li et al., 2016; Ferreira et al., 2016) and specifically regarding the studied stratigraphic unit.”

Some aspects contributing to the current knowledge on anisotropy are added to the introduction (lines 87-105), and several more references in this and other context, are added to the revised version (lines 81-82, 86, 119, etc.).

3.Comment:

The methods need to be clearly discussed.

Response: Pls see our response to the comments #11 and #13 below.

4.Comment: *Many figures require attention.*

Response: The quality of all the figures is improved in the revised version of the paper.

5.Comment

I do feel that testing all the proposed conclusions made from this study with sandstones from other places will make these conclusions stronger. If it is possible to have sandstones from other places to test your conclusions, this will be very good. However, if the aims/objectives of the study do not require/permit this, then no problem.

Response:

In this paper we gathered an extensive data set quantified on various scales on the studied sandstones to benchmark the approach (from our objective). We do not have these data for other sandstones, to perform a valid benchmarking and comparison. However, we added some brief review on the relevant properties of non-marine sandstones of Lower Cretaceous age from other places to the Discussion Sect. (lines 2047-2062).

Specific Comments

6.Comment:

Title

Why is there 'benchmark' in the title? Depending on the revised aims/objectives of the study, the title may require revision.

Response:

Benchmarking is comparing results or processes with the “reference” data or processes. This is exactly what we perform in the paper for the upscaling task. Moreover, following the suggestions of Ref.1, this benchmarking was strengthened by performing a semivariogram analysis (lines 871-1695) and by the additional calculations of permeability on the various REV subvolumes of S3 and on the full sample, to show their continuity (lines 1942-1955, 2115-2120 and Appendix C). This strengthens the “benchmarking” content of the study even better than before and thus should remain in our title.

7.Comment:

Introduction

An extended literature review is required. This may be part of the introduction or may be a separate section. This is important to discuss the state of the subject matter and to present a framework and context for which current study fits into. The current introduction is short while the aim of this study does not seem to address some of the issues raised (lines 66-67) in previous studies.

Response: The introduction is extended by addressing some knowledge on anisotropy in sandstones (lines 87-105), and by adding several more references in this and other context (lines 81-82, 86, 119, etc.).

8.Comment:

Geological Setting

Abbreviation in line 98 needs to be written in full at first time.

Response: Fe-ox is changed to “Fe oxide (Fe-ox)” at the first occurrence (line 178).

9.Comment:

Fig. 1 needs to be increased in size to make it legible. The quality of 1d needs to be improved. 1a needs lines of latitude and longitude.

Response: These changes are implemented.

10.Comment:

Appendix A. It is a bit strange that important geological information is put in an appendix. The key geological information in the appendix needs to be summarized and placed under geological setting. The information presented in this section is too shallow and only focused on a formation. Every relevant geological information about the whole basin and other formations should be included here to give a very good context for the current study.

Response: The information that was provided in the former Appendix A is moved to the main text (see lines 141-171), following the request of the reviewer. However, to agree with the aim and the scope of the current manuscript (see our response to comment 6 above), we avoid from adding an extensive geological content to our paper.

11.Comment:

Methods

3.1. How many samples were collected? Is it possible to state the size of these samples and large block samples or show their photos so that readers can have an idea of how big/small they are. There needs to be proper descriptions of all these samples: how can a reader identify/differentiate a sample from large block samples and from a sub-sample?

Response: The reviewer is invited to look at lines 200-205 at the manuscript where the information about the number of samples is presented:

“Large sample blocks of **~10÷20 cm size** were collected from these three layers, and the directions perpendicular to the bedding planes (defined as the z-directions in our study) were noted. Subsequently, in the laboratory, smaller sub-samples (**described below**) were prepared from these large samples for textural observations and various analytical measurements and computations. In total, 7 sub-samples from the top layer, 8 sub-samples from the middle layer and 4 sub-samples from the bottom layer were investigated in the laboratory (Table 2).” The information about the number of samples for each test is also indicated in Table 2 and also below Table 2 in the legend.

With respect to the sample sizes: The approximate size of the largest blocks (10÷20 cm) is added to the manuscript (in bold above, line 200). However, all sample sizes and their shapes used for the specific measurements are specified in the manuscript:

Lines 210-212: “Specimens ~5-7 cm in size were investigated by petrographic and petrophysical lab methods. Sub-samples ~1 cm in size were retrieved from the aforementioned plugs for investigation by 3D imaging, digital image analysis and simulation techniques (described in more detail below).”

These sizes were repeated further in the manuscript at the descriptions of the specific measurements:

Lines 237-238: “Effective porosity and permeability were evaluated on dried cylindrical samples (2.5 cm in diameter and 5-7 cm in length)”

Lines 242-243: “Mercury intrusion porosimetry (...) was applied to dried cylindrical samples ~1 cm³ in size”

Lines 273-274: “cylindrical subsamples 4-8 mm in diameter and 5-10 mm in length were retrieved from the larger samples studied in the laboratory and were scanned...”.

Sample sizes for the semivariogram analysis are also specified in the text (see lines 873, 1157, 1299).

With respect to the photos suggested by the Reviewer: because of the big difference in the samples sizes (specified above) and because their dimensions are clearly and repeatedly specified in the paper, we did not insert their photos into the revised version of the manuscript.

12.Comment:

Table 1. 3.7 should be ‘Optical microscopy’

Response: Table 1, point 7 “Petrographic microscopy” is changed to the “Optical microscopy”

13.Comment:

3.2 The laboratory methods are not properly discussed and this is not good enough.

More than just mentioning the names of equipment used, the procedure needs to be properly discussed or appropriate references provided.

Response: Methods 1-7 specified in Table 1 are the “classical” ones with well-established protocols available elsewhere. We stated this more clearly in lines 213-217 and cited a basic comprehensive reference of *Practices for Core Analysis, API, (1998)*. We also added the additional references to some of the laboratory methods in lines 228, 235, 239, 243.

14.Comment:

If the methods are properly discussed, I do not see any need for Table 1. Only the relevant information needed to understand the procedure for the workflow method should be provided. The current format appears to be excessive.

Response: Extended computational workflow (number 8 in Table 1, Fig.2) is one of the main methodologies of our study. It combines several methods with some variability in their application which is not obvious (e.g., especially with respect to the methods of filtering, segmentation, and REV estimation). Despite this, some of these methods (Fig.2a-2c) are described in the text in very brief, e.g. see lines 271-289. REV estimation demands an especial attention in the current paper due to its importance for the anisotropy and inhomogeneity estimation (emphasized by Ref. 1 in his comment #2). Following this request, we added some explanations regarding the semivariogram analysis in lines 326-495 and also added this method to Table 1. Flow modelling could also be applied in several ways, with respect e.g., to the boundary conditions and to the averaging procedures. However, those are currently described in brief as well (lines 496-543). Image analysis description is very concise (lines 544-550). It contains a necessary information on algorithms and software that allows the reader to repeat the process using the data on our samples (available online, see Supplementary material for more detail).

The necessity of Table 1 is clarified in lines 564-566.

15.Comment:

Results Line 269, 314, -what heavy minerals?

Response: The clarifications are added in lines 582, 644.

16.Comment:

268, 270: referencing methods using 'according to', 'following' should be amended using journal style

Response: This paper was edited by the professional AJE editorial agency (certificate # 13B3-B361-ED59-44F5-4FB0, attached to this response) in accordance with SE journal style.

17.Comment:

276; Mn-Ox: what is this? Please explain?

Response: Mn-ox is the manganese oxide, which is clarified in the text in the same way as Fe-ox before (your comment #8), see line 589.

18.Comment:

317-include reference

Response: An appropriate reference with a classification of the “quartz wacke sandstone” (Pettijohn et al., 1987) is included in line 647.

19.Comment:

318: result is mixed with interpretation. Only the results should be presented in the result section in this place and throughout the manuscript.

Response: The sentence “The pore network is influenced by the extent of clay deposition on coarser grains, identified mostly in laminae (Fig. 4a, d).” is substituted by “The pore space is reduced by clays deposited on coarser grains, identified mostly in laminae (Fig. 4a, d)”, see lines 648-649.

20.Comment:

Fig 4d-scale is missing

Response: The scale is added

21.Comment:

347-349 should be moved to the methods section

Response:

To agree with the corresponding descriptions of the top and intermediate unit layers in the Results section:

“**Sandstone S1:** The top unit layer with a thickness of ~1.5 m (Fig. 1c) consists of yellow-brown sandstone (Fig. 3a), which is moderately consolidated ...” (lines 580-581)

“**Sandstone S2:** The intermediate unit layer with a thickness of ~20 cm consists of grey-green moderately consolidated sandstone (Figs. 1c, 4) ...” (lines 640-641),

the following sentence for the bottom unit layer, addressed by the referee:

“**Sandstone S3:** Samples were taken from the ~1.5 m thick bottom unit layer in the outcrop (Fig. 1c) consisting of (pale) red-purple poorly consolidated sandstone with grains covered by a secondary red patina (Fig. 5).” (former lines 347-349)

are changed to:

“The bottom unit layer with a thickness of ~1.5 m consists of (pale) red-purple poorly consolidated sandstone (Fig. 1c) with grains covered by a secondary red patina (Fig. 5).”, see lines 693-694.

22.Comment:

Fig 6 and 7, 9, 11, 12 should be increased

Response: The quality of all the figures in the manuscript is improved

23.Comment:

480-485: more or less a repetition. Any new information here should be moved to methods section. The results of the modelling should be presented here.

Response: The questioned text from the lines 480-483 in the former version of our ms is presented below:

“Fluid flow was modelled at the pore scale in two different micro-CT-scanned geometries: 1) a full cube of sample S1, including two adjacent parts possessing relatively low (0-250 voxels) and high (250-1180 voxels) porosities (Fig. 9c), and 2) sample S3 within its REV dimensions (Table 3). Modelling of the 3D geometry of sample S2 was not performed due to the reasons detailed above.”

The new text is presented in lines 1797-1800. Please note that the domain size for the flow modelling relies on the results of the conducted REV analyses (including the new semivariogram analysis suggested by Ref.1).

The following sentence “A constant pressure gradient of 2.424 [Pa / mm] between the inlet and outlet boundaries was applied in all the simulations for consistency.” is moved to the Methods to the description of the flow modelling (lines 504-506).

24.Comment:

509-511: needs to be in the methods section

Response: The questioned text in lines 509-511 of the former version, is presented below: “For S1, the mode peak of the pore size distribution (measured by a Feret maximum calliper) (Fig. 13, red line) is at 194 μm (Table 2). In total, 3500 pores were analysed. The pore specific surface area (PSA) calculated from micro-CT images is 0.068 μm^{-1} .”

The number of the analyzed pores is the direct result of application of the image analysis (see lines 544-550 in Methods section). Now the number of the derived pores is specified in the caption to Fig.10. All other parameters derived by image analysis are presented in lines 784-788.

25.Comment:

513-514: is this result or interpretation?

Response:

“The tortuosity, measured from the whole CT image, indicates similar values in the x- and y-directions of 1.37 and 1.38, respectively, whereas in the z-direction, the tortuosity is 1.48 (Table 2). As many paths were considered, we suggest that this difference is created by the textural features that appear in horizontal planes (Fig. 3a).”

Both sentences include the results of the conducted image analysis indicating an anisotropy. The second sentence is changed to “As many paths were considered, this difference is an indication of the textural features that appear in horizontal planes (Fig. 3a).”, see lines 789-791.

26.Comment:

545: if the information in appendix C is important for the discussion, why is it not included in the main body of the manuscript?

Response:

Former Appendix C presented the definition of the Euler characteristic available elsewhere and used in our image analysis, with some clarification. It was excluded from the Methods section in order to reduce the text related to the image analysis (see comment #14 above and our response). In addition, because there is also no need to insert this “basic” definition to the Discussion, we decided to place this brief text to the Supplementary material and to refer to it from the main text (see lines 558, 1856).

27.Comment:

560: gravity-dominated?, capillary-dominated?

Response: SE English guidelines do not allow using hyphens in the specified grammar context: https://www.solid-earth.net/for_authors/manuscript_preparation.html

28.Comment:

601: use 'study' instead of paper, here and throughout the manuscript

Response: This was changed throughout the text where applicable

29.Comment:

603: 'very heterogeneous in nature'?

Response: Changed, see line 2039.

30.Comment:

References

I have not bothered to check the references at this stage. The author needs to ensure that all cited references are in the bibliography and vice. For example, I am not sure if I encountered Akinlotan 2018 in the text but it is in the bibliography. Please look into this and others and ensure referencing is accurate.

Response: The list of the reference was verified and adjusted accordingly in the revised version of our manuscript.

1 **Benchmark study using a multi-scale, multi-methodological approach for the**
2 **petrophysical characterization of reservoir sandstones**

3
4 Peleg Haruzi^{1,2}, Regina Katsman¹, Matthias Halisch³, Nicolas Waldmann¹, and Baruch Spiro^{1,4}

5
6 ¹The Dr. Moses Strauss Department of Marine Geosciences, Faculty of Natural Sciences, The University of
7 Haifa, Haifa, Mount Carmel 3498838, Israel

8 ²Agrosphere Institute, IBG-3, Institute of Bio- and Geosciences, Forschungszentrum Jülich GmbH, Germany

9 ³Leibniz Institute for Applied Geophysics, Dept. 5 – Petrophysics & Borehole Geophysics, Stilleweg 2, D-
10 30655 Hannover, Germany

11 ⁴Department of Earth Sciences, Natural History Museum, Cromwell Road, London SW7 5BD, UK

12
13
14 Correspondence to: Regina Katsman (rkatsman@univ.haifa.ac.il)

15 Matthias Halisch (Matthias.Halisch@leibniz-liag.de)

16
17
18
19 **Keywords:** multi-methodological approach, permeability, petrography, petrophysics, 3D imaging, pore-scale
20 modelling, upscaling, [semivariogram modelling](#), benchmark study.

21

Abstract

This paper presents a detailed description and evaluation of a multi-methodological petrophysical approach for the comprehensive multiscale characterization of reservoir sandstones. The suggested methodology enables the identification of Darcy-scale permeability links to an extensive set of geometrical, textural and topological rock descriptors quantified at the pore scale. This approach is applied to the study of samples from three consecutive sandstone layers of Lower Cretaceous age in northern Israel. These layers differ in features observed at the outcrop, hand specimen, petrographic microscope and micro-CT scales. Specifically, laboratory porosity and permeability measurements of several centimetre-sized samples show low variability in the quartz arenite (top and bottom) layers but high variability in the quartz wacke (middle) layer. The magnitudes of this variability are also confirmed by representative volume sizes and by semivariogram analyses conducted on micro-CT-imaged 3D pore geometries. Two scales of porosity variability are revealed by applying a semivariogram analysis to quartz arenite sandstone of the top layer: the pore size scale of $\sim 100\text{ }\mu\text{m}$, and $\sim 1.6\text{ mm}$ scale due to the occurrence of high- and low-porosity horizontal bands occluded by Fe oxide cementation. This millimetre-scale variability is found to control the laboratory-measured macroscopic rock permeability. More heterogeneous pore structures were revealed in the quartz wacke sandstone of the intermediate layer, which comprises an internal spatial irregularity at the different scales: at the pore size scale and at the larger scale of porous “lenses” originated in presence of patchy clay deposition. Quartz arenite sandstone of the bottom layer shows stationarity and isotropy in the investigated domain revealing porosity variability at a $\sim 0.1\text{ mm}$ scale, which is associated with the average size of pore cross-section. Good agreement between the permeability upscaled from the pore-scale modelling and the estimates based on laboratory measurements is shown for the quartz arenite layers. The proposed multi-methodological approach leads to an accurate petrophysical characterization of reservoir sandstones with broad ranges of textural, topological and mineralogical characteristics and is particularly applicable for describing anisotropy at various rock scales. The results of this study also contribute to the geological interpretation of the studied stratigraphic units.

Deleted: spatial variability

Deleted: statistical anisotropy

Deleted: variogram

Deleted: the

Deleted: about

Deleted: 1.

Deleted: 6

Deleted: 1-2 mm due to depositional processes by influencing on high- and low-porosity bands in quartz sandstone and deposition clay in patch structure wacke sandstone. fluctuations at $150\text{ }\mu\text{m}$ are due to variability in the pore size, and those at 2 mm are due to the occurrence of high- and low-porosity bands occluded by iron oxide cementation.

Deleted: (top)

62 **1. Introduction**

63 Permeability is an effective property of a reservoir rock that varies enormously over a wide range of
64 rock length scales, attributed to a hierarchy of dominant sedimentary depositional features (Norris and Lewis,
65 1991; Nordahl and Ringrose, 2008; Ringrose and Bentley, 2015). Permeability should thus be properly
66 upscaled through the following sequence of scales (Nordahl and Ringrose, 2008; Ringrose and Bentley, 2015
67 and references therein): (1) from the pore scale (the micro scale, typically microns to millimetres) to the
68 representative elementary volume of a single lamina (the macro scale, typically millimetres to centimetres,
69 e.g., Wildenschild and Sheppard, 2013; Andrä et al., 2013b
70 ; Bogdanov et al., 2011; Narsilio et al., 2009); (2) to the scale of geological heterogeneity, e.g., the scale of a
71 stratigraphic column (decimetres to decametres, e.g., Jackson et al. 2003; Nordahl et al. 2005); and (3) to the
72 field scale or the scale of an entire reservoir or aquifer (hundreds of metres to kilometres) (Haldorsen and Lake
73 1984; Rustad et al., 2008). Pore scale imaging and modelling enable us to relate macroscopic permeability to
74 basic microscopic rock descriptors (Kalaydjian, 1990; Whitaker, 1986; Cerepi et al., 2002; Haoguang et al.,
75 2014; Nelson, 2009). Therefore, the first stage in the above sequence is crucial for successful upscaling to the
76 final reservoir scale permeability.

77 Over the past few decades, 3D pore scale imaging and flow simulations (Bogdanov et al., 2012; Blunt
78 et al., 2013; Cnudde and Boone, 2013; Wildenschild and Sheppard, 2013; Halisch, 2013a) have started to
79 serve as a reliable method for rock characterization. The advantages of these techniques are their non-
80 destructive character and their capability to provide reliable information about the real pore-space structure
81 and topology of rocks that is impossible to obtain using the conventional experimental methods (e.g., Arns et
82 al., 2007; Knackstedt et al., 2010; Blunt et al., 2013). However, despite its importance, the upscaling from the
83 pore scale is sometimes omitted; as a result, effective petrophysical rock characteristics (e.g., porosity, surface
84 area, and permeability) are often evaluated at the macro scale through only conventional laboratory
85 experiments, which often suffer from errors due to local heterogeneities, anisotropy, or an insufficient number
86 of samples (e.g., Meyer, 2002; Halisch, 2013a).

87 Digital 3D micro scale core analysis should also become a necessary technique for rocks that are
88 difficult to characterize due to various reasons (e.g., for tight sandstones, Liu et al., 2017; Du et al., 2018;
89 Munawar et al., 2018; Zhang et al., 2019), or for those with inhomogeneous or anisotropic pore space (e.g.,

Deleted: a or

Deleted: ???

Deleted: -

Deleted: -

Deleted: -

Deleted: .

Deleted:

Deleted: small

Deleted:

99 [Meyer, 2002; Farrel et al., 2014](#)). Preferential fluid flow pathways are inherently connected to rock
100 microstructure, formed by depositional sedimentary structures such as pore shapes and their preferential
101 orientation (Sato et al., 2019) or lamination (Lewis et al., 1988). Those can be modified with time by
102 dissolution of grains, by grain rearrangement and pore collapse (Halisch et al., 2009; Clavaud et al., 2008), by
103 cementation (Louis et al., 2005), or by deformation structures (fractures). The later may drastically alter the
104 host rock depositional porosity pattern and create new permeability pathways (Zhu et al., 2002; Farrel et al.,
105 2014).

106 The present paper provides a detailed description and evaluation of a multi-methodological
107 petrophysical approach for the comprehensive multiscale characterization of reservoir sandstones. The
108 proposed approach includes petrography, gas porosimetry and permeametry, mercury intrusion porosimetry,
109 3D imaging and image analysis, semivariogram analysis and flow modelling at the pore-scale. The suggested
110 computational workflow enables the identification of Darcy scale permeability links to an extensive set of
111 geometrical, textural and topological rock descriptors, quantified at the pore scale by deterministic methods.
112 Ultimately, this approach is applied to the study of three different consecutive sandstone layers of Lower
113 Cretaceous age in northern Israel.

114 The approach presented herein is especially important for the detection of anisotropy and the
115 identification of its origin at various rock scales. The multi-methodological validation procedure is significant
116 for properly upscaling permeability from the micro scale to the macro scale (Ringrose and Bentley, 2015).
117 This validation, thereby, allows an accurate petrophysical analysis of reservoir sandstones with broad ranges
118 of textural and topological characteristics. The findings contribute also to the current geological knowledge
119 regarding non-marine sandstones of Lower Cretaceous age (e.g., Akinlotan, 2016; 2017; 2018; Li et al., 2016;
120 Ferreira et al., 2016) and specifically regarding the studied stratigraphic unit.

121

122 2. Geological setting

123 The study is based on samples collected from a steep outcrop at Wadi E'Shatr near Ein Kinya on the
124 southern slopes of Mt. Hermon (Figure 1). The outcrop consists of sandstones from the Lower Cretaceous
125 Hatira Formation (Sneh and Weinberger, 2003). This formation (Fm.) acts as a reservoir rock for hydrocarbons
126 in Israel (Figure 1a), both onshore, namely, Heletz (Grader and Reiss, 1958; Grader, 1959; Shenhav, 1971,

Deleted: ss

Deleted: at the pore-scale

Deleted: and

Deleted: characterising pore network, spatial variability investigation using semivariogram calculations, and several kinds of pore-scale modelling flow modelling at the pore-scale.

Deleted: -

Deleted: and probabilistic (statistical)

Deleted: 2017

Deleted: Fig.

Deleted: Fig.

138 ~~Calvo, 1992; Calvo et al., 2011~~), and offshore, namely, Yam Yafo (Gardosh and Tannenbaum, 2014; Cohen,
139 1971; Cohen, 1983;).

140 The Hatira Fm. is the lower part of the Kurnub Group of Lower Cretaceous (Neocomian – Barremian)
141 age. ~~The Hatira Fm. nomenclature used in Israel and Jordan is equivalent to Grès de Base in Lebanon~~
142 ~~(Massaad, 1976). This formation occurs in Israel in outcrops from the Eilat area along the rift valley, in the~~
143 ~~central Negev, and in the northernmost outcrops on Mount Hermon; it forms part of a large Palaeozoic –~~
144 ~~Mesozoic platform and continental margin deposits in northeastern Africa and Arabia. The Hatira Fm. consists~~
145 ~~of siliciclastic units, typically dominated by quartz-rich sandstones (Kolodner et al., 2009 and references~~
146 ~~therein). The underlying Palaeozoic sandstones cover large areas in North Africa and Arabia from Morocco~~
147 ~~to Oman; these sandstones overlie a Precambrian basement affected by Neoproterozoic (pan African)~~
148 ~~orogenesis (Garfunkel, 1988, 1999; Avigad et al., 2003, 2005). The lower Palaeozoic sandstones in Israel and~~
149 ~~Jordan originated from the erosion of that Neoproterozoic basement, the Arabian-Nubian Shield, with~~
150 ~~contributions from older sources. These lower Palaeozoic sandstones (Cambrian and Ordovician) are~~
151 ~~described as first-cycle sediments (Weissbrod and Nachmias, 1986; Amireh, 1997; Avigad et al., 2005).~~
152 ~~Exposures of the Hatira Fm. in the Central Negev, the Arava Valley, Eilat and Sinai were originally defined~~
153 ~~as the Wadi (Kurnub) Hatira Sandstone (Shaw, 1947). The largely siliciclastic section of the Hatira Fm. is~~
154 ~~intercalated with carbonates and shales representing marine incursions that increase towards the north~~
155 ~~(Weissbrod, 2002).~~

156 The Lower Cretaceous sandstones of the Kurnub Group are described as super mature, cross-bedded,
157 medium- to fine-grained, moderately sorted to well-sorted quartz arenites with a high zircon-tourmaline-rutil
158 (ZTR) index (for more details, see Kolodner, 2009). Earlier observations indicate the relatively scarce
159 occurrence of siltstones and claystones compared to sandstones (Massaad, 1976; Abed, 1982; Amireh, 1997).
160 These Lower Cretaceous sandstones are mainly the recycled products of older siliciclastic rocks throughout
161 the Phanerozoic; the sand was first eroded from the surface of the pan African orogeny ca. 400 Ma prior to its
162 deposition in the Lower Cretaceous sediments (Kolodner et al., 2009).

163 The Mount Hermon block was located at the southern border of the Tethys Ocean during the Early
164 Cretaceous (Bachman and Hirsch, 2006). A paleo-geographical reconstruction indicates that the sandy Hatira
165 Fm. (Figure 1) was deposited in a large basin, which included both terrestrial and coastal environments such

Moved (insertion) [5]

Deleted: ???

Moved up [5]: Calvo, 1992???; Calvo et al., 2011

Deleted: Fig.

169 as swamps and lagoons (Sneh and Weinberger, 2003). The Hermon block, located next to the Dead Sea
170 Transform, was rapidly uplifted during the Neogene (Shimron, 1998). The area is marked by intense erosion,
171 which resulted in extensive outcrops such as those near Ein Kinya on the southeastern side of Wadi E'Shatr.

172 The Kurnub Group in the study area (Figure 1b, d) consists of a volcanic sequence at its base that is
173 overlain with an angular unconformity by sandstone and clay layers of the Hatira Fm.; the upper unit consists
174 of limestone, marl and chalk – the Nabi Said Fm. (Sneh and Weinberger, 2003). At the section of Saltzman
175 (1968), which is approximately 100 m SW of the sampling area of the present study, the 58 m thick variegated
176 sandstone is interbedded with layers of clay and clay-marl. The sandy component is white-yellow-brown/red
177 and consists of largely angular, poorly sorted, fine- to coarse-grained quartz sand. Individual sandstone layers
178 are cemented by Fe oxide (Fe-ox). The outcrops show lenticular benches 0.2 m -1.0 m thick. The clay-rich
179 interlayers are grey and normally silty and brittle. Locally, these layers contain lignite. The outcrop
180 investigated and the specific beds sampled in the present study are shown in Figure 1c.

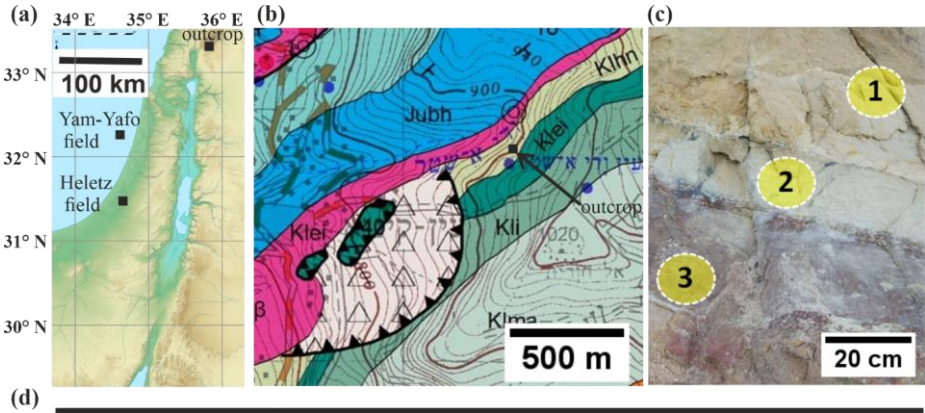
Deleted: Fig.

Deleted: 2004

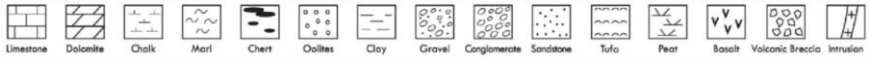
Deleted: ??

Deleted: 1967

Deleted: The wider geological context of the Hatira Fm. is presented in Appendix A.



SERIES - STAGE		SYMBOL	THICK. m	LITHOLOGY	LITHOSTRATIGRAPHY	
					MAPPING UNITS	GROUP
LOWER CRETACEOUS	APTIAN	Kli	45		Hidra Formation	JUDEA
		Klei			Ein El Assad Formation	
	NEOCOMIAN-BARREMIAN	Kln + Klih	85		Hatira & Nabi Sa'id formations	KURNUB
		imvb Kliβ			Volcanic sequence: basaltic flows, pyroclastics & lacustrine sediments	
JURASSIC	OXFORDIAN	Jubh	225		Be'er Sheva & Haluza formations	ARAD
		Juk	110		Kidod Formation	



187
 188 **Figure 1: Geographical and geological settings.** (a) Schematic relief map of Israel, (modified from www.mapsland.com).
 189 (b) Geological map of Ein Kinya. The Hatira Fm. sandstone and the overlying limestone and marl of the Nabi Said Fm.

Deleted: .

191 *are marked as Kln (map is adopted from Sneh and Weinberger, 2014). (c) Outcrop of the Lower Cretaceous Hatira Fm.*
192 *sandstones (Kln) at Ein Kinya. The studied sandstone layers have distinct colours: yellow-brown (1), grey-green (2),*
193 *and red-purple (3). (d) Stratigraphic table of the geological map (modified from Sneh and Weinberger, 2014).*

194 3. Methods

195 3.1. Sample description

196 Samples were extracted from three consecutive layers of different colours from a stratigraphic sequence
197 (Figs. 1c, 1d). The lower layer (3) is ~1.5 m thick and consists of sandstone that is light (pale) red-purple in
198 colour with undulating bedding planes between the sub-layers. The middle layer (2) is composed of grey –
199 green shaly sandstone that is 20 cm thick with dark horizons at the bottom and top. The upper layer (1)
200 comprises 1.5 m thick homogenous brown-yellow sandstone. Large sample blocks of ~10÷20 cm size were
201 collected from these three layers, and the directions perpendicular to the bedding planes (defined as the z-
202 directions in our study) were noted. Subsequently, in the laboratory, smaller sub-samples (described below)
203 were prepared from these large samples for textural observations and various analytical measurements and
204 computations. In total, 7 sub-samples from the top layer, 8 sub-samples from the middle layer and 4 sub-
205 samples from the bottom layer were investigated in the laboratory (Table 2).

206 3.2. Laboratory and computational methods for rock characterization

207 The integrated analytical programme designed for this study includes the following laboratory
208 measurements and computations conducted at different scales (from the micro scale reflecting the scale of
209 individual pores and grains to the core scale reflecting the scale of the laminas at the outcrop) (Table 1).
210 Specimens ~5-7 cm in size were investigated by petrographic and petrophysical lab methods. Sub-samples ~1
211 cm in size were retrieved from the aforementioned plugs for investigation by 3D imaging, digital image
212 analysis and simulation techniques (described in more detail below).

213 Petrographic and petrophysical analysis (#1-7 in Table 1) have been conducted following the RP40
214 guidelines (Recommended Practices for Core Analysis, API, 1998), giving detailed information on theory,
215 advantages and drawbacks of each method. Extended computational workflow (#8 in Table 1) combines
216 several methods that may contain some variability in their application for the rock characterization. Those are
217 described in more detail below.

Deleted: All

Deleted: .

Deleted: also

Deleted: a

Deleted: used

223 **Table 1.** Laboratory methods employed and petrophysical characteristics determined *from these methods*

Deleted: in this study

Method	Determined petrophysical characteristics
1. Scanning electron microscopy (SEM)	Mineral abundance, grain surface characterization of matrix and cementation
2. Grain size analysis (Laser diffraction)	Grain size distribution (<i>GSD</i>)
3. X-ray diffraction (XRD)	Mineral components
4. Nitrogen gas porosimetry	Porosity (ϕ)
5. Steady state permeametry	Permeability (1D) (κ)
6. Mercury intrusion porosimetry (MIP)	Pore throat size distribution (<i>PTSD</i>), specific surface area (<i>SSA</i>), characteristic length (l_c), pore throat length of maximal conductance (l_{max}), permeability (κ)
7. <u>Optical</u> microscopy Plane-parallelized (PPL) and cross-parallelized (XPL) and reflected-light (RL) microscopy, binocular (BINO).	Mineral abundance, grain surface characterization, cementation
8. Extended computational workflow: Digital image analysis (DIA) <u>Semivariogram analyses</u> Fluid flow modelling	 Porosity (ϕ), pore specific surface area (<i>PSA</i>), tortuosity (τ), pore size distribution (<i>PSD</i>), connectivity index (<i>CI</i>), micro-CT predicted porosity from MIP <u>Range of spatial correlation of pore structures</u> Permeability tensor ($\bar{\bar{\kappa}}$), tortuosity (τ)

Deleted: Petrographic

224

225 Petrographic descriptions of rock compositions and textures at the micro scale, notably those of the fine
226 fraction, were performed using scanning electron microscopy (*JCM-6000 Bench Top SEM device*; e.g.,
227 Krinsley et al., 2005) using both backscatter and secondary electron modes.

Deleted: .

228 Thin-section optical microscopy (*Olympus BX53 device*, e.g., MacKenzie et al., 2017) was used to
229 estimate the mineral abundance and surface features of the grains, and the mineralogical and textural features
230 of matrix and cement. Grain size distributions were determined by a laser diffraction particle size analyser (*LS*

Deleted: Adams

235 13 320; e.g., Wang et al., 2013). X-ray diffraction (Miniflex 600 device by Rigaku; e.g., Asakawa et al., 2020)
 236 was applied to powdered samples to determine their mineralogical composition.

237 Effective porosity and permeability were evaluated on dried cylindrical samples (2.5 cm in diameter and
 238 5-7 cm in length). Effective porosity (ϕ) was measured using a steady-state nitrogen gas porosimeter produced
 239 by Vinci Technologies (HEP-E, Vinci Technologies; e.g., Viswanathan et al., 2018). Absolute permeability (κ)
 240 was measured by using a steady-state nitrogen gas permeameter (GPE, Vinci Technologies; e.g., Tidwell et
 241 al., 1999).

242 Mercury intrusion porosimetry (Micromeritics AutoPore IV 9505, which considers pore throats larger
 243 than 0.006 μm ; e.g., Giesche, 2006) was applied to dried cylindrical samples $\sim 1 \text{ cm}^3$ in size to evaluate the
 244 following parameters (Table 1):

- 245 • Pore throat size distribution (PTSD, Lenormand, 2003).
- 246 • Specific surface area (SSA): the pore surface to bulk sample volume (Rootare and Prenzlöw, 1967;
 247 Giesche, 2006).
- 248 • Characteristic length (l_c): the largest pore throat width (obtained from the increasing intrusion
 249 pressure) at which mercury forms a connected cluster (Katz and Thompson, 1987).
- 250 • Pore throat length of maximal conductance (l_{max}): defines a threshold for the pore throat size l at
 251 which all connected paths composed of $l \geq l_{max}$ contribute significantly to the hydraulic
 252 conductance, whereas those with $l < l_{max}$ may completely be ignored (Katz and Thompson,
 253 1987).
- 254 • Permeability (Katz and Thompson, 1987):

$$255 \quad \kappa = \frac{1}{89} l_{max}^2 \frac{l_{max}}{l_c} \phi S(l_{max}) \quad (1)$$

256 where $S(l_{max})$ is the fraction of connected pore space that is composed of pore throat widths of size l_{max} and
 257 larger. This approach (Katz and Thompson, 1987), which was derived from percolation theory (Ambegaokar
 258 et al., 1971), is applicable for sandstones with a broad distribution of local conductances with short-range
 259 correlations only.

260 An extended computational workflow (similar to the procedure presented by Boek and Venturoli, 2010;
 261 Andrä et al., 2013a,b) (Figure 2) serves as one of the main methodologies in our study to upscale permeability.

Deleted: following the RP40 guidelines (*Practices for Core Analysis, API, 1998*).

Deleted: h

Deleted: y, v3.20

Deleted: , Das and Gogoi, 2018

Deleted: and Wilson

Deleted: Gieshe

Deleted: , 2013

Deleted: Fig.

271 It includes 3D micro-CT imaging of porous samples, digital image processing and segmentation, statistical
272 analyses for the determination of representative elementary volumes, and pore-scale flow modelling through
273 the 3D pore geometry of the rock. First, cylindrical subsamples 4-8 mm in diameter and 5-10 mm in length
274 were retrieved from the larger samples studied in the laboratory and were scanned non-destructively (Figure
275 2b) by using a *Nanotom 180 S* micro-CT device (*GE Sensing & Inspection Technologies, phoenix/X-ray*
276 *product line*, Brunke et al., 2008). The achieved voxel size of the data sets was $2.5\ \mu\text{m}$ or $5\ \mu\text{m}$ (isotropic),
277 suitable for imaging pore throats that effectively contribute to the flow in the studied type of sandstone (e.g.,
278 Nelson, 2009). Afterwards, all data sets were filtered for de-noising, X-ray artefact removal and edge
279 enhancement (Figure 2c). The post-processed images scanned with $2.5\ \mu\text{m}$ resolution had an edge length of
280 1180 voxels or $2950\ \mu\text{m}$. Image artefacts were processed as described by Wildenschild and Sheppard (2013).
281 Beam hardening artefacts were removed by applying the best-fit quadratic surface algorithm (Khan et al.,
282 2016) to each reconstructed 2D slice of the image. Ring artefact reduction and image smoothing (with
283 preservation of sharp edge contrasts) were performed using a non-local means filter (Schlüter, 2014).
284 Segmentation was performed to convert the grey-scale images obtained after image filtering into binary images
285 to distinguish between voids and solid phases (Figure 2c). The local segmentation approach, which considers
286 the spatial dependence of the intensity for the determination of a voxel phase, was used in addition to a
287 histogram-based approach (Iassonov et al., 2009; Schlüter et al., 2014). Two-phase segmentation was
288 performed by the converging active contours algorithm (Sheppard et al., 2004), a combination of a watershed
289 (Vincent et al., 1991) with an active contour algorithm (Kass et al., 1988).

290

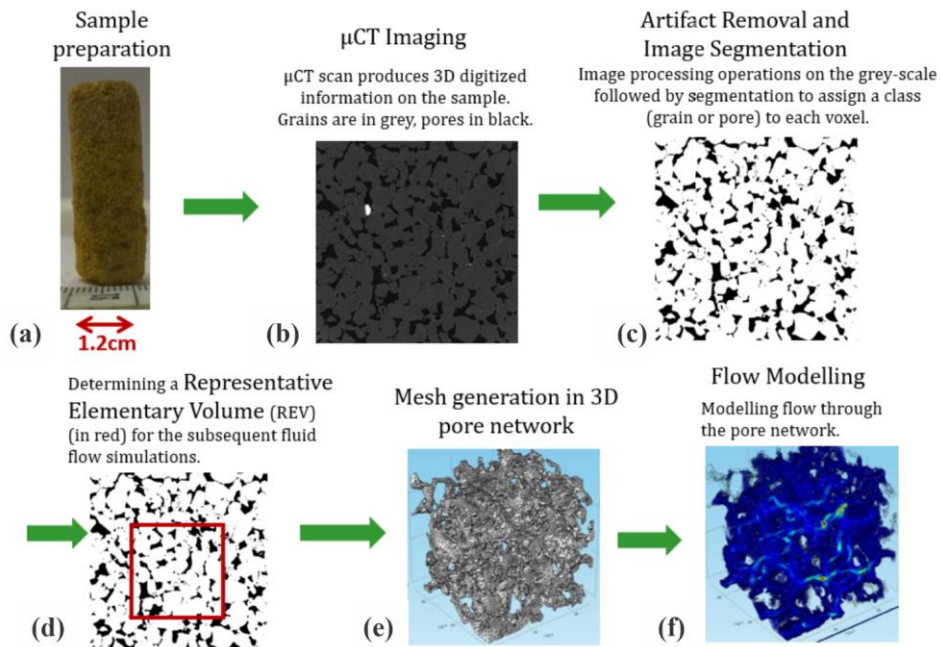
Deleted: Fig.

Deleted:

Deleted: Fig.

Deleted: Fig.

295
296



297

298 **Figure 2:** Extended computational workflow. See text for more details. Images (e) and (f) are adopted from
299 Bogdanov et al. (2012).

300 Simulations involving the real geometry of an imaged rock are computationally power and time
301 consuming. Therefore, the determination of a representative elementary volume (REV) is required (Figure 2d),
302 assuming that porous media are homogeneous at REV dimensions (Bear, 2013). A REV is required in the
303 current study to perform fluid flow simulations. Porosity, a basic macroscopic structural property of porous
304 media, is used here for the estimation of an REV (Bear, 2013; Halisch, 2013a; Tatomir et al., 2016) based on
305 its correlation with permeability (Kozeny, 1927; Carman, 1937) (see discussion on this issue in the Discussion
306 Sect.).

Deleted: .

Deleted: Fig.

Deleted: 1988

Deleted: n

Deleted: 1988

Deleted: However, the REV of permeability in sandstone is twice larger than REV of porosity, and using too low REV size results in overestimation of the permeability (Mostaghimi et al., 2013).

Two approaches were used in this study to estimate the REV (Halisch, 2013a,b). In the “classic” approach, the REV is attained when porosity fluctuations in the sub-volumes that grow isotropically in three orthogonal directions become sufficiently small (Bear, 2013). Practically, a large number of randomly distributed cubes were analysed through the entire 3D sample (with a 1180 voxel edge length in our case) for their image porosity (IP). The chosen initial cube size (with an edge length of 10 pixels in our case) was increased by 10-100 voxels. The REV size was specified when agreements between the mean and median IP values as well as saturation in the IP fluctuations were attained. The results of the REV estimation by this classic approach can be found in Appendix A.

A more advanced “directional” REV approach can capture porosity changes in a specific direction caused by microscopic structural features, such as grain packing, cracks, and textural effects (Halisch, 2013b). The \overline{IP} is calculated slice by slice across the segmented image in each orthogonal direction.

Semivariogram analysis was also conducted to estimate the REV. Semivariogram (Cressie, 1985) defines the relation between a spatially varying property (porosity in our case) and a lag distance (a Cartesian distance between the points in the studied domain). The semivariogram value increases when the values of the studied parameter become more dissimilar. Semivariogram, $\gamma(h)$, is based on the difference in values of the studied property between all combinations of pairs of data points, x_i and y_i , in the studied domain and is defined by:

$$\gamma(h) = \frac{1}{2N(h)} \sum_{i=1}^{N(h)} (x_i - y_i)^2 \quad (2),$$

where $N(h)$ is the number of pairs, and h is the lag distance. A semivariogram describing a single variability structure is characterized by a sill (a plateau) in which γ corresponds to the total variability of the sample, and by the range (of correlation) in h at which γ reaches the sill value (usually ~95 % of the sill value). Due to the spatial continuity of the CT dataset, a lag increment of a voxel size, set by the CT acquisition resolution, was chosen for calculation of the semivariogram, thus producing a large amount of data point pairs at each lag to get a significant mean (Ploner, 1999). A non-zero intercept in the semivariogram (nugget effect) may exist due to variability at lengths smaller than the lag distance and due to noisy data. For CT data, natural variations below the fixed resolution limit are invisible for the variography analysis. Therefore, in CT data the nugget effect may be observed only due to measurement error inherent to measuring devices. In a case they are small, the semivariogram will approximately have a zero intercept.

Deleted: 1988

Deleted: B

Deleted: average porosity

Deleted: first

Deleted: Variogram

Deleted: analysis

Deleted: 1993????

Deleted: the variability of

Deleted: parameter

Deleted: the

Deleted: as samples

Deleted:

Deleted: is used to describe the degree of spatial variability of the porosity in each direction based on the assumption that a distance at which no spatialofentire The variability estimated aentire . Therefore the lag distance that featuresin the specific direction isforentire

Deleted: value

Deleted: the

Deleted: $\gamma(h)$ is half the average of the squared difference,

Deleted: x_i and y_i are the values of the points,

Deleted: - a

Deleted: with

Deleted: ,

Deleted:

Deleted: the data in the semivariogram

Deleted: is the

Deleted: in the common practice it when it reaches

Deleted: T

Deleted: minimal

Deleted: the

Deleted: ,

Deleted: occurs because of the error

Deleted: in

Deleted: , and i

377 There are several analytical models that fit the semivariograms. In this study we use three of them (for
 378 more information see Cressie, 1985).

379 Gaussian: $\gamma(h) = C \left[1 - \exp \left(-3 \left(\frac{h}{a} \right)^2 \right) \right]$ (3)

380 Spherical: $\gamma(h) = C \left[\frac{3h}{2a} - \frac{1}{2} \left(\frac{h}{a} \right)^3 \right]$ for $h < a$, C else. (4)

381 Hole-effect: $\gamma(h) = C \left[1 - \cos \left(\frac{h}{a} \pi \right) \right]$ (5)

382 where C is the calibrated sill and a is a calibrated parameter.

383 Multiple sills may be associated with different variability structures, which are characteristic, for
 384 instance, for the different scales. Nested sills are modelled as a linear combination of the single models:

385 Nested sills: $\gamma(h) = \sum_{i=1}^n C_i \gamma_i(h)$, $0 < C$ (6)

386 where C_i is the contribution of a single sill.

387 z-direction of CT specimen used in this analysis is perpendicular to the natural layering of the sandstone
 388 identified in the outcrop and in the petrographic observations. x- and y- orthogonal directions lie in the
 389 horizontal plane, with an azimuth chosen randomly. The application of the semivariogram analysis using all
 390 data points (the voxels) distributed at multiple 3D sub-volume domains, is computationally intensive as the
 391 typical CT dataset includes 10^9 points and more. To allow faster semivariogram calculations, we slice the
 392 volume by cross-sections with a voxel size distance between them in each direction and evaluate the porosity
 393 at each cross-section, which produces a one-dimensional porosity profile. This results in histograms (the
 394 population of cross-sections porosity) that differ in each direction and also from those in the original 3D
 395 dataset. Therefore, for each direction a semivariogram model is independently calculated and modelled. In
 396 case when the variable is identified with a spatial systematic trend, the mean value will not to be independent
 397 of location (considered as a non-stationarity) that disconsiders the representativeness of the sample. When such
 398 a trend is identified, it should be modelled and removed from the property dataset, to remain with residuals.
 399 Next, a common practice is to calculate the semivariogram to a standardized histogram of the data to have a
 400 sill of 1 (Gringarten and Deutsch, 2001), which is achieved by z-score transformation (a normal score
 401 transform) of the residual porosity histograms. For evaluation of representative lengths, when along some
 402 direction the variability changes merely with an increasing lag distance, a sill (in a nested model) is calibrated

Deleted: at the smaller minimum ().Twitththus

Deleted: a few...several analytical models which...hat fit the semivariograms. In this study we relate to...se three of them (for more information see i.e.

Deleted: W...ere C is the calibrated sill and a is a second

Deleted: relate to physical phenomena occurs at...or the different scales. Nested sills are can be...modelled as a linear combination of the single models;

Deleted: ,

Deleted: The CT specimen is composed of slices along a direction z-direction of CT specimen used in this analysis isaxis...perpendicular to the natural layering of the sandstone identified which found...in the field...utcrop and from...n the petrographic observations. x- and y- orthogonal directions lie are perpendicular axes ...n the horizontal plane, with the...n azimuth chosen randomly. The application o apply...f the semivariogram analysis using all the 3D distributed ...ata points (the voxels) and...istributed at multiple 3D sub-volume domains, is computationally intensive as the typical CT dataset includes 10^9 points and more. To allow faster semivariogram calculations, we slice the volume to...y surfaces...ross-sections with...ith a voxel size width...istance between them along...n each direction and measure...valuate the average porosity

Deleted: s

Deleted: ing...a one-dimensional porosity profile along each axis... This results in e price paid by doing so is that the

Deleted: PLS SPECIFY WHAT DEPENDS ON WHAT IN THE HYSTOGRAM

Deleted: along...n each direction and are...now different from each other and...Iso from those in the original 3D dataset. Therefore, for each direction a different ...emivariogram model is independently calculated and modelled, rather than using a single variogram model for all directions in 3D dataset... The...n case when the variable is identified with a spatial systematic trend, the mean value will not to be independent of location (considered as a non-stationarity) that, what...disconsiders the representativeness of the sample. When such a trend is identified, it should be modelled and removed from the property dataset, to result...emain with the

Deleted: A

Deleted: an ...valuation of representative lengths, when along a...ome direction the variability merely

492 and the resulting calibrated range represents a length associated with a natural spatial structure in the sample.
 493 When a sill is calibrated similarly to the complete variability (sill~1) in the sample, the calibrated range is
 494 defined as a representative length in the studied direction. The experimental and modelled (Eqs.3-6),
 495 semivariograms were calculated in this study using dedicated MATLAB packages (Schwanghart, 2020a,b).

496 Further, the representative binary 3D image (REV) of the pore space was spatially discretised by
 497 tetrahedrals with *Materialize software (Belgium)* (Figure 2e). This step is required for importing the REV into
 498 the FEM-based modelling software (*Comsol Multiphysics simulation environment*, v5.2a). Stokes flow (Re <<
 499 1) is simulated (Table 1) in the pore network (Figure 2f) by the following equations (e.g., Narsilio et al., 2009;
 500 Bogdanov et al., 2011):

501 Stokes equation: $-\nabla p + \mu \nabla^2 \bar{u} = 0$ (7)

502 Continuity equation: $\nabla \cdot \bar{u} = 0$ (8)

503 where ∇p is the local pressure gradient, \bar{u} is the local velocity vector in the pore space and μ is the dynamic
 504 fluid viscosity. Fixed pressures ($p=const$) were specified at the inlet and outlet boundaries of the fluid domain
 505 with a constant pressure gradient of 2.424 Pa/mm over the domain prescribed in all the simulations for
 506 consistency. At the internal pore walls and at the lateral domain boundaries, no-slip boundary conditions ($\bar{u} =$
 507 0) were imposed (e.g., Guibert et al., 2016). These also simulate the flow setup in a steady-state experimental
 508 permeameter (e.g., Renard et al., 2001). The macroscopic fluid velocity $\langle \bar{v} \rangle$ was evaluated by
 509 volumetrically averaging the local microscopic velocity field (e.g., Narsilio, 2009; Guibert et al., 2016). Then,
 510 from the average macroscopic velocity vectors v_i^j in three orthogonal i -directions corresponding to the
 511 pressure gradients ∇p_j imposed in j -directions, the full 3D second-rank upscaled permeability tensor $\bar{\kappa}$ can be
 512 found:

513
$$\begin{pmatrix} v_x^x & v_x^y & v_x^z \\ v_y^x & v_y^y & v_y^z \\ v_z^x & v_z^y & v_z^z \end{pmatrix} = -\frac{1}{\mu \phi} \begin{pmatrix} \kappa_{xx} & \kappa_{xy} & \kappa_{xz} \\ \kappa_{yx} & \kappa_{yy} & \kappa_{yz} \\ \kappa_{zx} & \kappa_{zy} & \kappa_{zz} \end{pmatrix} \begin{pmatrix} \nabla p_x & 0 & 0 \\ 0 & \nabla p_y & 0 \\ 0 & 0 & \nabla p_z \end{pmatrix}$$
 (9)

514 The permeability tensor is symmetrized by:

515
$$\bar{\kappa}_{sym} = \frac{1}{2} (\bar{\kappa} + \bar{\kappa}^T)$$
 (10)

Deleted: an as

Deleted: is

Deleted:

Deleted: which is

Deleted: E

Deleted: ing

Deleted: correlation exists reflects the scale of homogeneity, which defines the REV. The variogramsemivariogram $\hat{\gamma}(h)$, i.e., the expected squared difference between two observations (here, the average of 2D IPs), is calculated as a function of their separation distance, h (lag). Practically, the lag distance at which the variogramsemivariogram curve is saturated is the distance at which no spatial correlation exists (defined as the range of a spatial correlation). Depending on the sample heterogeneity at different scales, the variogramsemivariogram may manifest a different range for each scale. VariogramSemivariogram analysis was performed using the 'VariogramSemivariogramfit' MATLAB package.¶

Deleted: Fig.

Deleted: Fig.

Deleted: 2

Deleted: 3

Deleted:

Deleted: .

Deleted: 4

Deleted: 5

541 Tortuosity (τ ; Bear, 2013; Boudreau, 1996) was calculated separately in the x-, y- and z-directions in
542 the meshed domain using the particle tracing tool of *Comsol Multiphysics software* (an additional method for
543 deriving τ is presented later in this section).

544 3D image analysis (Table 1) was conducted on a high-quality, fully segmented micro-CT image (edge
545 length of 2950 μm scanned at a 2.5 μm voxel size). Non-connected void clusters in the binary specimen were
546 labelled and then separated into objects (single pores and grains) by using a distance map followed by the
547 application of a watershed algorithm (e.g., Brabant et al., 2011; Dullien, 2012). Image analysis operations were
548 assisted by *Fiji-ImageJ software* (Schindelin et al., 2012) and by the *MorphoLibJ plug-in* (Legland et al.,
549 2014). The following geometrical descriptors were derived from the segmented image limited by the image
550 resolution of 2.5 μm (Table 1):

- 551 • micro-CT image porosity (IP);
- 552 • Pore specific surface area (PSA – surface to pore volume);
- 553 • Tortuosity: evaluated in the x-, y- and z-directions by finding the average of multiple shortest paths
554 through the main pore network using the fast marching method (Sethian, 1996) implemented using an
555 accurate fast marching plug-in in MATLAB.
- 556 • Pore size distribution (PSD): obtained by a Feret maximum calliper (Schmitt et al., 2016).
- 557 • Euler characteristic (χ) - a topological invariant (Wildenschild and Sheppard, 2013; Vogel, 2002) that
558 describes the structure of a topological space (see [Supplementary material](#) for more detail). Since the
559 number of pore connections depends on the number of grains, it is essential to normalize χ (Scholz et
560 al., 2012) to compare the connectivity among three samples that have the same dimensions but
561 different grain sizes.
- 562 • Connectivity index (CI): computed by dividing the absolute value of the Euler characteristic ($|\chi|$) by
563 the number of grains in the specimen (N , determined by image analysis), $CI = |\chi|/N$.

564 [Table 1 allows conducting a comparison between the characteristics derived by the different methods at](#)
565 [the different scales of investigation \(similarly to Table 1 in Tatomir et al. \(2016\) that focuses on the similar](#)
566 [rock\).](#)

567 Additionally, we propose a simple and new method to estimate the image porosity at a given resolution.
568 Multiplication of the mercury effective saturation at the capillary pressure corresponding to the micro-CT

Deleted: 1988

Deleted: Appendix C

571 resolution (e.g., 2.5 μm) by the porosity of the same sample measured by a gas porosimeter yields the *micro-*
572 *CT-predicted image porosity from MIP* at the given resolution limit (Table 1).

573

574

Deleted: i.e

576 **4. Results**

577 **4.1. Petrographic and petrophysical rock characteristics**

578 Three types of sandstone rocks were characterized by techniques 1-8 listed in Table 1. The results are
579 presented in Figures 3-8 and summarized in Table 2.

580 **Sandstone S1:** The top unit layer with a thickness of ~1.5 m (Figure 1c) consists of yellow-brown
581 sandstone (Figure 3a), which is moderately consolidated. The sandstone is a mature quartz arenite (following
582 Pettijohn et al., 1987) with minor Fe-ox, feldspar and heavy minerals (e.g., rutile and zirconium). The grain
583 size distribution has a mean of ~325 μm (Figure 6a, Table 2). The grains are moderately sorted (according to
584 the classification of Folk and Ward, 1957) and sub-rounded to well-rounded with local thick (millimetre-scale),
585 relatively dark envelopes (Figure 3b). The sandstone consists of alternating millimetre-scale layers of large
586 and small sand grains. Secondary silt (~45 μm) and clay (~0.95 μm) populations are detected in the grain size
587 distribution (Figure 6). X-ray diffraction detected a small amount of kaolinite. The Fe-ox grain-coating and
588 meniscus-bridging cement is composed of overgrown flakes aggregated into structures ~10 μm in size (Figure
589 3c-3f). Mn_{oxide} is also evident but is scarce (Figure 3e).

590 The pore network is dominated by primary inter-granular well-interconnected macro porosity (Figure
591 3b). However, sealed and unsealed cracks in grains are also observed. Higher Fe-ox cementation at the
592 millimetre scale on horizontal planes is recognized (Figure 3a). In addition, smaller voids between Fe-ox
593 aggregates and flakes occur at the micrometre scale and smaller (Figure 3d-f).

594 The pore throat size analysis conducted with MIP shows that 82 % of the pore volume is composed of
595 macro pores (>10 μm) following a log-normal distribution with a peak at 44 μm (Figure 7a). The characteristic
596 length, i.e., the largest pore throat length at which mercury forms a connected cluster, is $l_c = 42.9 \mu\text{m}$ (Figure
597 7b), and the pore throat length of maximal conductance is $l_{max} = 34.7 \mu\text{m}$ (Appendix B, Figure B1). The
598 porosity evaluated by laboratory gas porosimetry varies in the range of 26-29 % for 7 different samples of S1
599 (Figure 8). Multiplying the mercury effective saturation (85.8 %) at the micro-CT resolution (2.5 μm) (Figure
600 7a, red dashed line) by the porosity of the same sample measured by gas porosimetry (27.3 %) yields a micro-
601 CT-predicted image porosity of 23.5 % at a resolution limit of 2.5 μm (Table 2).

Deleted: Fig.

Deleted: Fig.

Deleted: Fig.

Deleted: Fig.

Deleted: Fig.

Deleted: Fig.

Deleted: -

Deleted: Fig.

Deleted: Fig.

Deleted: Fig.

Deleted: Fig.

Deleted: μm

Deleted: Fig.

Deleted: Fig.

Deleted: D

Deleted: Fig.

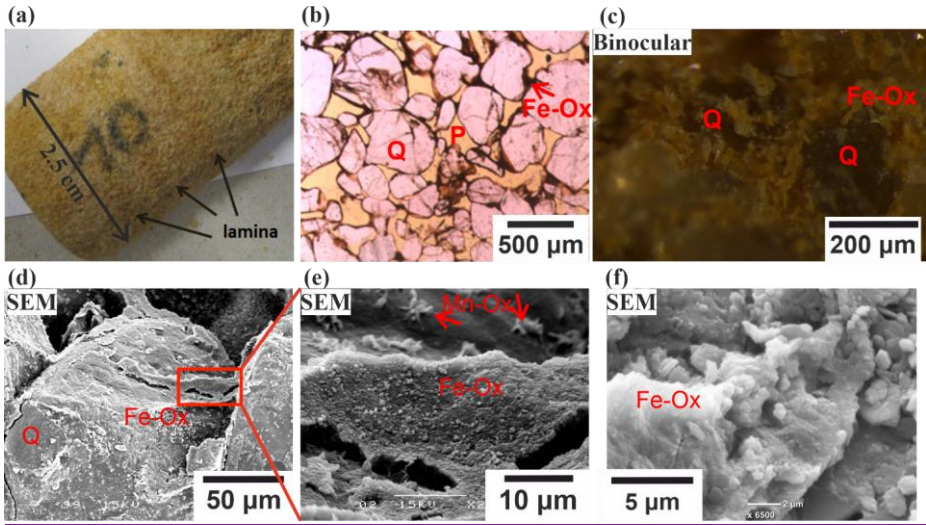
Deleted: D1

Deleted: Fig.

Deleted: Fig.

621 The permeability evaluated by a laboratory gas permeameter has averages of 350 mD (range of 130-
622 500 mD) for 5 samples measured perpendicular to the depositional plane (z-direction) and 640 mD for 2
623 samples measured parallel to the depositional plane (x- and y-directions) (Figure 8). MIP measurement (Katz
624 and Thompson, 1987) yields a permeability (see Sect. 3.2) of 330 mD (Table 2).

Deleted: Fig.



625
626 **Figure 3:** Representative images of sandstone SI. (a) Darker laminae in the x-y plane at the millimetre scale are observed.
627 (b) Thin section image of SI, P refers to open pores, Q – to quartz, Ox to oxide. (c) Fe-ox flakes (yellow) on quartz grains
628 (pale grey). (d) SEM image of SI: grain-coating, meniscus-bridging cement and overgrowth of Fe-ox flakes. (e,f)
629 Magnified images at different scales.

630

631

633 **Table 2.** Petrophysical characteristics of the three studied sandstone layers.

	Method	S1	S2	S3
Grain size	Laser diffraction	325 µm medium sand moderately sorted sand: 92.6 % silt: 6.6 % clay: 0.8 %	154 µm very fine sand poorly sorted 65.7 % 31.3 % 3 %	269 µm fine sand moderately sorted 94.4 % 4.8 % 0.8 %
Pore throat size	MIP	Mode 1: 44 µm Mode 2: 0.035 µm Mode 3: 2.2 µm macro pores well sorted	0.035 µm 3.5 µm meso pores poorly sorted	35 µm 0.035 µm 2.2 µm macro pores well sorted
Pore size	Image analysis (min. object size 2.5 µm)	194 µm (*FWHM [150,335] µm)	Mode 1: 21 µm Mode 2: ~100 µm	223 µm (*FWHM [145,400] µm)
Characteristic length, l_c	MIP	42.9 µm	12.3 µm	36.9 µm
l_{max} contributing to maximal conductance	MIP	34.7 µm	8 µm	31.4 µm
Porosity, ϕ	Gas porosimetry	28 ± 2 % (7**)	19 ± 5 % (8)	31 ± 1 % (4)
	CT predicted image porosity from MIP	23.5 %	6.6 %	30.4 %
	Micro-CT segmented	17.5 %	6.9 %	28.3 %
Permeability, κ ⊥ - perpendicular to layering (z-direction) - parallel to layering (x-y plane)	Gas permeametry	⊥ 350 mD (5) 640 mD (2)	⊥ 2.77 mD (5) 7.73 mD (3)	⊥ 220* mD (2) 4600* mD (2)
	MIP	330 mD (1)	4 mD (1)	466 mD (3)
	Flow modelling	$\begin{pmatrix} 420 & 66.3 & 1.91 \\ 66.3 & 344 & 12.8 \\ 1.91 & 12.8 & 163 \end{pmatrix}$ mD	-	$\begin{pmatrix} 4517 & 5 & 38 \\ 5 & 4808 & 547 \\ 38 & 547 & 4085 \end{pmatrix}$ mD
Specific surface area, SSA (surface-to- bulk-volume)	MIP	$3.2 \mu m^{-1}$	$12.2 \mu m^{-1}$	$0.16 \mu m^{-1}$
Pore specific surface area, PSA (surface-to-pore-volume)	Micro-CT at 2.5 µm resolution size	$0.068 \mu m^{-1}$	$0.136 \mu m^{-1}$	$0.069 \mu m^{-1}$
Connectivity index	Image analysis	3.49	0.94	10
Tortuosity, τ	Flow modelling	-	-	x: 1.443 y: 1.393 z: 1.468
	Micro-CT shortest path analysis	x: 1.385 y: 1.373 z: 1.477	-	x: 1.316 y: 1.338 z: 1.394

634 Legend:

635 *Addressed in the Discussion.

636 ** Numbers in parentheses related to gas porosity, gas permeability and MIP permeability, indicate the
637 number of plugs for the measurements. Other measurements and calculations were conducted on single
638 plugs.

639 FWHM - full width at half maximum, log-normal distribution.

640 **Sandstone S2:** The intermediate unit layer with a thickness of ~20 cm consists of grey-green moderately
641 consolidated sandstone (Figs. 1c, 4) composed of sub-rounded to rounded, very fine sand grains (~154 μm);
642 the sandstone is poorly sorted with 35 % of the particles being silt and clay (Figure 6, Table 2). Secondary silt
643 (~ 40 μm), sand (~400 μm) and clay (~1.5 μm) populations are also detected. The grains are composed of
644 quartz with minor Fe-ox coating the grains and minor quantities of heavy minerals (e.g., rutile and zirconium)
645 (Figure 4c). Clay filling the pore space was identified by XRD as a kaolinite mineral. It appears as a grain-
646 coating, meniscus-bridging, and pore-filling matrix (Figure 4b, c). Therefore, the unit layer (Figure 1c) is
647 classified as a quartz wacke sandstone (Pettijohn et al., 1987).

648 The pore space is reduced by clays deposited on coarser grains, identified mostly in laminae, (Figure 4a,
649 d). However, the inter-granular connectivity of macro pores can still be recognized (Figure 4b, c). The
650 effective pore network consists of inter-granular macro pores distributed between the laminae or zones richer
651 in clay and Fe-ox. Integrating the grain size and pore throat size analysis results (Figs. 6, 7) confirms that the
652 reduction in the inter-granular pore space in S2 is due to the clay matrix, which is reflected in the poor grain
653 sorting and large variance in pore size. In the pore throat size analysis (Figure 7), only 15 % of the pore volume
654 is composed of macro pores that are larger than 10 μm . The prominent sub-micron pore mode is ~35 nm, with
655 a population containing ~45 % of the pore volume (Figure 7a). This population of pores occurs inside the clay
656 matrix. The secondary pore volume population is poorly distributed within the range of 0.8-30 μm . The
657 characteristic length (Sect. 3.2), $l_c = 12.3 \mu\text{m}$ (Figure 7b), and the pore throat length of maximal
658 conductance, $l_{max} = 8 \mu\text{m}$ (Appendix B, Figure B1) (both have a large uncertainty resulting from uncertainty
659 in the threshold pressure), suggest a connectivity of macro pores regardless of their small fraction within the
660 total pore space. The porosity of S2 evaluated for 8 different samples varies in the range of 14.5-23.5 % (Figure
661 8). From the PTSD (Table 1) and gas porosimetry results (for a sample with a porosity of 18.6 %), micro-CT
662 predicts an image porosity of 6.6 % at a resolution limit of 2.5 μm (Table 2). The gas permeability in the z-
663 direction was measured in 5 samples (Figure 8): in four of them, the permeability ranges within 1-12 mD and

Deleted: Fig.

Deleted: Fig.

Deleted: Fig.

Deleted: Fig.

Deleted: The pore network is influenced by the extent of clay deposition on coarser grains, identified mostly in laminae

Deleted: Fig.

Deleted: Fig.

Deleted: Fig.

Deleted: Fig.

Deleted: Fig.

Deleted: D

Deleted: Fig.

Deleted: D1

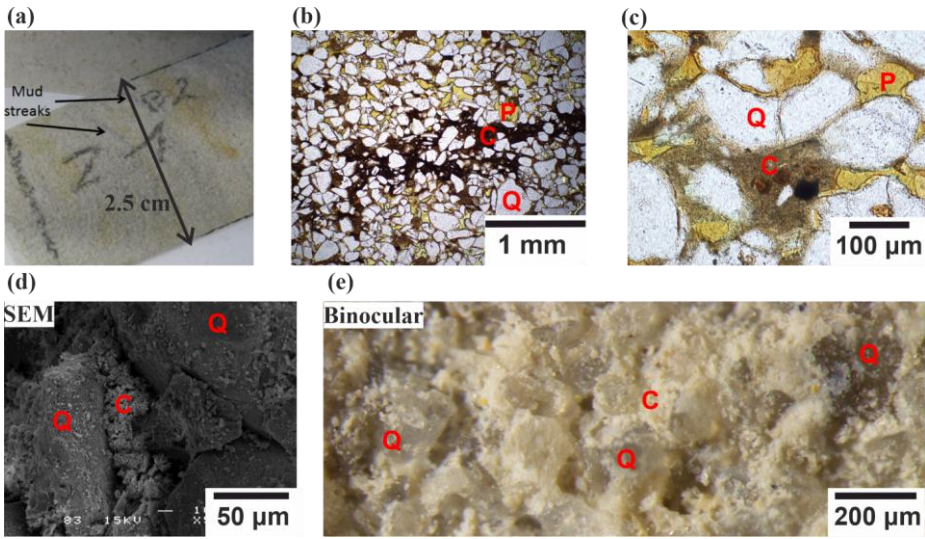
Deleted: Fig.

Deleted: Fig.

680 increases with porosity. However, one sample had an exceptionally large porosity and permeability of 23 %
681 and 62 mD, respectively. The permeability measured for 3 samples in the x-y plane ranges within 4-12 mD,
682 also showing ~15 % porosity (Figure 8). In addition, for the samples with ~15 % porosity, their permeability
683 is ten times larger in the x-y plane (parallel to the layering) than in the z-direction (perpendicular to the
684 layering). The permeability derived from MIP reaches 4 mD, which agrees with an average of 2.77 mD and
685 7.73 mD (Table 2) measured in the z-direction with a gas permeameter (excluding one exceptionally high
686 value, Figure 8).

Deleted: Fig.

Deleted: Fig.



687 **Figure 4.** Representative images of sandstone S2. (a) Dark stains in the rock are mud streaks, yellowish zones are due to
688 increased Fe-Ox cement. (b) The dark laminae are richer in clays and Fe-ox. P refers to open pores, Q – to quartz, C –
689 to clay. (c) Clay and silt accumulated as meniscus and as clay matrix. (d) Pore clogged by clay and Fe-ox. (e) Rock
690 texture. The clay matrix is white, and quartz grains are pale grey.

Deleted: .

Deleted: Fig.

Deleted: Fig.

Deleted: Samples were taken from the ~1.5 m thick bottom unit layer in the outcrop (Figure

Deleted: Fig.

Deleted: 1c) consisting of (pale) red-purple poorly consolidated sandstone with grains covered by a secondary red patina (Fig. 5).

693 **Sandstone S3:** The bottom unit layer with a thickness of ~1.5 m consists of (pale) red-purple poorly
694 consolidated sandstone (Figure 1c) with grains covered by a secondary red patina (Figure 5). The sandstone

705 is composed of friable to semi-consolidated, fine ($\sim 269\text{ }\mu\text{m}$), moderately sorted sand (Table 2), where only
706 5.6 % of particles are silt and clay (Figure 6). Secondary silt ($\sim 50\text{ }\mu\text{m}$) and clay ($\sim 0.96\text{ }\mu\text{m}$) populations were
707 also detected. The sandstone consists of sub-rounded to rounded grains showing a laminated sedimentary
708 texture consisting of the cyclic alternation of relatively dark and light red bands of millimetre-scale thickness
709 (Figure 5a). The dark laminae contain slightly more Fe-ox meniscus-bridging and pore-filling cementation
710 (Figure 5b, d). Overall, this bed consists of a ferruginous quartz arenite. The grains are dominated by quartz
711 with very minor feldspar and black opaque mineral grains, perhaps Fe-ox (Figure 5d). X-ray diffraction
712 indicated quartz only. The Fe-ox coating of grains is less extensive than in other samples (Figure 5c). The
713 pore interconnectivity in this sandstone is high (Figure 5d). Heavier cementation is rarely observed (Figure
714 5d) and is organized in horizontal laminae (Figure 5a). Features including grain cracks, grain-to-grain
715 interpenetration, and pressure solution are also recognized (Figure 5e). The PTSD showed that 95 % of the
716 pore volume is presented by macro pores (Figure 7a), which agrees with the minority of fine particles. The
717 characteristic length and pore throat length of maximal conductance are $l_c = 36.9\text{ }\mu\text{m}$ (Figure 7b) and $l_{max} =$
718 $31.4\text{ }\mu\text{m}$ (Appendix B, Figure B1), respectively.

719 The porosity measured by a gas porosimeter in the laboratory varies in the range of 30-32 % for 4
720 different samples (Figure 8). From PTSD and gas porosimetry (Figs. 7, 8), the micro-CT-predicted image
721 porosity at a resolution limit of $2.5\text{ }\mu\text{m}$ is 30.4 % (Table 2). The permeability measured by a laboratory gas
722 permeameter averages 220 mD for 2 samples measured in the z-direction and 4600 mD for 2 samples
723 measured in the x-y plane (Figure 8), showing a ten-fold difference (discussed in Sect. 5). The permeability
724 derived from MIP reaches 466 mD (Table 2).

Deleted: Fig.

Deleted: Fig.

Deleted: Fig.

Deleted: Fig.

Deleted: Fig.

Deleted: Fig.

Deleted: Fig.

Deleted: Fig.

Deleted: Fig.

Deleted: Fig.

Deleted: D

Deleted: Fig.

Deleted: D1

Deleted: Fig.

Deleted: Fig.

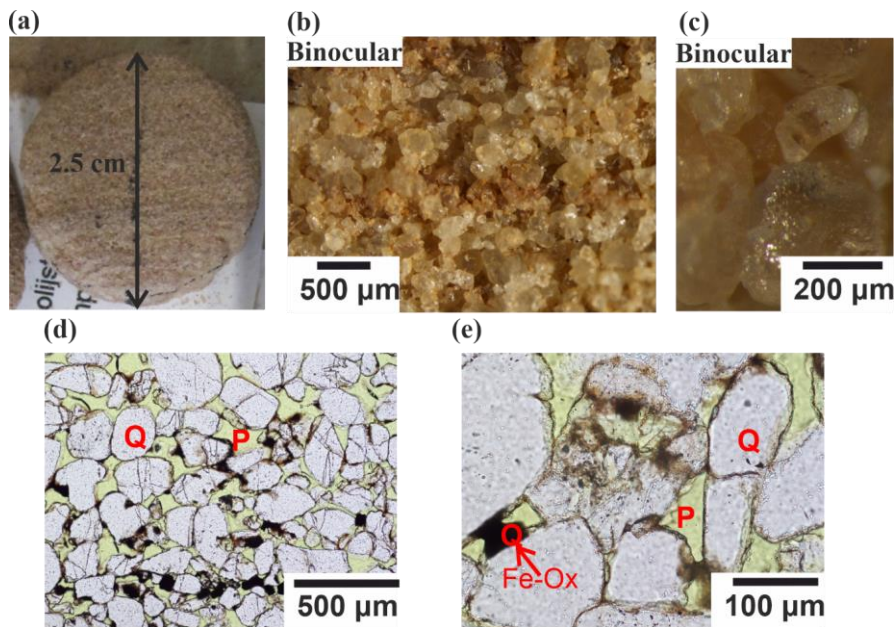
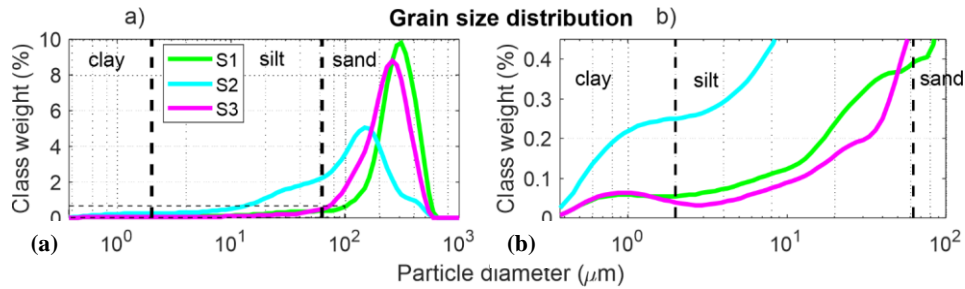


Figure 5. Representative images of sandstone S3. (a) Laminae are recognized by their slightly dark and red color. (b) General view reveals red laminae ~300 µm thick. (c) High-resolution observation of a clear grain. (d) A millimetre-scale lamina is indicated by enhanced meniscus-type Fe-ox cementation and partly by inter-granular fill. Grain surfaces are coated by thin Fe-ox. Black and orange cements represent crystallized and non-crystallized Fe-ox, respectively. Some cracked grains are observed, sporadically cemented by Fe-ox. P refers to open pores, Q – to quartz. (e) Partially dissolved grains are coated by cement.

750

751

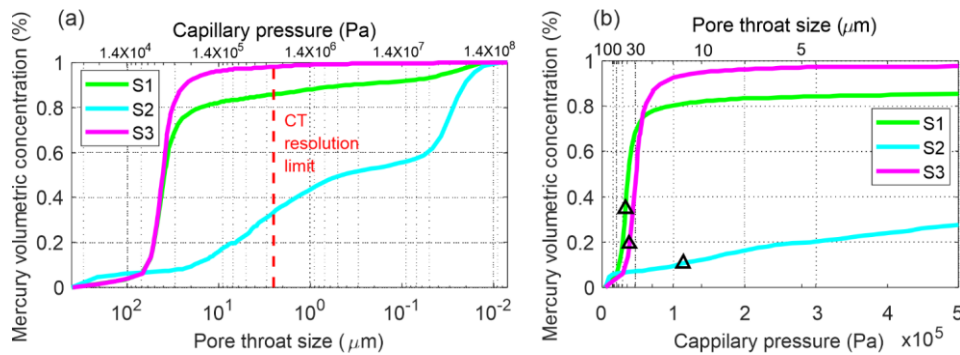
752



753

754 **Figure 6:** (a) Grain size distribution. (b) Magnified grain size distribution in the fine grain size region plotted
 755 for sandstones S1 (green), S2 (blue) and S3 (purple). S1 and S3 have a unimodal distribution and are
 756 moderately sorted with a small skewness tail. Sample S2 has a multi-modal distribution and is poorly sorted.

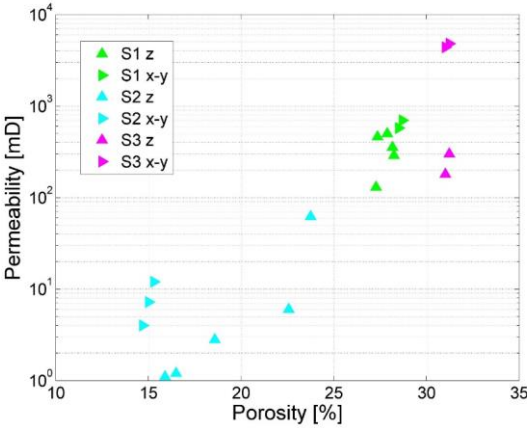
757



758 **Figure 7:** Cumulative pore throat sizes of the studied sandstones. (a) Capillary pressure on a logarithmic
 759 scale. The resolution limit of the micro-CT imaging indicates the fraction of the pore space that could be
 760 resolved. (b) Capillary pressure on a linear scale. The triangles indicate the characteristic length, l_c .

Deleted: normal

762



763

764 **Figure 8:** Results of porosity-permeability lab measurements. The permeability of the samples was measured
765 in directions perpendicular to the bedding (z-direction) and parallel to the bedding (x-y plane).

766 Overall, for all three investigated sandstones, the pore throat size contributing to the maximal
767 conductance, l_{max} , is smaller than the characteristic length, l_c (Table 2), when the relative decrease is greater
768 for the layers containing more fines.

769 Additionally, pore surface roughness may be evaluated from the specific surface area (SSA) measured
770 by MIP (Table 2). A larger SSA implies a rougher surface (e.g., Tatomir et al., 2016). The SSAs for S1 and S2
771 ($3.2 \mu\text{m}^{-1}$ and $12.2 \mu\text{m}^{-1}$, respectively) are similar to those given in the literature for sandstones of similar
772 properties (e.g., Cerepi et al., 2002). The SSA of S2 is higher because of its high silt and clay content of 34.3
773 %, which is only 7.4 % for S1 (Figure 6a). The SSA of S3 (where silt and clay constitute only 5.6 %, including
774 the Fe-ox rim coating) is only $0.16 \mu\text{m}^{-1}$, which is 20 times smaller than that of S1 (Table 2). The difference
775 in SSAs between S1 and S3, which are similar in their grain and pore throat size distributions (Figs. 6, 7), is a
776 result of S1 having a higher Fe-Ox grain coating than S3 (compare Figs. 3d and 5c).

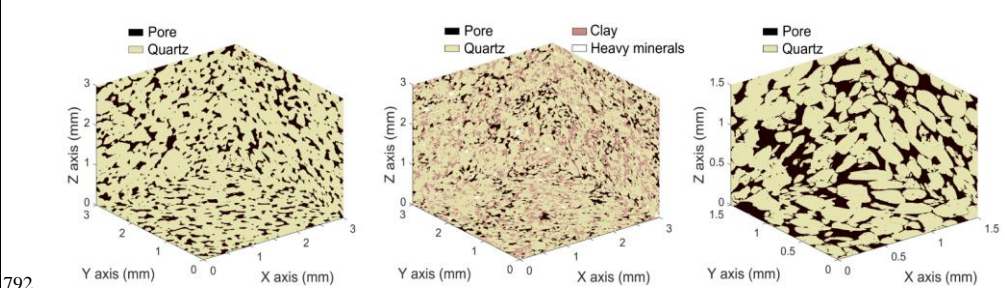
Deleted: Fig.

Deleted: $0.16 \mu\text{m}^{-1}$

779 In summary, although the S1 pore network has larger pore throats, it also has greater grain roughness
780 and lower connectivity than S3. These two properties dominate and generate a smaller permeability for S1
781 than for S3 (Table 2).

782 **4.2. Image analysis**

783 Visualized segmented sub-volumes of samples S1, S2, and S3, depicting Quartz, pores, clay and heavy
784 minerals, are presented in Figure 9. The main pore size population in PSD of S1 is at ~100-500 μm range with
785 majority at 194 μm (Figure 10). A smaller population of pores of ~30-100 μm was identified as well, which
786 may refer to (Mode 1) pore throat size derived from the MIP experiment (Table 2). Image resolution of 2.5
787 μm limited the analysis. The pore specific surface area (PSA) calculated from micro-CT images is
788 $0.068\text{ }\mu\text{m}^{-1}$. The tortuosity, measured from the whole CT image, indicates similar values in the x- and y-
789 directions of 1.37 and 1.38, respectively, whereas in the z-direction, the tortuosity is 1.48 (Table 2). As many
790 paths were considered, this difference indicates the textural features that appear in horizontal plane (Figure
791 3a).



Deleted: 109

Deleted: Orthogonal surfaces of the segmented CT sample S1 show the pore volume distribution in a $(3\text{ mm})^3$ representative sub-volume (Figure 109a). Using image analysis techniques on the pore network, ...t

Deleted: i

Deleted: of S1 distribute in the range

Deleted:

Deleted: ~200

Deleted: 1

Deleted: Table 2

Deleted: ,

Deleted: and a

Deleted: ,

Deleted: equivalent to the range of

Deleted: distribution which was

Deleted: Limited i

Deleted: was a bottom boundary which

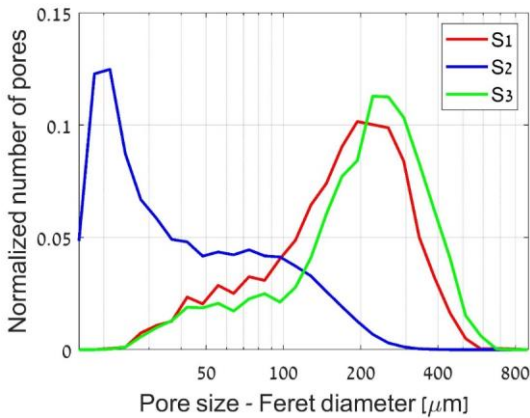
Deleted: measurement

Deleted: For S1, the mode peak of the pore size distribution (measured by a Feret maximum calliper) (Fig. 13, red line) is at 194 μm (Table 2). In total, 3500 pores were analysed.

Deleted: Fig.

Deleted: we suggest that this difference is created by the textural features that appear in horizontal planes (Fig. 3a)

819 **Figure 9:** Visualized sub-volumes of segmented CT samples of (a) S1, (b) S2, (c) S3. S1 and S2 in this
820 visualization have volumes 3^3 mm^3 scanned with $5 \mu\text{m}$ voxel size resolution, S3 has volume $1,5^3 \text{ mm}^3$ scanned
821 with $2.5 \mu\text{m}$ voxel size.



823 **Figure 10:** Statistics of the pore sizes calculated by image analysis for three sandstone samples: S1, S2, and
824 S3. Number of pores analysed: S1 – 3500, S2 – 45000, S3 – 3500. The CT samples used for this analysis had
825 $2.5 \mu\text{m}$ voxel size resolution.

826 For S2 (Figure 9), the main pore size population is at $\sim 15\text{-}50 \mu\text{m}$ range (Figure 10), with majority at 21
827 μm . This may refer to the pore throat size derived from MIP. However, smaller pore throat sizes which were
828 derived from the MIP (mode peak is at $\sim 3.5 \mu\text{m}$) could not be visualized due to the limited resolution of the
829 image ($2.5 \mu\text{m}$), and because of high uncertainty associated with size of pores smaller than $10 \mu\text{m}$ (four voxels)
830 (that were excluded from the PSD evaluation, Figure 10). A large pore population is also recognized at ~ 100
831 μm (Figure 10), which corresponds to the pore size scale recognized from the petrography (Figure 4), MIP
832 (Figure 7) and CT image (Figure 9). The pore specific surface area (PSA) calculated from micro-CT images
833 is

834 $0.136 \mu\text{m}^{-1}$ (Table 2), which is twice as large as the PSA of S1.

Deleted: Orthogonal surfaces of segmented samples

Deleted: cell size

Deleted: cell size

Deleted: ,

Deleted: P

Deleted: ,

Deleted: Figure 13: Statistics of the pore sizes calculated by image analysis for three sandstone samples: S1, S2, and S3.

Deleted: 10

Deleted: ,

Deleted: , blue line

Deleted: ~

Deleted: 0

Deleted: length

Deleted: refers

Deleted: which was

Deleted: whereas

Deleted: smaller

Deleted: sizes smaller

Deleted: sample

Deleted: 2.

Deleted: the

Deleted: ey

Deleted: ,

Deleted: voxels at

Deleted: s

Deleted: 1

Deleted: relate

Deleted: observed

For S3 (Figure 9), the main pore size population is at ~100-500 μm range (Figure 10), with majority at 223 μm . The geometry-based tortuosity values measured from the whole CT image with multiple paths is 1.32, 1.34 and 1.39 in the x-, y- and z-directions, respectively. The tortuosity is lower for S3 than for S1 in all directions, which is a direct result of the smaller amount of cement in the pore throats. The *PSA* of S3 is 0.069 μm^{-1} , which is similar to that of S1.

869

4.3. REV Analysis

4.3.1. Quartz arenite sandstones (S1 and S3)

One-dimensional profiles of porosity (Figure 11(a-c)) were evaluated in sequential slices in three orthogonal directions of S1, having a maximal available segmented volume of $6.8 \times 6.9 \times 9.2 \text{ mm}^3$ scanned with a voxel size of 5 μm (suitable for imaging pore throats that effectively contribute to the flow in S1, Table 2). The slice-by-slice porosity distinguishes the z-direction as having an exceptional behaviour, with variance in porosity fluctuations being four times larger than that in x- and y- directions. Porosity fluctuates around the mean value with a wavelength of ~0.2 mm in x- and y- directions. Semivariograms (obtained after z-score transformation of porosity histograms, Figure 11d) show stationarity in x- and y- directions (i.e., sill~1, Figure 12). The nugget is set to zero (see Methods Sect. 3.2). A semivariogram was fitted using Gaussian model with range of ~0.1 mm for x- and y- directions (Figure 12a,b). A second semivariogram feature is the waviness, i.e. cyclic behaviour with lag distance. The lag distances of the first peaks in the experimental variograms are 0.135 and 0.15 mm in x- and y- directions, respectively. In laminated geologic settings, the distance to the first peak is an indication of the average thickness of the bedding in that direction (Pyrcz and Deutsch, 2003). However, here this distance refers to the average size of the cross sections of pores in this direction (a cross-section varies from zero to the maximal one), which is smaller than the average pore size measured in image analysis. The lag distance between the peaks is about 0.2 mm, being similar to that observed in Figure 11a,b that refers to the average cross-section of pores and grains in that direction. In z-direction (Figure 11c, black line) the variability is larger than in x- and y- directions, depicted by a cyclic structure with ~3.5 mm wavelength. A cyclic structure with lower amplitude and smaller wavelengths in z-direction “rides” on the main structure with a higher wavelength. A trend in porosity increase with distance is observed, being modelled by a linear regression model (0.166 % porosity per mm), which was removed from the original

Deleted: For S2, the mode peak of the pore size distribution (Fig. 13, blue line) is at 21 μm . A large pore population is also recognized at ~100 μm (Table 2). In total, 45000 pores were analysed. The pore specific surface area (*PSA*) calculated from micro-CT images is 0.136 μm^{-1} (Table 2), which is twice as large as the *PSA* of S1.

Deleted: 10

Deleted: pore size distribution has the main population

Deleted: 1

Deleted: the ...majority at about ...50...3 μm .

Deleted: (Fig. 13, green line) has a mode peak at 223 μm and shows a Gaussian shape (Table 2). In total, 3491 pores were analysed

Deleted:REV Analysis

Deleted: 1

Deleted: in surface...n (with the width of the voxel size, 5 μm) along...each...three orthogonal axis...directions in a maximal volume $6.8 \times 6.9 \times 9.2 \text{ mm}^3$...f S1, having a maximal available segmented volume of $6.8 \times 6.9 \times 9.2 \text{ mm}^3$ scanned with a voxel size of 5 μm (is shown in Figure 11). ...uitable for imaging pore throats that effectively contribute to the flow in S1, Table 2). The slice-by-slice porosity distinguishes the z-direction as having an exceptional behaviour. The histograms of porosity along each direction are different...

Deleted: amplitude of

Deleted: z-direction...eing four times larger than that in x- and y- axes...directions. Along x- and y- axes ...the p...osity varies...luctuates around with...the mean value with no trend, and fluctuates ...ith a “...avelengths”...of about ...0.2 mm in x- and y- directions. SModelling the experimental s...mivariograms (obtained after z-score transformation of the

Deleted: 1

Deleted: of x- and y- axes ...hows...stationarity in that domain

Deleted: 1

Deleted: was fixed to...s set to zero (see Mm...thods Ss...ction

Deleted: data she CT while appear size

Deleted: ... semivariogram model near

Deleted: of coordin

Deleted: variogram

Deleted: fitting

Deleted: axes...directions (Figure 12a,b). A second semivariogram structure...eature is the semivariogram ...aviness (“hole effect”)... i.e. cyclic variance ...haviour with lag distance. The lag distances of the first peaks in the experimental variograms is...re 0.135 and 0.15 mm in x- and y-...directions, respectively. In laminated settings, the distance to the first peak is an indication of the average thickness of the bedding in that direction (Pyrcz and Deutsch, 2003). However, here this length...istance refers to the average thickness...ize of the cross sections of pores in this direction (a cross-section varies between...rom zero to the maxim

1035 porosity (in black) to obtain the porosity residuals (in red, Figure 11c). The experimental semivariogram of
 1036 the residuals (Figure 12c, in red) shows smaller sill and range than the semivariogram of the original porosity
 1037 (in black). The semivariogram in z-direction was fitted with two nested models, a Gaussian model with range
 1038 of 0.1 mm similar to those applied to x- and y- directions, and a hole-effect model with range of 1.63 mm.
 1039 The hole-effect range refers to the average thickness of horizontal layering structures of mm-scale, comprising
 1040 larger or smaller grains, which impose larger or smaller pores between them (see sample cross-section in
 1041 microscopy in Figure 3b). The first trough at 3.4 mm lag distance (Figure 112c) in the curve with a larger
 1042 wavelength, refers to the average thickness of these two layers with higher and lower porosity. A secondary
 1043 structure in the semivariogram of the lower wavelength of ~0.2 mm is similar to those observed in x- and y-
 1044 directions. The larger-scale layering is discerned in z-direction only, and the larger variance of porosity in that
 1045 direction implies an anisotropy in a sandstone S1.

1046 In order to capture this layering pattern, a volume with a side length of at least ~3.5 mm in z-direction
 1047 is required. The ranges in x- and y- directions of ~0.1 mm are associated with the typical pore sizes, which are
 1048 too small to be used in flow modelling, as to predict the permeability reliably, it is necessary to capture the
 1049 three-dimensional tortuosity of the pore space. Alternatively, the REV size from the classic approach, was
 1050 estimated as ~1.2 mm (Appendix A, Figures A1a, b). Therefore, for the flow simulations, we decided to use
 1051 a segmented specimen cube with a maximal available edge length of 2950 μm , scanned with a higher
 1052 resolution of a 2.5 μm , to preserve a consistency between the flow simulations in S1 and S3.

Deleted: values... (in black) to get... obtain the porosity residuals (in red, Figure 11c curve.... The experimental semivariogram of the residuals (Figure 12c, in red) shows smaller sill and range than the semivariogram of the original porosity histogram which the trend was not removed... (in black curve.... The semivariogram in z-direction was fitted nested... with two nested models structures... a Gaussian model with range of 0.1 mm similar to those in... applied to x- and y- directions axes

Deleted: two???

Deleted: porous ... layering structures of mm-scale, comprising . This thickness may be related to ... larger and ... smaller grains deposited in mm-scale width horizontal layering... which subsequently ... impose larger and ... smaller pores between them (see sample cross-section in microscopy in Figure 3b). The first trough at 3.4 mm lag distance (Figure 112c) in the curve with a larger wavelength, an irregular strata

Deleted: ??

Deleted: wavy ... structure in the semivariogram of the lower wavelength of about ... 0.2 mm is similar to those... observed in x- and y- axes... directions. The larger-scale layering is discerned only along ... n z-direction only axis... and the larger variance of porosity in that direction,... implies o... n anisotropy in a sandstone S1, due to less porosity changes in horizontal plane

Deleted: fac... idee... length along z-axis ... f at least ~3.5 mm in z-direction is required. The ranges along ... n x- and y- axes... directions of ~0.1 mm are associated with the size of a... typical pore sizes, which are too small to be used in flow modelling, as to predict the permeability reliably, it is necessary to capture adequately the three-dimensional tortuosity of the pore space. Alternatively, the the REV size for porosity ... rom the classic approach ... was estimated to ... s ~1.2 mm (Appendix B... Figures... B... 1a, b). Therefore, F... or the flow simulations, we decided to use a high resolution of a 2.5 μm on the... entire... segmented specimen cube with an...

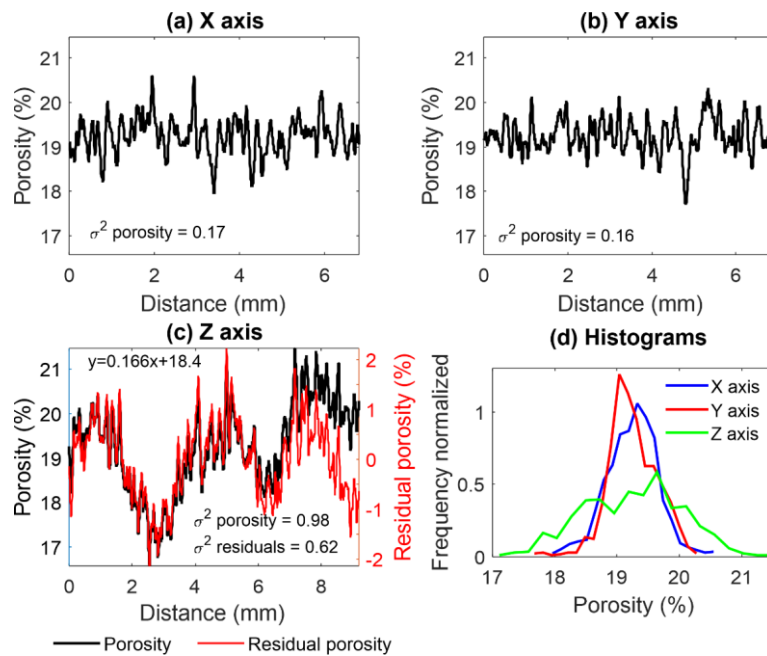


Figure 11: One-dimensional porosity profile of S1 slices evaluated in a) x-direction, b) y-direction and c) z-direction. Investigated volume size is $6.8 \times 6.9 \times 9.2 \text{ mm}^3$. For z-direction, the right y-axis refers to the residual porosity after removing the trend, modelled by a linear regression model. The porosity variations both before (in black) and after (in red) the trend removal are demonstrated. (d) Porosity histograms (z-direction after the trend removal).

Deleted: measured along

Deleted: axis

Deleted: axis

Deleted: axis

Deleted: V

Deleted: X

Deleted: X

Deleted: external

Deleted: variances

Deleted: shown

Deleted: the

Deleted: Z axis

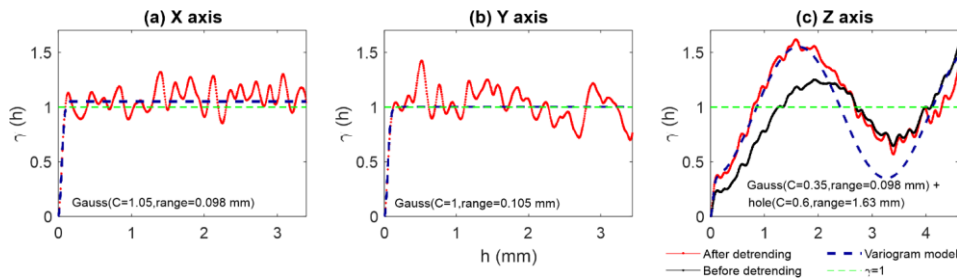


Figure 12: Semivariograms of S1 in a) x-direction, b) y-direction and c) z-direction. z-score transform was applied to the histograms (Figure 11d). For z-direction it was applied before (in black) and after (in red) the trend removal (Figure 11c). The variogram analytical models (Gaussian and hole-effect) are also displayed (dashed blue line), modelled with nugget set to zero.

One-dimensional profiles of porosity were evaluated in sequential slices in the orthogonal directions of S3 with a maximal segmented volume of $3 \times 3 \times 4.2 \text{ mm}^3$ scanned with a voxel size of $2.5 \mu\text{m}$ (Figure 13a-c). Porosity fluctuates around the mean with no trend in all directions. Modelling of the experimental semivariograms (Figure 14) shows stationarity in the investigated domain with range of $\sim 0.087 \text{ mm}$, smaller than that in sample S1 ($\sim 0.1 \text{ mm}$). Cyclic structure contributes to $\sim 40\%$ in the semivariogram variability. The first peak in x- and y-directions are at $\sim 0.115 \text{ mm}$ and in z-direction it is at $\sim 0.103 \text{ mm}$, which relates to the average size of pore cross-section in that direction. The first trough at $\sim 0.2 \text{ mm}$ in all directions, relates to the average cross section of pore and grain together in those directions. Porosity variance in z-direction is ~ 1.08 that is slightly larger than that in other directions (~ 0.9). However a distinct difference in the spatial variability as that in S1 is not observed, which implies that S3 has lower anisotropy characteristics.

Deleted: axis

Deleted: axis

Deleted: a

Deleted: axis

Deleted: Z

Deleted: axis

Deleted: external

Deleted: zero

Deleted: The results of the directional REV analysis of sample S1 conducted on a cube with a $2950 \mu\text{m}$ edge size (1180 pixels) scanned with a resolution of $2.5 \mu\text{m}$ are shown in Figures 9 and 10. The average slice-by-slice porosity analysed in three directions

Deleted: To investigate the nature of the variability in the z-

Deleted: <object><object><object><object><object><object>

Deleted: ¶

Deleted: Figure 9: Directional REV analysis of sandstone S1

Deleted: Fig.

Deleted: (

Deleted:)

Deleted: Figure 113 shows sample S3 one-dimensional porosity

Deleted: l

Deleted: at

Deleted: about

Deleted: 0

Deleted: about

Deleted: axis

Deleted: about

Deleted:

Deleted: axis

Deleted: refer

Deleted: about

Deleted: refers

Deleted: that

Deleted: axis

Deleted: the

Deleted: with

Deleted: ,

Deleted: h

Deleted: for

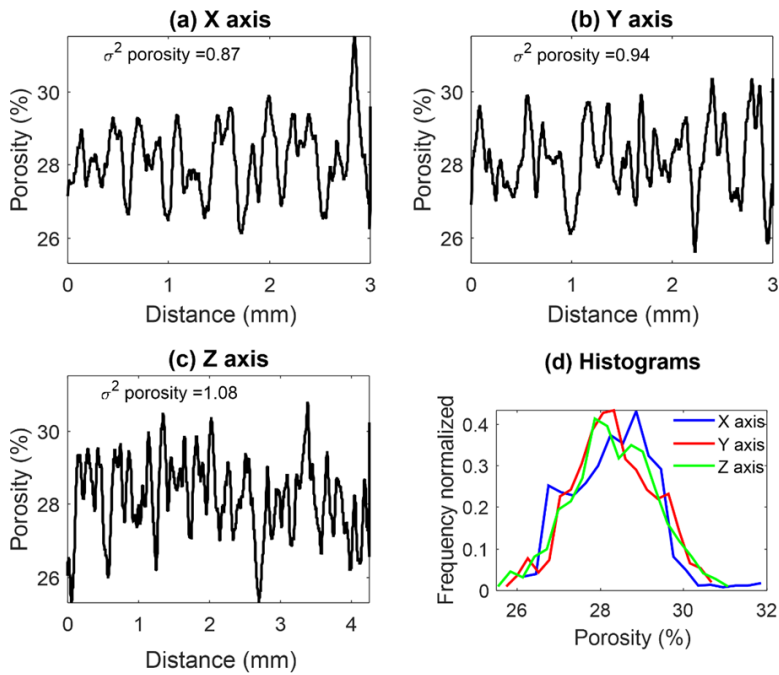
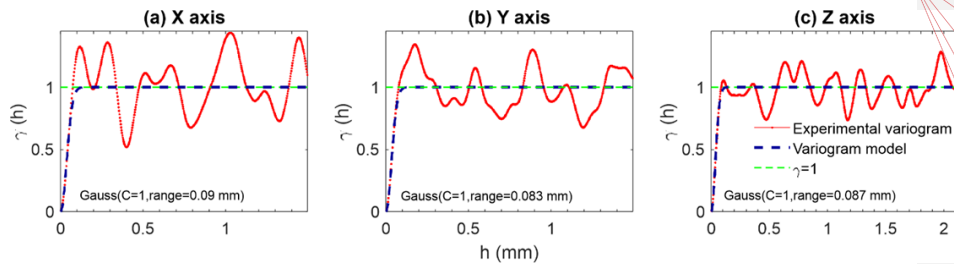


Figure 13: One-dimensional porosity profile of S3 slices evaluated in a) x-direction, b) y-direction and c) z-direction. Investigated maximal segmented volume size is $3 \times 3 \times 4.2 \text{ mm}^3$. d) Porosity histograms.



Deleted: measured along

Deleted: axis

Deleted: axis

Deleted: axis

Deleted: V

Deleted: X

Deleted: X

Figure 14: Semivariograms of S3 in a) x-direction, b) y-direction and c) z-direction. The experimental semivariogram was modelled using Gaussian model (dashed blue line). The semivariogram models are also displayed, modelled with nugget set to zero.

Classic REV porosity analysis (Appendix A, Figure A1e,f) yields REV size with a cube edge length of 875 μm (350 pixels), which is about ten-fold larger than the ranges observed in the semivariogram analysis (~ 0.1 mm, which is a typical size of a pore). For the same reasons used in estimations of REV by the classic approach in S1, the classic REV derived volume was used for the flow modelling in S3.

4.3.2. Quartz wacke sandstone (S2)

Sample S2 is more heterogeneous than S1 and S3 because of the deposition of clay. The sample is visualized in Figure 9b with quartz grains (yellow), pore volume (black), clay matrix (brown) and heavy minerals (white). The clay matrix is distributed in patches. In Figure 15, the porosity of sequential planes in the orthogonal directions is shown together with clay matrix content. In z-direction a clear trend in porosity is observed, which has a negative correlation with the clay content (Figure 16), whereas in the horizontal (x-y) plane there is no clear correlation. This correlation in z-direction implies that the porosity is controlled by the depositional processes. (However, the similar large-scale wavy structures of the clay content in x- and y-directions (Figures 15a,b) may refer to errors originated from the scanning and inversion in the CT acquisition, as x- and y-coordinates are associated with the side boundaries of the cylindrical sample). The trend was removed in all three directions to remain with residual porosity, when the largest trend slope was in z-direction (Figure 17). After the trend removal, the histogram variance in x-direction appears as the largest one, more than twice larger than that in y-direction. Semivariogram analyses were performed (Figure 18) to investigate the spatial variability of the entire available 3D volume ($7.9 \times 6.8 \times 9.2 \text{ m}^3$) scanned with $5 \mu\text{m}$ resolution. Experimental semivariograms were calculated twice: on porosity values, and on porosity residuals (both the porosity and residuals are z-score transformed before calculating the semivariogram). After the trend removal, the range and sill decrease in all directions and especially in z-direction that now reaches the sill. In x-direction, the detrended semivariogram keeps increasing above sill of 1 for the increasing lag distance, thus indicating that the trend was not completely removed, and that the domain is not fully stationary. The semivariograms

Deleted: axis... b) y-directionaxis...and c) a...-directionaxis... The experimental semivariogram was modelled using Gaussian semivariogram...model (dashed blue line) with nugget set to zero... Volume size is $6.8 \times 6.9 \times 9.2 \text{ mm}^3$

Deleted: al...REV porosity analysis (Appendix B..., Figure B...e,f) yields porosity ...EV size with a cube edge length of 875 (350 pixels), which is aboutone...ten-fold larger than the ranges observed in the semivariogram analysis (...0.1 mm, which is a typical size of a pore). For the same reasons used to...n estimations of REV by...the classic approach REV of...n S1, the e classic REV derived volume was used in this study for the flow modelling.

Deleted: Figure 11 shows the results of the directional REV analysis for sample S2 conducted on a cube with an edge length of $2950 \mu\text{m}$ (1180 pixels) scanned with a $2.5 \mu\text{m}$ resolution. Each direction shows a remarkably different trend (Fig. 11a-c). The largest difference between the minimum and maximum slice porosities, 6.57 %, appears in the z-direction (in contrast to 4.5 % and 3.56 % in the x- and y-directions, respectively), and the standard deviation in the z-direction (1.53 %) is approximately twice those in the other two directions (0.86 % and 0.73 %). An increase in porosity with the slice number is observed in the z-direction (Fig. 11c) and is also represented by the trend in the variogramsemivariogram (Fig. 11f). This trend is inversely correlated with the content of clay between the sand grains (Fig. 11a-c, brown curve). The negative correlation coefficient between the porosity and clay matrix in the z-direction (-0.87) (Fig. 11g-i) is larger (in its absolute value) than the corresponding correlation coefficients in the x- and y-directions (-0.34 and -0.03, respectively). Finally, the sill in the directional variogramsemivariogram analysis is not reached for S2 in the y- and z-directions for the cube with an edge length of $2950 \mu\text{m}$. Alternatively, the large difference between the mean and median

Deleted: 4

Deleted: ...The sample is visualized in Figure 9b with quartz grains (yellow), pore volume (black), clay matrix (brown) and hea...

Deleted: there is...clear external ...rend in porosity is observed, which has a negative correlation to...ith the clay content (Figure 16), whereas in the horizontal (x-y) directions...lane there is no clear

Deleted: ing

Deleted: these...- and y-coordinates are associated with are...the side boundaries of the cylindrical sample cylinder axis.... The trend was removed in the...ll three 3...directions to remain with resida...

Deleted: Variogram

Deleted: i...s were performed (Figure 18) to investigate for...he spatial variability over...f the whole...ntire available 3D volume ($7.9 \times X...6.8 \times X$

Deleted: ???

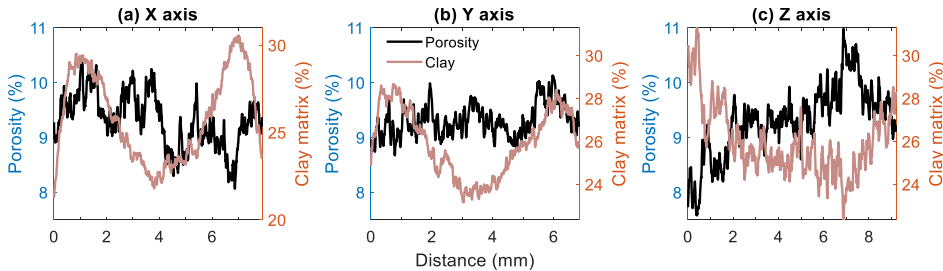
Deleted: variogram

Deleted: the ...porosity values, and on the ...porosity residuals (both the porosity and residuals are for

Deleted: variogram

Deleted: were ...creased...in all directions and especially in z-direction axis...that now reaches the sill. In x-direction axis

504 have multiple structures including cyclicity, therefore, three analytical nested models were used in all
 505 directions; Gaussian, spherical and hole-effect models. The smallest range for the y- and z- directions (Figure
 506 18) is within 0.062-0.07 mm, which refers to the average size of pore cross-section, in agreement with the pore
 507 size distribution from the image analysis (Figure 10), which is smaller than those of the S1 and S3. However,
 508 the contribution of the pore size scale to the overall variability (0.2-0.35) is smaller than that in S1 and S3. The
 509 ranges of the larger-scale cyclic structure are ~1.1 mm and ~2.1 mm in horizontal and vertical directions,
 510 respectively. These length scales relate to an average thickness of the more porous “lenses” originated at the
 511 presence of patchy clay deposition. An intermediate range between those from the Gaussian and hole-effect
 512 models in y- and z- directions are of ~0.35 mm, discerned by a spherical model, may relate to another structure,
 513 associated with a distance between pores.



516 **Figure 15:** Porosity (left) and clay (right) profiles in slices of S2 evaluated in (a) x-direction, (b) y-direction
 517 (c) z-direction. Investigated maximal segmented volume size is $7.9 \times 6.8 \times 9.2 \text{ m}^3$ (see text for more detail).

Deleted: thus

Deleted: used three nested structures

Deleted: between

Deleted: and

Deleted: largest

Deleted: is

Deleted: , with ranges of about

Deleted: refer

Deleted: length

Deleted: se

Deleted: regions which resulted

Deleted: was modelled with about

Deleted: with

Deleted: which assumedly refers

Deleted: possibly due to

Deleted: a typical

Deleted: semivariogramsemivariogramsemivariogram

Deleted: planes

Deleted: axis

Deleted: axis

Deleted: axis

Deleted: ???

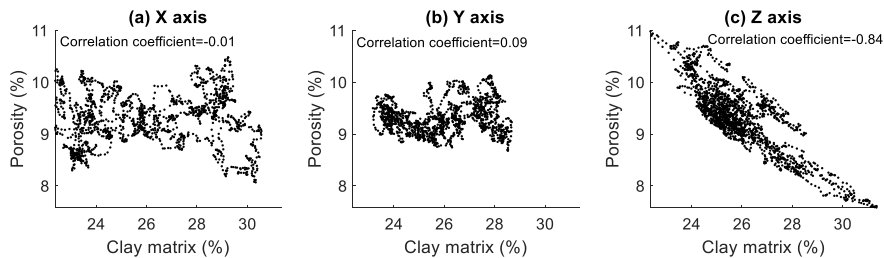


Figure 16: Scatterplots of clay content and porosity in S2 in (a) x-direction, (b) y-direction, (c) z-direction.

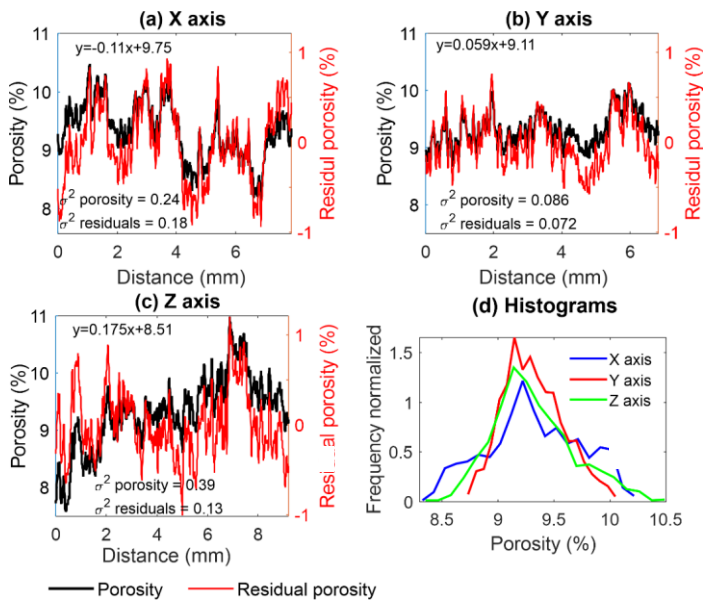


Figure 17: One-dimensional porosity profile of S2 slices estimated in a) x-direction, b) y-direction and c) z-direction. The left vertical axes of the panels refer to the real porosity values, while the right axes to the

Deleted: axis

Deleted: axis

Deleted: axis

Deleted: measured

Deleted: along

Deleted: axis

Deleted: axis

Deleted: axis

Deleted: Volume size is 7.9 X 6.8 X 9.2 m³.

Deleted: i

Deleted: s

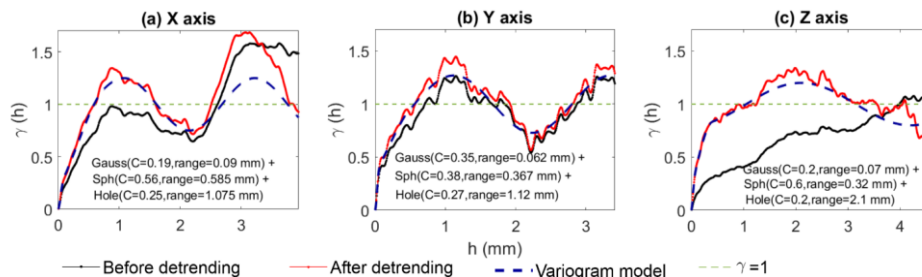
Deleted: and

Deleted: i

residual porosity after removing the trend, modelled by a linear model, shown in each subplot. The variances before and after the trend removal are indicated. (d) Porosity histograms after the trend removal.

Deleted: external ...rend, modelled by a linear model, shown in each subplot. The variances before and after the trend removal are shown...

Deleted: semivariogram



Deleted: Variogram

Deleted: axis ...irection, b) y-axis...irection and c) a-axis...irection. z...score transformation was applied to the histogram, before (black) and after (red) the trend removal

Deleted: variogram

Deleted: exponential variogramsemivariogram

Deleted: from...y the classical...porosity-based REV approach (Appendix B...

Deleted: Fig.

Deleted: B...1c, d) show that there is a large difference between the mean and median porosities... Together with the external trend in z-axis...irection (Figure 15) in the scale

Deleted: implies tha

Deleted: i

Deleted: also cannot be reached

Deleted: these volume...2.9 X 6.8 X 9.2 m³... As a result, flow modelling could not be conducted for

Deleted: semivariogram

Deleted: W...here is an opportunity to e...investigate the... sample heterogeneity of S2 by analysing semivariograms for the sequential surface...lice porosity of the same volume size

Deleted: l

Deleted:the semivariograms were modelled (machine-wise), and threshold ... threshold was set such that only to ...the stationary semivariograms were analysed to calibrate the range of correlation. This threshold is associatedwhich were modelled...with sills between 0.9 and 1.1, were taken in consideration in analyses of the range of correlation

Deleted: cube... (Figure 19a-c), with an edge size 2-3 times larger than the cyclic range found (1.1 mm in x- and y- axes...irections, 2.1 mm in z- axis

Deleted: l

Deleted: full...ntire domain (7.9 × 6.8 × 9.2 mm³), the spherical model was used, and the percentages which...f passing...the threshold were 39, 33 and 12 % in x-, y- and z-axes...irections, respectively. The average residual variances a

Figure 18: Semivariograms of S2 in a) x-direction, b) y-direction and c) z-direction. z-score transformation was applied to the histogram, before (black) and after (red) the trend removal. The experimental semivariogram was also modelled using nested Gaussian, spherical and hole-effect models (dashed blue line) with nugget set to zero. The calibrated sill and range are shown (see text for more detail).

Alternatively, the large difference between the mean and median porosities is identified by the classic porosity-based REV approach (Appendix A, Figure A1c, d). Together with the porosity trend in z-direction (Figure 15) in the volume under investigation ($7.9 \times 6.8 \times 9.2 \text{ m}^3$), there is no REV in S2. As a result, flow modelling could not be conducted in sample S2.

Additionally, there is an opportunity to investigate a heterogeneity of S2 by analysing semivariograms for the sequential slice porosity for the multiple sub-volumes of the volume investigated above ($7.9 \times 6.8 \times 9.2 \text{ m}^3$ size, Figure 19). For each sub-volume cube (with 3.5, 1.2, and 0.5 mm edge size) the trend in porosity was removed and the histogram was standardized. A threshold was set such that only the stationary semivariograms were analysed to calibrate the range of correlation. This threshold is associated with sills between 0.9 and 1.1.

For 3.5^3 mm^3 sub-volumes (Figure 19a-c), with an edge size 2-3 times larger than the cyclic range found (1.1 mm in x- and y- directions, 2.1 mm in z- direction, Figure 18), and which is about half the size of the entire domain ($7.9 \times 6.8 \times 9.2 \text{ mm}^3$), the spherical model was used, and the percentages of passing the threshold were 39, 33 and 12 % in x-, y- and z-directions, respectively. The average residual variances were

0.39, 0.34 and 0.59, respectively. Experimental semivariograms were chosen randomly for the observation (Figure 19a-c). The semivariograms vary in all directions (indicated by the variability in slopes till reaching the ranges), when the calibrated ranges averaged to $204 \pm 65 \mu\text{m}$, $202 \pm 69 \mu\text{m}$ and $334 \pm 137 \mu\text{m}$, for x-, y- and z- directions, respectively. The large cycles of more than 1 mm in the wavelengths are not consistent. Overall, for 3.5^3 mm^3 sub-volume sizes, the ranges in x- and y-directions do not vary much, but z-direction shows a smaller percentage of sub-volumes passing a sill threshold and a larger variance, which points on more heterogeneous and irregular structure of the pore space.

Modelled 1.2^3 mm^3 sub-volumes (Figure 19d-f) are smaller than the cyclic length calibrated for the entire domain (Figure 18). Gaussian model, which fits the smallest range structures in the entire domain, was used. The percentage of the sub-volumes which passed the threshold were 35, 42 and 17 % in x-, y- and z- directions, respectively. The average residual variances were 1.76, 1.59 and 3.27, respectively. The semivariograms initial slopes (Figures 19d-f) vary mainly in z-direction, when the calibrated ranges averaged to $79 \pm 18 \mu\text{m}$, $72 \pm 19 \mu\text{m}$ and $187 \pm 120 \mu\text{m}$ in x-, y- and z- directions, respectively.

For the smallest 0.5^3 mm^3 sub-volumes (Figure 19g-i), the percentages which passed the threshold were 27, 30 and 11 % in x-, y- and z- directions, respectively. The average residual variances were 4.6, 4.8 and 12.3. The semivariogram initial slopes (Figure 19g-i) vary more in z-direction, when the calibrated ranges averaged to $43 \pm 8.3 \mu\text{m}$, $43 \pm 9 \mu\text{m}$ and $91 \pm 44 \mu\text{m}$ in x-, y- and z- directions, respectively.

To summarize, small percentages of sub-volumes which passed the stationarity threshold imply that the sub-volumes of those sizes are not representative for S2. For the increasing sub-volume sizes the range increases (Figure 19), because larger sub-volume is composed of smaller sub-volumes with very different structure characteristics, including those that have not passed the threshold. The larger range identified in z-direction is assumed to be related to an irregular structure in that direction, whereas in x- and y- directions the heterogeneity is milder. The larger porosity variance in z-direction implies an anisotropy due to less constrictions to flow in the horizontal plane.

Deleted: For observation

Deleted: The

Deleted: ...-c). The semivariograms slopes ...ary in all directions (indicated by the variability in slopes till reaching the ranges), when the calibrated modelled by average...ranges averaged toof... $204 \pm 65 \mu\text{m}$, $202 \pm 69 \mu\text{m}$ and $334 \pm 137 \mu\text{m}$, forin...x-, y- and z- axes...irections, respectively. The large cycles of more than 1 mm in the wavelengths are not consistent in length... Overall, for 3.5^3 mm^3 sub-volume sizes, the ranges in x- and y-directions do not vary much, but in ...axis...irection shows a smaller percentage of sub-volumes passing a sill threshold passing ...nd a larger variance, which infer...oints on more heterogeneous and irregular structure of the pore distribution

Deleted: For

Deleted: 1

Deleted: found...alibrated for the whole

Deleted: 1

Deleted: found ...its for...the smallest range structures in the entire domain, was used. The percentage of the sub-volumes which passed the threshold were 35, 42 and 17 % in x-, y- and z-axes...irections, respectively.he average residual variances a...ere 1.76, 1.59 and 3.27, respectively. The semivariograms initial slopes (Figures 19d-f) now ...ary mainly in z-axis...irection, when the calibrated ranges averaged toand modelled by average ranges of... $79 \pm 18 \mu\text{m}$, $72 \pm 19 \mu\text{m}$ and $187 \pm 120 \mu\text{m}$ in x-, y- and z- axes

Deleted: st

Deleted: axes...irections, respectively. The average residual variances a...ere 4.6, 4.8 and 12.3. The semivariogram initial slopes (Figure 19g-i) ...ary mainly...more in z-axis...irection, when the calibrated ranges averaged toand modelled by average ranges of... $43 \pm 8.3 \mu\text{m}$, $43 \pm 9 \mu\text{m}$ and $91 \pm 44 \mu\text{m}$ in x-, y- and z- axes

Deleted: ies...that a ...hedomain...sub-volumes of thoset...sizes is...re not representative for S2. For the increased

Deleted: 1

Deleted: by...f smaller sub-volumes with very different structure characteristics, including those that have not passed the threshold. The larger range calculated...identified in z-axis...irection is assumed to be related to an irregular structure in that direction, whereas in x- and y- axes...irections the heterogeneity is milder. The larger porosity variance in z-direction implies o

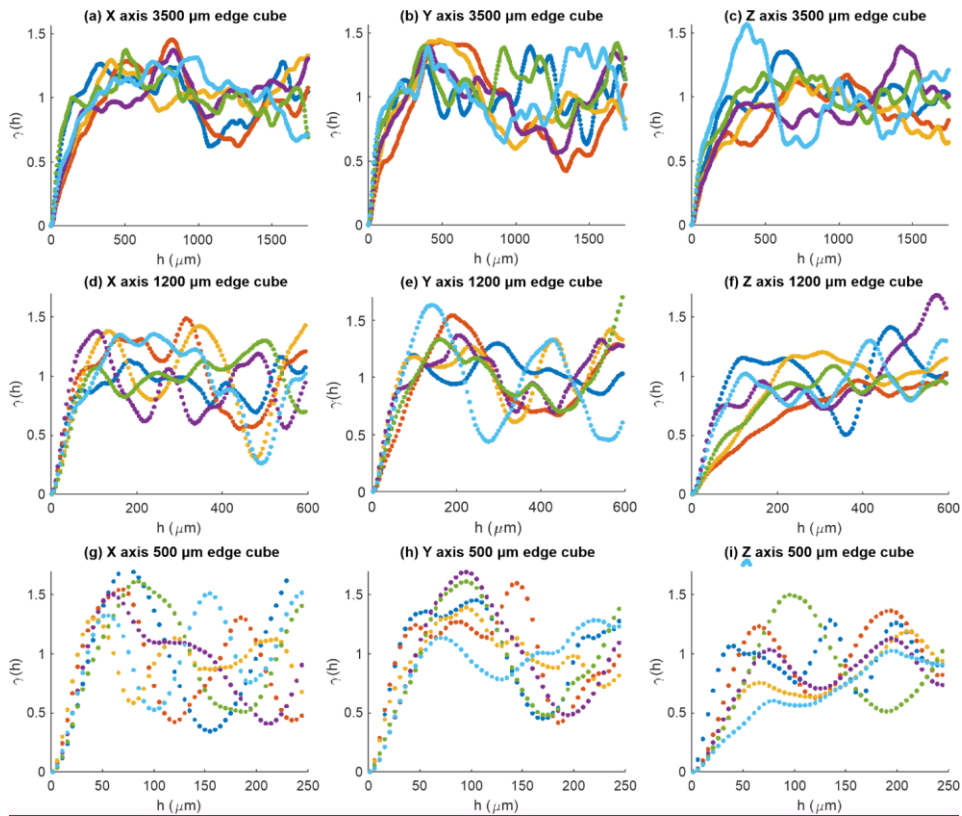


Figure 19: Experimental semivariograms of sub-volume cubes with 3.5^3 mm^3 (top row), 1.2^3 mm^3 (middle row) and 0.5^3 mm^3 (bottom row) edge sizes, in x -direction (left column), y -direction (middle column) and z -direction (right column), respectively.

Deleted: s

Deleted: 3.5

Deleted: axis

Deleted: x

Deleted: axis

Deleted: axis

1796 **4.4. Flow modelling at the pore scale**

1797 Fluid flow was modelled at the pore scale in two different micro-CT-scanned geometries: 1) a full cube

1798 of sample S1, and 2) sample S3 within its REV dimensions (Table 3), imaged with 2.5 μm voxel size.

1799 Modelling of the 3D geometry of sample S2 was not performed due to its non-stationarity which did not allow

1800 finding the REV in the investigated domain.

1801 **Table 3. Porosity losses in S1 and S3 over the course of applying the extended computational workflow (Figure**

1802 **2).**

Sample	Sample size (mean mesh edge size) [μm]	CT segmented image porosity (%)	Connected porosity (%)	Mesh porosity (%)	Gas porosity (%)
S1 (entire sample, 1180 voxels)	2950 (14)	17.5	15.6	13.6	28
S3 (REV, 350 voxels)	875 (5)	28.3	27.9	25.9	31

1803

1804 The porosity of the meshed domain of sample S1 is 13.6 % (in contrast to 17.5 % in the segmented

1805 image, Table 3), and the mesh edge length is 14 μm along the pore walls. The observed porosity loss results

1806 from disconnecting narrow pore throats from the connected cluster imaged with a 2.5 μm voxel size due to

1807 the use of a 14 μm mesh size (the lowest possible for our computational needs). A maximum Reynolds number

1808 of $Re = 0.084$ was used to guarantee the simulation in a creeping flow regime.

1809 The symmetrized permeability tensor, $\bar{\kappa}$, was obtained as follows (Table 2):

1810
$$\bar{\kappa}_{sym} = \begin{pmatrix} 420 & 66.3 & 1.91 \\ 66.3 & 344 & 12.8 \\ 1.91 & 12.8 & 163 \end{pmatrix}$$

1811 The permeability tensor is anisotropic, with κ_{zz} being more than half κ_{xx} and κ_{yy} . This result is in

1812 agreement with the appearance of horizontal banding with higher cementation derived from the semivariogram

1813 analysis (Figure 11c).

1814 The porosity of the meshed domain of sample S3 is 25.9 % (in contrast to 28.3 % in the segmented

1815 image, Table 3), and the mesh edge length is 5 μm along the pore walls. A maximum Reynolds number of

Deleted: 4.3. Fluid

Deleted: f

Deleted: including two adjacent parts possessing relatively low (0-250 voxels) and high (250-1180 voxels) porosities (Fig. 9c),

Deleted: to the reasons

Deleted: the

Deleted: to

Deleted: detailed above.

Deleted: A constant pressure gradient of $2.424 \left[\frac{\text{Pa}}{\text{mm}} \right]$ between the inlet and outlet boundaries was applied in all the simulations for consistency.¶

Deleted: ¶

Deleted: Fig.

Deleted: variogram

Deleted: Fig.

Deleted: 10f

1832 $Re = 0.22$ was used to guarantee the simulation in a creeping flow regime. The symmetrized permeability
1833 tensor is close to isotropic (Table 2):

1834
$$\bar{\kappa}_{sym} = \begin{pmatrix} 4517 & 5 & 38 \\ 5 & 4808 & 547 \\ 38 & 547 & 4085 \end{pmatrix}$$

1835 The tortuosity of S3 in the x-, y-, and z- directions varies in the range [1.39, 1.47] (Table 2), and the largest
1836 value is observed in the z-direction, which is in agreement with the lowest permeability in the z-direction.

1837 **5. Discussion**

1838 **5.1. Validation of permeability by micro- and macro-scale rock descriptors**

1839 Each of the evaluated micro- and macro-scale rock descriptors supplies qualitative information about the
1840 sample permeability (Tables 2-3), which is used to validate the multi-methodological approach presented in
1841 this paper. Specifically, the increasing mercury effective saturation with increasing pressure shows a similar
1842 pore throat size distribution curve slope for sandstone samples S1 and S3 in the macro-pore throat range
1843 (Figure 7), suggesting that these samples have similar structural connectivity. However, S1 has a smaller
1844 volume fraction of pore space available for fluid flow that is controlled by macro pore throats (i.e., 81 % in
1845 S1 vs. 93 % in S3, Figure 7) due to its higher contents of silt, clay, and Fe-ox cement. The intermediate layer
1846 (S2) with 19 % porosity comprises more fines, which form a clay matrix (Table 2) due to poor grain sorting
1847 and smaller mechanical resistance of clay to pressure under the burial conditions. Only ~15 % of the pore
1848 volume fraction in S2 is controlled by bottle-neck macro pore throats (Figure 7). However, the characteristic
1849 length of S2, 12.3 μm (Table 2), indicates that macro-pore connectivity is still possible even when the pore
1850 space consists mainly of sub-macro-scale porosity. This 0.15 volume fraction is in agreement with Harter
1851 (2005), who estimated a volume fraction threshold of 0.13 for correlated yet random 3D fields required for
1852 full interconnectivity.

1853 The value of the connectivity index of S3 (10) is approximately three times higher than that of S1 (3.49),
1854 while both rocks are defined as moderately sorted sandstones (Table 2). This difference is due to S1 having a
1855 smaller number of inequivalent loops within the pore network than S3, leading to smaller β_1 values in Euler
1856 characteristics (see Supplementary material for more detail). Inequivalent loops are correlated with pore
1857 throats; their number is affected by the resolution of the CT image and by the partial volume effect at grain

Deleted: PTSD

Deleted: .

Deleted: Fig.

Deleted: with 19 % porosity

Deleted: .

Deleted: bad

Deleted: most likely affected by the

Deleted:

Deleted: of this sample

Deleted: (Table 2)

Deleted: .

Deleted: A field tracer test in a sand and gravel aquifer derived effective porosity of for transport of approximately 0.17 (Stephens et al., 1998).

Deleted: (Appendix C)

1873 surfaces (Cnudde and Boone, 2013; Kerckhofs et al., 2008), where some voxels could be identified as grains
1874 and thus “clog” the small pore throats. Artefact porosity loss is apparent for S1, where the IP is 17.5 % (in
1875 contrast to the CT porosity of 23.5 % predicted from MIP, Table 2). The connectivity index of S2 (0.94, Table
1876 2) is lower than those of both S1 and S3 because of the clay matrix, which clogs pores. The effect of the partial
1877 volume effect on the image connectivity and on the preservation of small features was reviewed by Schlüter
1878 et al. (2014).

1879 A correlation was found between the grain size and the amount of Fe-ox cement in S1 evaluated at each
1880 slice along the z-direction (from the image analysis, [Figure 20](#)). Exceptionally large grains are detected
1881 (indicated by the red rectangle) near the cemented region at ~750 µm. Large grains and a relatively high
1882 amount of cement can also be observed in the S1 thin section ([Figure 3b](#)). Large grains cause large pores and
1883 generate relatively permeable horizons through which water flow and solute transport can become focused
1884 (McKay et al., 1995; Clavaud et al., 2008), supplying iron solutes. We suggest that a vadose zone was formed
1885 after flooding events, where the water flow mechanism could have changed from gravity dominated to
1886 capillary dominated. Water then flowed due to capillary forces along grain surfaces towards regions with
1887 larger surface areas, and iron solutes precipitated in a reaction with oxygen available in the partly saturated
1888 zone. We suggest that with time, this cementation mechanism caused a decrease in the pore throat size near
1889 the preferential path, while the preferential path with a low surface area remained open, eventually generating
1890 the observed anisotropic flow pattern.

Deleted: Fig.

Deleted: 14

Deleted: Fig.

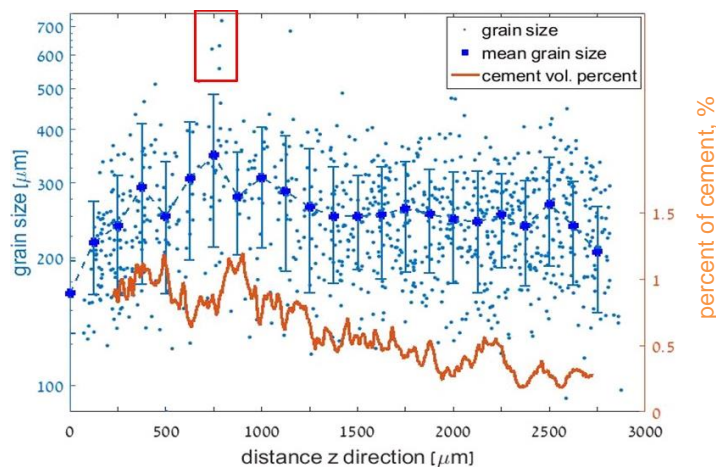


Figure 20. Grain size scattering and Fe-ox cement content in sandstone S1 in slices along the z-direction.

In this respect, permeability anisotropy in sandstones at a small scale is usually attributed to the shape or preferential orientation of grains and pores (e.g., Sato et al., 2019) and to a heterogeneous distribution of cementing material at grain contacts (Louis et al., 2005). At a larger scale, a higher degree of permeability anisotropy is associated with the presence of localized beds, foliation, and compaction bands that constitute barriers to flow in the perpendicular direction (see Halisch et al., 2009; Clavaud et al., 2008 and references therein). Clay-free and cement-free layers constitute the main avenues for flow in the parallel direction (e.g., Figure 12).

The semivariogram analysis of S1 reveals horizontal porosity bands with a thickness of ~ 1.6 mm (Figure 12c) that are composed of larger or smaller grains with larger or smaller pores between them, correspondingly. Flow modelling in the specified REV shows anisotropy (Table 2) and an average permeability value of 310 mD that is close to that derived from MIP (330 mD). However, the average permeability is lower than the average experimental gas permeability (~ 543 mD); this difference should be related to the loss of porosity due to limitations on the CT resolution, image processing and meshing (Table 3, see Sect. 5.2 for more details).

Deleted: 14

Deleted: .

Deleted: 14

Deleted: directional

Deleted: REV

Deleted: period

Deleted: 2

Deleted: about

Deleted: perpendicular to the z-direction

Deleted: .

Deleted: 10c

Deleted: , f

Deleted: sub-domains

Deleted: exhibiting

Deleted: high and low Fe-ox cementation

Deleted: and

Deleted: high affected on

Deleted: and

927 In contrast, no banding was detected in S3 by the semivariogram analysis (Figures 13-14). Flow
 928 modelling and upscaling to the macro scale indicate an isotropic sample (Table 2). However, the modelled
 929 permeability (~4500 mD) is ten times higher than the MIP-derived permeability (466 mD, Table 2). Gas
 930 permeability measurements indicate anisotropy, yielding permeabilities of 4600 mD in the x-y plane and 220
 931 mD in the z-direction (with an anisotropy ratio of ~20, defined here as κ_x/κ_z , e.g., Tiab and Donaldson, 2004).
 932 For comparison, the values of this ratio obtained from experimental permeability measurements were ~1.2 for
 933 Bentheim sandstone (Louis et al., 2005), ~1.7-2.5 for a sandstone within the Cretaceous Virgelle Member,
 934 Alberta, Canada (Meyer and Krause, 2001), and ~8.5 for Berea sandstone (Sato et al., 2019). However, in
 935 some laboratory measurements conducted parallel to the layering (in the x-y plane), poorly cemented grains
 936 in S3 could dislocate from the weakly consolidated sample due to the application of a pressure gradient. This
 937 could have resulted in a higher measured gas flux and thus a higher permeability parallel to the layering,
 938 yielding a high anisotropy. In this case, the permeability upscaled from the modelling in S3 is also exaggerated.

939 Alternatively, the disagreement between the laboratory-determined permeability (perpendicular to the
 940 layering) and the permeability obtained from the flow modelling (Table 2) may also stem from the small
 941 dimension of the modelled domain (cube edge length of ~0.875 mm), which may not have included the textural
 942 features that constrain fluid flow on a larger scale (e.g., Figure 5d). Nevertheless, additional permeability
 943 simulations on equivalently REV sized segmented sub-volumes of S3 and on the entire S3 have been
 944 conducted, to ensure consistency of the estimated REV size. These simulations have been performed by using
 945 the FlowDict module (Linden et al., 2015; 2018) of the GeoDict toolbox (Wiegmann, 2019) currently available
 946 at our disposal. Pre-processing as well as boundary conditions are identical to those used in COMSOL setup
 947 described in the Methods Sect. Sub-volumes locations, detailed permeability tensor simulation results, as well
 948 as evaluated 3D image porosity data, can be found within the Appendix C. The permeability results are in a
 949 good agreement with previously conducted flow simulations (Table 2). The average permeability derived from
 950 all REV-sized sub-volumes is ~4381 mD, compared to the average permeability of ~4500 mD simulated upon
 951 the entire S3 geometry. This, again, is in a good accordance with the permeability of S3 measured parallel to
 952 the layering (Table 2). These simulations conducted in the sub-samples and in the full sample S3 (Appendix
 953 C), strengthen our conclusion that those may not have included the textural features that constrain fluid flow
 954 on a larger scale of the samples tested in the gas permeametry. Similarly, the differences with the permeability
 955 estimated by MIP seem to originate from the same reason.

Deleted: directional REV

Deleted: ...res 12

Deleted: , which agrees with the isotropy derived from the

Deleted: variogram

Deleted: semivariogram analysis

Deleted:

Deleted: were ...ould dislocated

Deleted: Fig.

Deleted: in order ...o ensure consistency and repeatability ...f the estimated REV size. Due to licensing issues of the meshing software used in this study, ...heseadditional...simulations have been conducted...

Moved down [2]: (Linden et al., 2015; Linden et al. 2018)

Moved (insertion) [2]

Deleted: with regards ...o those...used in COMSOL sS...tup described in the Mm...thods Ss...ction... Principle sampling ...ub-volumes locations of the sub-volumes... as well as ...etailed permeability tensor simulation results and...as well as evaluated 3D image porosity data, can be found within the Aa...pendix Cof this manuscript (@Regina: please implement as intended and meaningful)... The permeability results are in very... good agreementaccordance...to the...ith previously conducted flow simulations experiment...Table 2). The average permeability derived from all REV-sized sub-volumes is about ...4381 mD, compared to the average permeability of about...500 mD simulated upon the entire S3 geometry. This, again, is in excellent... good accordance to...ith the measured data...rmeability of S3 measured parallel to the layering (Table 2). These simulations conducted in the sub-samples and in the full sample S3 (Appendix C), strengthen our conclusion that those may not have included the textural features that constrain fluid flow on a larger scale of the samples tested in the gas permeametry. Hence...imilarly, the differences compared...ith to...the permeability estimated by MIP seem to originate from the same reasonthe underlying capillary tube model (API RP 40), as well as from non-representatively sampled pieces of sandstone

For sample S2, both classic REV and semivariogram analyses indicated an REV size larger than the investigated sample size (Figure 18, Figs. B1 c,d in Appendix A). For this reason, the analytical programme formulated in our study cannot entirely be applied to S2 due to the impossibility of determining a reliable REV and hence conducting pore-scale flow modelling. As a result, although sample S2 represents a common sandstone, it is very heterogeneous in nature, and a sample larger than at least 9 mm (which is a maximal size of the tested domain) is required to capture its REV. The MIP-derived permeability is 4 mD; this low permeability is due to a clay-rich matrix that encloses substantial void space (Hurst and Nadeau, 1995; Neuzil, 2019). The gas permeability of the quartz wacke layer (S2, ~4.6 mD on average) is approximately two orders of magnitude lower than that of the quartz arenite layers (S1 and S3, Table 2). The permeability anisotropy ratio of S2 is ~2.8. The high inverse correlation between the porosity and clay matrix content enhanced in the z-direction (Figures 15c, 16c) suggests that the clay matrix pattern appears as horizontal layering, thus generating the observed anisotropy.

Finally, non-marine sandstones of Lower Cretaceous age (as well as sandstones in general), feature a big complexity and variability in their characteristics, as immediately seen even from a comparison of our samples S1, S2, S3 from the same outcrop (Table 2). The distinctions usually stem from the different depositional and diagenetic conditions. For instance, low porosity of Wealden quartz arenite sandstones from Weald Basin within Ashdown and Wadhurst Clay Fms. in southeast England, ranges between 6.3 % and 13.2 %, while permeability between 0.4 mD and 11.9 mD (Akinlotan, 2016), suggested to be controlled mainly by grain sizes, grain shapes, and sorting that are directly linked to their depositional environment. Average porosities of 3.06 % and 0.19 % were evaluated in medium and fine grained tight gas sandstones, correspondingly, from Lower Cretaceous Dengloulou Fm. in the Songliao Basin, China (Zhang et al., 2019). Alternatively, a secondary porosity of 4 % to 22 % was generated by acidic fluids acting in the compactional regime, destructing a high primary porosity in sandstone of Lower Cretaceous Shurijeh Fm. in the eastern Kopet-Dagh Basin in NE Iran (Moussavi-Harami and Brenner, 1993), while significant average porosity and permeability of 20 % and 3700 mD, respectively, were quantified in the Masila Block, Upper Qishn Fm. of the Lower Cretaceous Age, Republic of Yemen (Harding et al., 2002). Multi-methodological approach suggested in this study is applicable to all those sandstones with broad ranges of their textural, topological and mineralogical characteristics and should lead to their accurate petrophysical characterization.

Deleted: much

Deleted: Fig.

Deleted: 11

Deleted: B

Deleted: paper

Deleted: of a very heterogeneous nature

Deleted: 3

Deleted: 2

Deleted: in

Deleted: Fig.

Deleted: 11

Deleted: g-i

5.2. Upscaling permeability: accuracy of the extended computational workflow

The extended computational workflow (Figure 2) serves as the main tool in this study for upscaling permeability from the pore-scale velocity field. The accuracy of each step in the workflow affects the ultimate result.

Following the steps of the workflow, a micro-CT image resolution of 2.5 μm limits the reliability of the representation of the porous medium and defines the lower pore identification limit using this method. As an example of this limitation, the SSA (bulk specific surface area) calculated by MIP is larger than the PSA (pore specific surface area) calculated by micro-CT image analysis in all the samples (Table 2), although the pore volume is always smaller than the bulk volume. The PSA from micro-CT is limited by the image resolution and therefore does not consider relatively small pores with large surfaces. The PSAs of S1 and S3 are similar, but the SSA (from MIP) of S1 is 20 times larger than that of S3 because S1 has a larger surface area at small pores created mainly by Fe-ox cement (compare Figure 3c-f for S1 to Figure 5c for S3). S2 shows a PSA twice as large as that of S1 due to the presence of clay and clay matrix with large surface areas.

Image processing and segmentation were applied in this study to recover the image geometry, which was blurred by noise or affected by the partial volume effect (see Sect. 3). Then, the loss of pore space due to the resolution limits was estimated in this study from the amount of mercury filling the pores with diameters equal to the resolution limit (Figure 7a). After segmentation, sample S1 had a segmented image porosity of 17.5 % and a CT predicted porosity of 23.5 % from MIP (Tables 2, 3). Therefore, the difference in porosities generated by the partial volume effect in the image processing scheme (e.g., Cnudde and Boone, 2013) is a significant component of error, especially for small structures, such as pores with a large surface area-to-volume ratio. In contrast, the image porosity of S3 after segmentation was 28.3 %, which is close to the porosity of 30.4 % estimated from MIP (Tables 2, 3). This is a result of the very small degree of cementation and the absence of Fe-ox flakes in the majority of the sample pores, leading to the small contribution of the partial volume effect. In comparison, a fine-grained and well-sorted Lower Cretaceous Fm. sandstone from Heletz Field (e.g., Figure 1a) (Tatomir et al., 2016) comprising clay and calcite had MIP and micro-CT porosities of 26.7 % and 20.9 %, respectively.

An additional source of inaccuracy is the use of a porosity-based REV for permeability approximations. Mostaghimi et al. (2013) showed that for CT images of sandpacks (homogenous samples), the porosity-based

Deleted: Fig.

Deleted: (Fig. 2)

Deleted: Fig.

Deleted: Fig.

Deleted: Fig.

Deleted: Fig.

2110 REV had an edge length of 0.5 mm, whereas the permeability-based REV was twice as large. Moreover, the
2111 porosity- and permeability-based REV in images of bead packs derived by Zhang et al. (2000) had edge
2112 lengths of 1.71 and 2.57 mm, respectively. According to Mostaghimi et al. (2013), larger REV values for
2113 permeability rely on contributions from the tortuosity and connectivity of pore spaces, whereas the larger REV
2114 values of Zhang et al. (2000) may be related to the heterogeneity of the sample.

2115 Additional simulations performed in S3 presented in Appendix C support this conclusion. Both porosity
2116 and permeability demonstrate a good agreement with those estimated with flow simulations in the REV
2117 presented in Table 2, thus confirming a representativeness of the estimated REV and a continuity of these
2118 characteristics over the chosen sample. However, the differences in porosity between the sub-samples and the
2119 full sample are smaller than the corresponding differences in permeability (Appendix C), as anticipated from
2120 a porosity-based REV derivation discussed above.

2121 Further, textural bedding at ~1.6 mm scale dominates the porosity anisotropy in S1 (Figure 12c,
2122 evaluated by the semivariogram), and by ~3.5 mm average thickness of two adjacent more and less porous
2123 beddings together. To upscale to permeability reliably, the REV domain should be sufficiently large such that
2124 it is bounded from below by the scale of the textural bedding (i.e., an edge length > 3.5 mm) but should not be
2125 larger than necessary to optimize computational efficiency (while remaining within the same scale of
2126 heterogeneity, i.e., at the macro scale). As a result, a REV with an edge length of ~2950 μm (~1.5 times larger
2127 than the scale of textural bedding) was chosen in the current study in sample S1. For comparison, in other
2128 studies, the edge lengths of REV in sandstones were 0.68 mm (Ovaysi and Piri, 2010), 0.8 mm (Mostaghimi
2129 et al., 2013), and 1.2 mm (Okabe and Oseto, 2006; Tatomir et al., 2016). The larger REV size in the current
2130 study found by the semivariogram (rather than by the classic isotropic approach) was due to the textural
2131 features revealed in the z-direction.

2132 Another source of inaccuracy is the geometry used for the flow model. The geometry considered in this
2133 study included only the pore network connecting six faces of the REV cube. Other pore spaces in the REV
2134 disconnected from the main network were deleted (because all paths smaller than the resolution were
2135 prescribed as grain pixels due to the partial volume effect), thus resulting in the smaller effective size of the
2136 simulation domain. The image porosity of sample S1 was 17.5 %, whereas its connected porosity was
2137 estimated as 15.6 % (Table 3), while those of sample S3 were 28.3 % and 27.9 %, respectively.

Deleted: It might be noticed, that the calculated semivariograms do not feature any nugget effect. Obviously, the nugget effect can be attributed to measurement errors or spatial sources of variation at distances smaller than the sampling interval or both. Measurement error occurs because of the error inherent in measuring devices. Natural phenomena can vary spatially over a range of scales. Variations at microscales smaller than the sampling distances will appear as part of the nugget effect. Nevertheless, this is more or less impossible to achieve for “mining” spatial data from μ -CT images since we have a fixed resolution limit. Hence, all variation below that “hard resolution boundary” is “invisible” for the variography analysis. This clearly is a drawback of the image analysis, and hence it is important to gain detailed understanding of the scales of spatial variation from multiple methods. Accordingly, the smallest lags are related to the resolution, i.e. the smallest segmented feature of the 3D scan. ¶

Deleted: a 2

Deleted: about

Deleted: .

Deleted: 10f

Deleted: directional REV

Deleted: , e.g., Halisch, 2013

Deleted: porous

Deleted: .

Deleted: 2

Deleted: consisting of an

Deleted: directional approach

2165 Furthermore, the mesh was generated by taking a trade-off between the size of the mesh elements (4
 2166 elements in the smallest pore throat) and computational limits into account while coarsening the mesh
 2167 elements towards the pore centre. The connectivity between pores with very fine pore throats that could not
 2168 be replaced by mesh elements could be lost, resulting in the loss of those pores in the calculations. In sample
 2169 S1, the porosity used in the simulation was approximately 50 % smaller than the porosity estimated by gas
 2170 porosimetry (Tables 2, 3). In contrast, the porosity used in the simulations in S3 was mostly preserved,
 2171 comprising ~84 % of that estimated in the laboratory.

2172 For comparison, in the fine-grained sample of the Lower Cretaceous sandstone from Heletz Field in
 2173 Israel (Figure 1a), which has grain size characteristics similar to those of S1 but with higher clay and additional
 2174 calcite contents (Tatomir et al., 2016), the permeability upscaled from micro-CT flow modelling (conducted
 2175 by the same simulation method as that in the current study) exceeded the gas permeability by a factor of ~6.
 2176 This could be related either to the small REV for the flow model or to the reduction in the specific surface
 2177 area by image processing and meshing (Mostaghimi et al., 2013) for the flow modelling.

2178 Finally, the upscaling process from the flow modelling successfully predicted the permeability
 2179 anisotropy ratio of ~2.3 in S1, as discussed above. For comparison, the permeability anisotropy ratio evaluated
 2180 using micro-CT flow monitoring in clay-free sandstones (Clavaud et al., 2008) had a mean value of ~2.5
 2181 (ranging from ~1.7 to ~5.2), related to the presence of less permeable silty layers. This is consistent with the
 2182 ratio estimated at the pore scale in Rothbach sandstone (~5) (Louis et al., 2005), attributed to lamination due
 2183 to differences both in the characteristics of the solid phase (grain size and packing) and in the content of the
 2184 Fe-ox.

2185 In this study we used the semivariogram range of spatial correlation of porosity as a parameter to
 2186 determine the REV from CT data (in addition to the classic method suggested by Bear, 2013). The spatial
 2187 correlation of porosity relates to a distance that fluid travels without being constrained by grains, and therefore
 2188 to permeability. Calibrating the range of correlation of porosity by modelling the semivariogram for different
 2189 sub-volume sizes sheds light on the specimen heterogeneity at the different scales. This approach could be
 2190 applied for a series of CT datasets, to determine the REV from the range of correlations and to compare to the
 2191 REV of permeability. Quantifying the spatial variability of structures which occur at different sub-volume,

Deleted: to

Deleted: e

Deleted: Fig.

Deleted:

Deleted: ides

Deleted: 1988

Deleted: s

199 sizes, may link to generation of preferential flow paths and to determination of effective porosity (associated
200 with mobile water fraction) that is available for transport.

Deleted: be found to

Deleted: influences on

Deleted: the

2202 6. Conclusions

2203 This paper presents a detailed description and evaluation of a multi-methodological petrophysical approach
2204 for the comprehensive multiscale characterization of reservoir sandstones. The validation was performed on
2205 samples from three different consecutive layers of Lower Cretaceous sandstone in northern Israel. The
2206 following conclusions can be drawn:

2207 1. The suggested methodology enables the identification of links between Darcy-scale permeability
2208 and an extensive set of geometrical, textural and topological rock descriptors, which are
2209 quantified at the pore scale by deterministic and statistical methods. Specifically, micro-scale
2210 geometrical rock descriptors (grain and pore size distributions, pore throat size, characteristic
2211 length, pore throat length of maximal conductance, specific surface area, and connectivity index)
2212 and macro-scale petrophysical properties (porosity and tortuosity), along with quantified
2213 anisotropy and inhomogeneity, are used to predict the permeability of the studied layers.

2214 2. Laboratory porosity and permeability measurements conducted on centimetre-scale samples
2215 show less variability for the quartz arenite (top and bottom) layers and more variability for the
2216 quartz wacke (intermediate) layer. The magnitudes of this variability in the samples are correlated
2217 with the dimensions of their representative volumes and anisotropy, both of which are evaluated
2218 within the micro-CT-imaged 3D pore geometry. This variability is associated with clay and
2219 cementation patterns in the layers and is quantified in this study with image and semivariogram
2220 analyses.

2221 3. Two different correlation lengths of porosity variations are revealed in the top quartz arenite layer
2222 by statistical semivariogram analysis: fluctuations at $\sim 100\ \mu\text{m}$ are due to variability in grain and
2223 pore sizes, and those at $\sim 1.6\ \text{mm}$ are due to the occurrence of high- and low-porosity horizontal
2224 bands occluded by Fe-ox cementation. The latter millimetre-scale variability is found to control
2225 the macroscopic rock permeability measured in the laboratory. Bands of lower porosity could be

Deleted: analysis

Deleted: For one

Deleted: quartz arenite sample (the top layer),

Deleted: T

Deleted: t

Deleted: different scales

Deleted: variogram

Deleted: 150

Deleted: 2

generated by Fe-ox cementation in regions with higher surface areas adjacent to preferential fluid flow paths.

4. More heterogeneous pore structures were revealed in the quartz wacke sandstone of the intermediate layer. This heterogeneity resulted from a combination of several spatial structures, each one with an internal irregularity; the pore size at the scale of ~50 µm, the distance between the pores at the scale of ~350 µm, and the larger-scale more porous “lense” structures originated at the presence of patchy clay deposition at the ~1-2 mm distance.

5. Quartz arenite sandstone of the bottom layer shows stationarity in the investigated domain and lower anisotropy characteristics than that of the top layer, due to less horizontal cement bands. Modelling of the experimental semivariograms indicates a scale of ~0.1 mm in all directions, associated with the average size of pore cross-section.

6. The macroscopic permeability upscaled from the pore-scale velocity field simulated by flow modelling in the micro-CT-scanned geometry of millimetre-scale sample shows agreement with laboratory petrophysical estimates obtained for centimetre-scale samples for the quartz arenite layers. The anisotropy in both estimates correlates with the presence of millimetre-scale bedding, also recognized by the semivariogram analysis.

7. The multi-methodological petrophysical approach detailed and evaluated in this study is particularly applicable for the detection of anisotropy at various rock scales and for the identification of its origin. Moreover, this method allows the accurate petrophysical characterization of reservoir sandstones with broad ranges of textural and topological features.

Acknowledgements

This project was supported by fellowships from the Ministry of Energy, Israel, and the University of Haifa. The authors are grateful to Igor Bogdanov from the University of Pau for his continuing scientific support. Special thanks to Rudy Swennen and his group from KU Leuven for their contributions to the MIP, thin section preparation, microscopy and micro-CT image processing; to Veerle Cnudde and her group from Ghent University for teaching us the image processing techniques; to Kirill Gerke and Timofey Sizonenko from the Russian Academy of Sciences for providing their image processing code; to Uzi Saltzman from Engineering Geology and Rock Mechanics Company, Israel, for sending his detailed historic geological

Moved (insertion) [1]

Deleted:

Deleted: For wacke sandstone sample a

Deleted: m

Deleted: nature

Deleted: than of the quartz sandstone were found

Deleted: e

Deleted: is

Deleted: few

Deleted: structure

Deleted: 0

Deleted: clay patches or

Deleted: s

Deleted: u

Moved up [1]: e-ox cementation in regions with higher surface areas adjacent to preferential fluid flow paths.

Deleted: of

Deleted: that

Deleted: in that sample

Deleted: <#>¶

Deleted: <#>(top)

Deleted: <#>-variogram

Deleted: paper

2289 description of the study area; and to Or Bialik, Nimer Taha and Ovie Emmanuel Eruteya from the
2290 University of Haifa, Israel, for their assistance in the laboratory work.

2291

2292 **Competing interests**

2293 The authors declare that they have no conflicts of interest.

2294

2295 **Author contributions**

2296 PH and RK designed the study. PH developed codes for pore-scale modelling with contributions by RK and
2297 MH. BS advised the microscopy and led the geological interpretations. MH scanned the samples and
2298 contributed to the statistical analysis conducted by PH. NW led the laboratory measurements. All co-authors
2299 participated in the analysis of the results. PH wrote the text with contributions from all co-authors. All co-
2300 authors contributed to the discussion and approved the paper.

2301

2302 **Supplementary Material & Data Availability**

2303 3-D μ -CT datasets are freely available at the open access data repository “PANGAEA” under the given doi:
2304 <https://doi.pangaea.de/10.1594/PANGAEA.907552>.

2305

Deleted: .

2307 **References**

2308 Abed, A. M.: Depositional environments of the early cretaceous Kurnub (Hatira) sandstones, North Jordan,
2309 Sedimentary Geology, 31(3-4), 267-279, **1982**.

2310 Akinlotan, O.: Porosity and permeability of the English (Lower Cretaceous) sandstones, Proceedings of the
2311 Geologists' Association, 127, 681-690, **2016**.

2312 Akinlotan, O.: Mineralogy and palaeoenvironments: the Weald Basin (Early Cretaceous), Southeast England,
2313 The Depositional Record, 3(2), 187-200, **2017**.

2314 Akinlotan, O.: Multi-proxy approach to palaeoenvironmental modelling: the English Lower Cretaceous Weald
2315 Basin, *Geol. J.* **53**, 316–335, **2018**.

2316 Ambegaokar, V., Halperin, B. I., & Langer, J. S. (1971). Hopping conductivity in disordered systems. *Physical*
2317 *review B*, **4**(8), 2612.

2318 American Petroleum Institute, API : Recommended Practices for Core Analysis, RP 40, second edition, **1998**.

2319 Amireh, B. S.: Sedimentology and palaeogeography of the regressive-transgressive Kurnub Group (Early
2320 Cretaceous) of Jordan, Sedimentary Geology, 112(1-2), 69-88., **1997**.

2321 Andrä, H., Combaret, N., Dvorkin, J., Glatt, E., Han, J., Kabel, M., Keehm, Y., Krzikalla, F., Lee, M.,
2322 Madonna, C., Marsh, M., Mukerji, T., Saenger, E., Sain, R., Saxena, N., Ricker, S., Wiegmann, A., and
2323 Zhan, X.: Digital rock physics benchmarks-Part I: Imaging and segmentation, *Computers & Geosciences*,
2324 **50**, 25-32, **2013a**.

2325 Andrä, H., Combaret, N., Dvorkin, J., Glatt, E., Han, J., Kabel, M., Keehm, Y., Krzikalla, F., Lee, M.,
2326 Madonna, C., Marsh, M., Mukerji, T., Saenger, E., Sain, R., Saxena, N., Ricker, S., Wiegmann, A., and
2327 Zhan, X.: Digital rock physics benchmarks-Part II: Computing effective properties, *Computers &*
2328 *Geosciences*, **50**, 33-43, **2013b**.

2329 Arns, J.Y., Sheppard, A.P., Arns, C.H., Knackstedt, M.A., Yelkhovsky, A., and Pinczewski, W.V.: Pore-level
2330 validation of representative pore networks obtained from micro-CT images. In: *Proceedings of the annual*
2331 *symposium of the society of core analysis, SCA2007-A26, Calgary, Canada, 2007*.

2332 Asakawa, S., Watanabe, T., Lyu, H., Funakawa, S. and Toyohara, H.: Mineralogical composition of tidal flat
2333 sediments in Japan, *Soil Science and Plant Nutrition*, 1-9, **2020**.

2334 Avigad, D., Kolodner, K., McWilliams, M., Persing, H., and Weissbrod, T.: Origin of northern Gondwana
2335 Cambrian sandstone revealed by detrital zircon SHRIMP dating, *Geology*, 31(3), 227-230, **2003**.

2336 Avigad, D., Sandler, A., Kolodner, K., Stern, R. J., McWilliams, M., Miller, N., and Beyth, M.: Mass-
2337 production of Cambro-Ordovician quartz-rich sandstone as a consequence of chemical weathering of Pan-
2338 African terranes: Environmental implications, *Earth and Planetary Science Letters*, 240(3-4), 818-826,
2339 **2005**.

2340 Bear, J.: *Dynamics of fluids in porous media*. Courier Corporation, Courier Corporation, **2013**.

2341 Blunt, M. J., Bijeljic, B., Dong, H., Gharbi, O., Iglauer, S., Mostaghimi, P., Paluszny, A., and Pentland, C.:
2342 Pore-scale imaging and modelling, *Advances in Water Resources*, 51, 197-216, **2013**.

2343 Boek, E. S., and Venturoli, M.: Lattice-Boltzmann studies of fluid flow in porous media with realistic rock
2344 geometries, *Computers & Mathematics with Applications*, 59(7), 2305-2314, **2010**.

Deleted: Adams, A. E., MacKenzie, W. S., and Guilford, C.: Atlas of sedimentary rocks under the microscope. Routledge, Taylor and Francis Group, London and New York, **2017**.

Moved (insertion) [6]

Moved up [6]: American Petroleum Institute, API : Recommended Practices for Core Analysis, RP 40, second edition, **1998**.

Deleted:

Deleted: Bachmann, M., and Hirsch, F.: Lower Cretaceous carbonate platform of the eastern Levant (Galilee and the Golan Heights): stratigraphy and second-order sea-level change, *Cretaceous Research*, 27(4), 487-512, **2006**.

Deleted:

Deleted: Bear, J., Dynamics of Fluids in Porous Media. Courier Corporation, **1988**.

2359 Bogdanov, I. I., Guerton, F., Kpahou, J., and Kamp, A. M.: Direct pore-scale modeling of two-phase flow
 2360 through natural media, in: Proceedings of the 2011 COMSOL Conference in Stuttgart, **2011**.

2361 Bogdanov, I. I., Kpahou, J., and Guerton, F.: Pore-scale single and two-phase transport in real porous medium,
 2362 in: Proceedings of ECMOR XIII-13th European Conference on the Mathematics of Oil Recovery,
 2363 September, **2012**.

2364 Boudreau, B. P.: The diffusive tortuosity of fine-grained unlithified sediments, *Geochimica et Cosmochimica*
 2365 *Acta*, 60(16), 3139-3142, **1996**.

2366 Brabant, L., Vlassenbroeck, J., De Witte, Y., Cnudde, V., Boone, M. N., Dewanckele, J., and Van Hoorebeke,
 2367 L.: Three-dimensional analysis of high-resolution X-ray computed tomography data with Morpho+,
 2368 *Microscopy and Microanalysis*, 17(2), 252-263, **2011**.

2369 Brunke, O., Brockdorf, K., Drews, S., Müller, B., Donath, T., Herzen, J., and Beckmann, F.: Comparison
 2370 between X-ray tube based and synchrotron radiation based μ CT, in: *Developments in X-ray Tomography*
 2371 VI, edited by: Stock, S. R., San Diego: SPIE, 7078, **2008**.

2372 Calvo, R., The diagenetic history of Heletz Formation and the timing of hydrocarbons accumulation in Heletz-
 2373 Kokhav oil field. M.Sc. thesis, The Hebrew University of Jerusalem, 72 p. (in Hebrew, with English
 2374 abstract), 1992.

2375 Calvo, R., Ayalon, A., Bein, A., and Sass, E.: Chemical and isotopic composition of diagenetic carbonate
 2376 cements and its relation to hydrocarbon accumulation in the Heletz-Kokhav oil field (Israel), *Journal of*
 2377 *Geochemical Exploration*, 108(1), 88-98, **2011**.

2378 Carman, P. C.: Fluid flow through granular beds, *Trans. Inst. Chem. Eng.*, 15, 150-166, **1937**.

2379 Cerepi, A., Durand, C., and Brosse, E.: Pore microgeometry analysis in low-resistivity sandstone reservoirs,
 2380 *Journal of Petroleum Science and Engineering*, 35(3-4), 205-232, **2002**.

2381 Clavaud, J. B., Mainault, A., Zamora, M., Rasolofosaon, P., and Schlitter, C.: Permeability anisotropy and its
 2382 relations with porous medium structure, *Journal of Geophysical Research: Solid Earth*, 113(B1), **2008**.

2383 Cnudde, V., and Boone, M. N.: High-resolution X-ray computed tomography in geosciences: A review of the
 2384 current technology and applications, *Earth-Science Reviews*, 123, 1-17, **2013**.

2385 Cohen, A., and Boehm, S.: Lithofacies and environments of deposition of the Lower Cretaceous Helez &
 2386 Telamim Formations, Geological Survey of Israel Report No. 5, **1983**.

2387 Cohen, Z.: The geology of the Lower Cretaceous in Southern Coastal Plain, Ph.D. thesis, The Hebrew
 2388 University of Jerusalem, 98 pp. (in Hebrew, with English abstract), **1971**.

2389 Cressie, N.: Fitting variogram models by weighted least squares. *Journal of the international Association for*
 2390 *mathematical Geology*, 17(5), 563-586, 1985.

2391 Du, S., Pang, S., and Shi, Y.: Quantitative characterization on the microscopic pore heterogeneity of tight oil
 2392 sandstone reservoir by considering both the resolution and representativeness, *J. Pet. Sci. Eng.*, 169, 388-
 2393 392, 2018.

2394 Dullien, F. A.: Porous media: fluid transport and pore structure, Academic press, **2012**.

2395 Harter, T.: Finite-size scaling analysis of percolation in three-dimensional correlated binary Markov chain
 2396 random fields, *Physical Review E*, 72(2), 026120, **2005**.

Deleted: Borgomano, J., Masse, J. P., Fenerci-Masse, M., and Fournier, F.: Petrophysics of Lower Cretaceous platform carbonate outcrops in Provence (SE France): implications for carbonate reservoir characterisation, *Journal of Petroleum Geology*, 36(1), 5-41, **2013**.¶

Deleted: Calvo, R., Ayalon, A., Bein, A., and Sass, E.: The diagenesis history of Heletz formation and the timing of hydrocarbon accumulation in Heletz-Kokhav oil field, *Geological Survey of Israel, Current Research*, 8, 82-83, **1993**.¶

Deleted: Cressie, N.: Statistics for spatial data, *Terra Nova*, 4(5), 613-617, **1992**.¶
 Djebbar, T., and Donaldson, E. C.: Petrophysics. Elsevier Engineering Information Incorporated, **2004**.¶

Farrel, N.J.C., Healy, D., and Taylor, C.W.: Anisotropy of permeability in faulted porous sandstones. *Journal of Structural Geology* 63, 50-67, **2014**.

Ferreira, N. N., Ferreira, E. P., Ramos, R. R., and Carvalho, I. S.: Palynological and sedimentary analysis of the Igarapé Ipiranga and Querru 1 outcrops of the Itapecuru Formation (Lower Cretaceous, Parnaíba Basin), Brazil, *Journal of South American Earth Sciences*, 66, 15-31, **2016**.

Folk, R. L., and Ward, W. C.: Brazos River bar [Texas]; a study in the significance of grain size parameters, *Journal of Sedimentary Research*, 27(1), 3-26, **1957**.

Gardosh, M. A., and Tannenbaum, E.: The petroleum systems of Israel, in: *Petroleum systems of the Tethyan region*: AAPG Memoir, edited by: Marlow, L., Kendall, C., and Yose, L., 106, 179-216, **2014**.

Garfunkel, Z.: The pre-quaternary geology in Israel, in: *The zoogeography of Israel*, edited by: Tchernov, E., and Yom-Tov, Y., Dr W. Junk Publishers, Dordrecht, Netherlands, 7-34, **1988**.

Garfunkel, Z.: History and paleogeography during the Pan-African orogen to stable platform transition: reappraisal of the evidence from the Elat area and the northern Arabian-Nubian Shield, *Israel Journal of Earth Sciences*, 48, 135-157, **1999**.

Giesche, H.: Mercury porosimetry: a general (practical) overview. *Particle & particle systems characterization*, 23(1), 9-19, **2006**.

Grader, P., and Reiss, Z.: On the Lower Cretaceous of the Heletz area, *Geological Survey of Israel, Bull No.* 16, 14 pp., **1958**.

Grader, P.: The geology of the Heletz oil field, Ph.D. thesis, The Hebrew University of Jerusalem, 81 pp. (in Hebrew, with English abstract), **1959**.

Gringarten, E., and Deutsch, C.V.: Teacher's aide [semivariogram](#) interpretation and modeling. *Mathematical Geology*, 33(4), 507-534, **2001**.

Guibert, R., Horgue, P., Debenest, G., and Quintard, M.: A comparison of various methods for the numerical evaluation of porous media permeability tensors from pore-scale geometry, *Mathematical Geosciences*, 48(3), 329-347, **2016**.

Haldorsen, H. H., and Lake, L. W.: A new approach to shale management in field-scale models, *Society of Petroleum Engineers Journal*, 24(04), 447-457, **1984**.

Halisch, M.: Application and assessment of the lattice boltzmann method for fluid flow modeling in porous rocks, PhD thesis, Technical University of Berlin, 182 pp., **2013a**.

Halisch, M.: The REV Challenge – estimating representative elementary volumes and porous rock inhomogeneity from high resolution micro-CT data sets, *Society of Core Analysts (SCA) Proceedings*, SCA2013-069, **2013b**.

Halisch, M., Weller, A., Debschütz, W., Sattler, C. D., and El-Sayed, A. M.: A complex core-log case study of an anisotropic sandstone, originating from Bahariya Formation, Abu Gharadig Basin, Egypt, *Petrophysics*, 50(06), **2009**.

Deleted: Foos, A. M., Regional hydrogeology of the Sharon Aquifer, in: *Pennsylvanian sharon formation, past and present: sedimentology, hydrology, historical and environmental significance*, edited by: Foos, A. M., Guidebook No. 18, Ohio Department of Natural Resources, Division of Geology, Columbus OH, Chapter 4, 19-25, **2003**.

Deleted: Giesche, H. (2006). Mercury porosimetry: a general (practical) overview. *Particle & particle systems characterization*, 23(1), 9-19.

Deleted: variogram

Deleted:

Deleted:

Haoguang, W. E. I., Kun, M. A., Xiang'an, Y. U. E., and Xinxin, W. A. N. G.: The Relationship of Ultra-Low Permeability Sandstone Aspect Ratio With Porosity, Permeability, *Advances in Petroleum Exploration and Development*, 7(1), 7-12, **2014**.

Harding, T. G., Norris, B., and Smith, K.H.: Horizontal Water Disposal Well Performance in a High Porosity and Permeability Reservoir Conference: SPE International Thermal Operations and Heavy Oil Symposium and International Horizontal Well Technology Conference. SPE-18153-MS, <https://doi.org/10.2118/79007-MS>, 2002.

Hurst, A., and Nadeau, P. H.: Clay microporosity in reservoir sandstones: an application of quantitative electron microscopy in petrophysical evaluation, *AAPG bulletin*, 79(4), 563-573, **1995**.

Iassonov, P., Gebrenegus, T., and Tuller, M.: Segmentation of X-ray computed tomography images of porous materials: A crucial step for characterization and quantitative analysis of pore structures, *Water Resources Research*, 45(9), **2009**.

Jackson, M. D., Muggeridge, A. H., Yoshida, S., and Johnson, H. D.: Upscaling permeability measurements within complex heterolithic tidal sandstones, *Mathematical Geology*, 35(5), 499-520, **2003**.

Kalaydjian, F.: Origin and quantification of coupling between relative permeabilities for two-phase flows in porous media, *Transport in porous media*, 5(3), 215-229, **1990**.

Kass, M., Witkin, A., and Terzopoulos, D.: Snakes: Active contour models, *International Journal of Computer Vision*, 1(4), 321-331, **1988**.

Katz, A. J., and Thompson, A. H.: Prediction of rock electrical conductivity from mercury injection measurements, *Journal of Geophysical Research: Solid Earth*, 92(B1), 599-607, 1987.

Kerckhofs, G., Schrooten, J., Van Cleynebreugel, T., Lomov, S. V., and Wevers, M.: Validation of x-ray micro-focus computed tomography as an imaging tool for porous structures, *Review of Scientific Instruments*, 79(1), 013711, **2008**.

Khan, F., Enzmann, F., and Kersten, M.: Multi-phase classification by a least-squares support vector machine approach in tomography images of geological samples, *Solid Earth*, 7(2), 481-492, **2016**.

Knackstedt, M., Jaime, P., Butcher, A.R., Botha, P.W.S.K., Middleton, J., and Sok, R.: Integrating reservoir characterization: 3D dynamic, petrophysical and geological description of reservoir facies. In: *Proceedings of the SPE Asia Pacific oil and gas conference and exhibition*, 18–20 October, 2010, Brisbane, Queensland, Australia, SPE 133981, **2010**.

Kolodner, K., Avigad, D., Ireland, T. R., and Garfunkel, Z.: Origin of Lower Cretaceous ('Nubian') sandstones of North-east Africa and Arabia from detrital zircon U-Pb SHRIMP dating, *Sedimentology*, 56(7), 2010-2023, 2009.

Kozeny, J.: *Über kapillare leitung der wasser in boden*, Royal Academy of Science, Vienna, *Proceedings Class I*, 136, 271-306, **1927**.

Krinsley, D. H., Pye, K., Boggs Jr, S., and Tovey, N. K.: *Backscattered scanning electron microscopy and image analysis of sediments and sedimentary rocks*. Cambridge University Press, **2005**.

Lenormand, R.: Sca2003-52: Interpretation of mercury injection curves to derive pore size distribution, in: *Proceedings of 2003 International Symposium of SCA.*, **2003**.

Legland, D., Arganda-Carreras, I., Andrey, P.: MorphoLibJ: integrated library and plugins for mathematical morphology with ImageJ. *Bioinformatics*, 32(22), 3532-3534, 2016.

Deleted: Hubert, J. F.: A zircon-tourmaline-rutile maturity index and the interdependence of the composition of heavy mineral assemblages with the gross composition and texture of sandstones, *Journal of Sedimentary Research*, 32(3), 440-450, **1962**.¶

Deleted: Katz, A. J., and Thompson, A. H.: Quantitative prediction of permeability in porous rock, *Physical Review B*, 34(11), 8179, **1986**.¶

Deleted: ¶

Li, Y., He, D., Chen, L., Mei, Q., Li, C., and Zhang, L.: Cretaceous sedimentary basins in Sichuan, SW China: Restoration of tectonic and depositional environments, *Cretaceous Research*, 57, 50-65, **2016**.

Linden, S., Wiegmann, A., and Hagen, H.: *The LIR space partitioning system applied to the Stokes equations*, *Graph. Models* 82, 58–66 (2015).

Linden S., Cheng L., Wiegmann A.: *Specialized methods for direct numerical simulations in porous media*, Math2Market GmbH, technical report, <https://doi.org/10.30423/report.m2m-2018-01>, **2018**.

Liu, X., Wang, J., Ge, L., Hu, F., Li, C., Li, X., Yu, J., Xu, H., Lu, S., and Xue, Q.: *Porescale characterization of tight sandstone in Yanchang Formation Ordos Basin China using micro-CT and SEM imaging from nm- to cm-scale*, *Fuel*, 209, 254–264, **2017**.

Lewis, J.J.M.: *Outcrop-derived quantitative models of permeability heterogeneity for genetically different sand bodies*. In: *SPE Annual Technical Conference and Exhibition*, 2-5 October 1988, Houston, Texas, **1988**.

Louis, L., David, C., Metz, V., Robion, P., Menendez, B., and Kissel, C.: Microstructural control on the anisotropy of elastic and transport properties in undeformed sandstones. *International journal of rock mechanics and mining sciences*, 42(7-8), 911-923, **2005**.

Massaad, M.: Origin and environment of deposition of Lebanon basal sandstones, *Eclogae Geologicae Helvetiae*, 69(8), **1976**.

Mckay, G., *Use of Adsorbents for the Removal of Pollutants from Wastewater*. CRC press, **1995**.

MacKenzie, W. S., Adams, A. E., & Brodie, K. H. *Rocks and Minerals in Thin Section: A Colour Atlas*. CRC Press., **2017**.

Meyer, R., and Krause, F. F.: A comparison of plug-derived and probe-derived permeability in cross-bedded sandstones of the Virgelle Member, Alberta, Canada: The influence of flow directions on probe permeametry, *AAPG bulletin*, 85(3), 477-489, **2001**.

Meyer, R.: *Anisotropy of Sandstone Permeability*. CREWES Research Report, Vol. 14, **2002**.

Mostaghimi, P., Blunt, M. J., and Bijeljic, B.: Computations of absolute permeability on micro-CT images, *Mathematical Geosciences*, 45(1), 103-125, **2013**.

Moussavi-Harami, R., and Brenner, R. L.: *Diagenesis of non-marine petroleum reservoirs: the Neocomian (Lower Cretaceous) Shurijeh Formation, Kopet-Dagh basin, NE Iran*. *Journal of Petroleum Geology*, 16(1), 55-72, **1993**.

Munawar, M.J., Lin, C., Cnudde, V., Bultreys, T., Dong, C., Zhang, X., De Boever, W., Zahid, M.A., and Wu, Y.: *Petrographic characterization to build an accurate rock model using micro-CT: case study on low-permeable to tight turbidite sandstone from Eocene Shahejie Formation*, *Micron* 109, 22–33, **2018**.

Narsilio, G. A., Buzzi, O., Fityus, S., Yun, T. S., and Smith, D. W.: Upscaling of Navier-Stokes equations in porous media: Theoretical, numerical and experimental approach, *Computers and Geotechnics*, 36(7), 1200-1206, **2009**.

Nelson, P. H.: Pore-throat sizes in sandstones, tight sandstones, and shales, *AAPG bulletin*, 93(3), 329-340, **2009**.

Neuzil, C. E.: Permeability of Clays and Shales, *Annual Review of Earth and Planetary Sciences*, 47, 247-273, **2019**.

Deleted: 2018,

Deleted: ¶

Deleted: ¶

Deleted: ¶

Deleted: ¶

2550 Nordahl, K., and Ringrose, P. S.: Identifying the representative elementary volume for permeability in
 2551 heterolithic deposits using numerical rock models, *Mathematical Geosciences*, 40(7), 753, **2008**.
 2552 Nordahl, K., Ringrose, P. S., and Wen, R.: Petrophysical characterisation of a heterolithic tidal reservoir
 2553 interval using a process-based modelling tool, *Petroleum Geoscience*, 11, 17-28, **2005**.
 2554 Norris, R. J., and J. J. M. Lewis. The geological modeling of effective permeability in complex heterolithic
 2555 facies, in SPE Annual Technical Conference and Exhibition, Society of Petroleum Engineers, **1991**.
 2556 Okabe, H., and Oseto, K.: Pore-scale heterogeneity assessed by the lattice-Boltzmann method, *Society of Core*
 2557 *Analysts (SCA2006-44)*, 12-16, **2006**.
 2558 Ovaysi, S., and Piri, M.: Direct pore-level modeling of incompressible fluid flow in porous media, *Journal of*
 2559 *Computational Physics*, 229(19), 7456-7476, **2010**.
 2560 Pettijohn, F. J., Potter, P. E., and Siever, R.: *Sand and Sandstone*. Springer Verlag, **2nd ed.**, New York, **1987**.
 2561 Ploner, A.: The use of the variogram cloud in geostatistical modelling. *Environmetrics: The official journal of*
 2562 *the International Environmetrics Society*, 10(4), 413-437, **1999**.
 2563 Pyrcz, M. J., and Deutsch, C. V.: The whole story on the hole effect. *Geostatistical Association of Australasia*,
 2564 *Newsletter*, 18, 3-5, **2003**.
 2565 Renard, P., Genty, A., and Stauffer, F.: Laboratory determination of the full permeability tensor, *Journal of*
 2566 *Geophysical Research: Solid Earth*, 106(B11), 26443-26452, **2001**.
 2567 Reynolds, A. D.: *Paralic reservoirs*. Geological Society, London, Special Publications, 444(1), 7-34, **2017**.
 2568 Ringrose, P., and Bentley, M.: *Reservoir Model Design: A Practitioner's Guide*, Springer, 249 p. New York,
 2569 **2015**.
 2570 Rootare, H. M., and Prenzlow, C. F.: Surface areas from mercury porosimeter measurements, *The Journal of*
 2571 *physical chemistry*, 71(8), 2733-2736, **1967**.
 2572 RP40, A. P. I. (1960). *API recommended practice for core-analysis procedure. Edition, API, New York, 12-13*.
 2573 Rustad, A. B., Theting, T. G., and Held, R. J.: Pore space estimation, upscaling and uncertainty modelling for
 2574 multiphase properties. In SPE Symposium on Improved Oil Recovery, Society of Petroleum Engineers,
 2575 **2008**.
 2576 Saltzman, U.: Survey of the southeastern flanks of Mount Hermon, Tahal report (in Hebrew), **1968**.
 2577 Sato, M., Panaghi, K., Takada, N., and Takeda, M.: Effect of Bedding Planes on the Permeability and
 2578 Diffusivity Anisotropies of Berea Sandstone, *Transport in Porous Media*, 127(3), 587-603, **2019**.
 2579 Schindelin, J., Arganda-Carreras, I., Frise, E., Kaynig, V., Longair, M., Pietzsch, T., Preibisch, S., Rueden,
 2580 C., Saalfeld, S., Schmid, B., Tinevez, J., White, D., Hartenstein, V., Eliceiri, K., Tomancak, P., and
 2581 Cardona, A.: Fiji: an open-source platform for biological-image analysis, *Nature methods*, 9(7), 676, **2012**.
 2582 Schlüter, S., Sheppard, A., Brown, K., and Wildenschild, D.: Image processing of multiphase images obtained
 2583 via X-ray microtomography: a review, *Water Resources Research*, 50(4), 3615-3639, **2014**.
 2584 Schmitt, M., Halisch, M., Müller, C., and Fernandes, C. P.: Classification and quantification of pore shapes in
 2585 sandstone reservoir rocks with 3-D X-ray micro-computed tomography, *Solid Earth*, 7(1), 285-300, **2016**.

Deleted: Niemi, A., Bensabat, J., Shtivelman, V., Edlmann, K.,
 Gouze, P., Luquot, L., Shtivelman, V., Edlmann, K., Liang, T.,
 Fagerlund, F., Gendler, M., Goldberg, I., Tatomir, A., Lange, T.,
 Sauter, M., and Freifeld, B.: Heletz experimental site overview,
 characterization and data analysis for CO₂ injection and geological
 storage, *International Journal of Greenhouse Gas Control*, 48, 3-23,
2016.¶

Deleted: Oyanyan, R. O., and Ideozu, R. U.: Sedimentological
 Control on Permeability Anisotropy and Heterogeneity in Shorefae
 Reservoir, Niger Delta, Nigeria, *International Journal of Science
 and Technology*, 6(1), **2016**.¶
 Peksa, A. E., Wolf, K. H. A., and Zitha, P. L.: Bentheimer
 sandstone revisited for experimental purposes, *Marine and
 Petroleum Geology*, 67, 701-719, **2015**.¶

Deleted: 1972

Deleted: ¶

Deleted: Or 19671968

2603 Scholz, C., Wirner, F., Götz, J., Rüde, U., Schröder-Turk, G. E., Mecke, K., and Bechinger, C.: Permeability
 2604 of porous materials determined from the Euler characteristic, Physical review letters, 109(26), 264504,
 2605 **2012**.

2606 Sethian, J. A.: A fast marching level set method for monotonically advancing fronts, Proceedings of the
 2607 National Academy of Sciences, 93(4), 1591-1595, **1996**.

2608 Shaw, S. M.: Southern Palestine geological map on a Scale 1:250,000 with explanatory notes, Palestine Geol.
 2609 Soc. Publ., Jerusalem, **1947**.

2610 Shenhav, H.: Lower Cretaceous sandstone reservoirs, Israel: petrography, porosity, permeability, AAPG
 2611 Bulletin, 55(12), 2194-2224, **1971**.

2612 Sheppard, A. P., Sok, R. M., and Averdunk, H.: Techniques for image enhancement and segmentation of
 2613 tomographic images of porous materials, Physica A: Statistical mechanics and its applications, 339(1-2),
 2614 145-151, **2004**.

2615 Shimron, A. E.: Tectonic evolution of the southern Mount Hermon, Geological Survey of Israel Report,
 2616 GSI/10/98, **1998**.

2617 Sneh, A., and Weinberger, R.: Geology of the Metula quadrangle, northern Israel: Implications for the offset
 2618 along the Dead Sea Rift, Israel Journal of Earth Sciences, 52, **2003**.

2619 Sneh, A., and Weinberger, R.: Metula sheet 2-11, Geology Survey of Israel, Ministry of Energy, **2014**.

2620 Tatomir, A. B., Halisch, M., Duschl, F., Peche, A., Wiegand, B., Schaffer, M., Licha, T., Niemi, A., Bensabat,
 2621 J., and Sauter, M.: An integrated core-based analysis for the characterization of flow, transport and
 2622 mineralogical parameters of the Heletz pilot CO₂ storage site reservoir, International Journal of
 2623 Greenhouse Gas Control, 48, 24-43, **2016**.

2624 Stephens, D. B., Hsu, K. C., Prieksat, M. A., Ankeny, M. D., Blandford, N., Roth, T., Kelsey, J., Whitworth, J.
 2625 R.: A comparison of estimated and calculated effective porosity. Hydrogeology Journal, 6(1), 156-165,
 2626 **1998**.

2627 Tiab, D., and Donaldson, E. C.: Petrophysics: Theory and Practice of Measuring Reservoir Rock and Fluid
 2628 Transport Properties, Elsevier, **2004**.

2629 Tidwell, V. C., and Wilson, J. L.: Permeability upscaling measured on a block of Berea Sandstone: Results
 2630 and interpretation, Mathematical Geology, 31(7), 749-769, **1999**.

2631 Vincent, L., and Soille, P.: Watersheds in digital spaces: an efficient algorithm based on immersion
 2632 simulations, IEEE Transactions on Pattern Analysis & Machine Intelligence, 6, 583-598, **1991**.

2633 Vogel, H. J.: Topological characterization of porous media, in: Morphology of condensed matter, edited by:
 2634 Mecke, K. R., and Stoyan, D., Springer, Berlin, 75-92, **2002**.

2635 Schwanghart, W.: Experimental (Semi-
 2636 Variogram ([https://www.mathworks.com/matlabcentral/fileexchange/20355-experimental-semi-](https://www.mathworks.com/matlabcentral/fileexchange/20355-experimental-semi-variogram)
 2637 [variogram](https://www.mathworks.com/matlabcentral/fileexchange/20355-experimental-semi-variogram)), MATLAB Central File Exchange, **2020a**,
 2638 Schwanghart, W. . variogramfit ([https://www.mathworks.com/matlabcentral/fileexchange/25948-](https://www.mathworks.com/matlabcentral/fileexchange/25948-variogramfit)
 2639 [variogramfit](https://www.mathworks.com/matlabcentral/fileexchange/25948-variogramfit)), MATLAB Central File Exchange, **2020b**.

Deleted: Shimron, A. E. and Peltz, S.: Early Cretaceous
 pyroclastic volcanism on Mount Hermon Range, Geological Survey
 of Israel, Report GSI/10/98, **1993**.

2643 Wang, W. P., Liu, J. L., Zhang, J. B., Li, X. P., Cheng, Y. N., Xin, W. W., & Yan, Y. F. Evaluation of laser
2644 diffraction analysis of particle size distribution of typical soils in China and comparison with the Sieve-
2645 Pipette method. *Soil science*, 178(4), 194-204, **2013**.

2646 Viswanathan, J., Konwar, D., & Jagatheesan, K. Laboratory Characterization of Reservoir Rock and Fluids of
2647 Upper Assam Basin, India. In *Novel Issues on Unsaturated Soil Mechanics and Rock Engineering: Proceedings of the 2nd GeoMEast International Congress and Exhibition on Sustainable Civil*
2648 *Infrastructures, Egypt 2018–The Official International Congress of the Soil-Structure Interaction Group*
2649 *in Egypt (SSIGE)* (p. 179). Springer, **2018**.

2651 Weissbrod, T.: Stratigraphy and correlation of the Lower Cretaceous exposures across the Dead Sea Transform
2652 with emphasis on tracing the Amir Formation in Jordan, *Israel Journal of Earth Sciences*, 51(2), 55–78,
2653 **2002**.

2654 Weissbrod, T., and Nachmias, J.: Stratigraphic significance of heavy minerals in the late Precambrian-
2655 Mesozoic clastic sequence (“Nubian Sandstone”) in the Near East, *Sedimentary Geology*, 47(3-4), 263-
2656 291, **1986**.

2657 Whitaker, S.: Flow in porous media I: A theoretical derivation of Darcy's law, *Transport in porous media*, 1(1),
2658 3-25, **1986**.

2659 Wiegmann, A.: *GeoDict, the Digital Material Laboratory - Easy-to-use - Powerful - Accurate, Whitepaper*,
2660 **2019**, <https://doi.org/10.30423/WHITEPAPER.M2M-2019>

2661 Wildenschild, D., and Sheppard, A. P.: X-ray imaging and analysis techniques for quantifying pore-scale
2662 structure and processes in subsurface porous medium systems, *Advances in Water Resources*, 51, 217-
2663 246, **2013**.

2664 Zhang, D., Zhang, R., Chen, S., and Soll, W. E.: Pore scale study of flow in porous media: Scale dependency,
2665 REV, and statistical REV, *Geophysical research letters*, 27(8), 1195-1198, **2000**.

2666 Zhang, P., Leed, Y. L., and Zhange, J.: A review of high-resolution X-ray computed tomography applied to
2667 petroleum geology and a case study, *Micron*, 124, 102702, **2019**.

2668 Zhu, W., Montési, L. G. J., and Wong, T. F.: Effects of Stress on the Anisotropic Development of Permeability
2669 during Mechanical Compaction of Porous Sandstones, *Geological Society, London*, 119-136, *Special*
2670 *Publications*, 200, **2002**.

Moved down [3]: (2013).

Deleted: .

Moved (insertion) [3]

Deleted: (

Deleted:)

Moved down [4]: (2018, October).

Moved (insertion) [4]

Deleted: (

Deleted: , October)

Deleted: Wilson, M., Shimron, A. E., Rosenbaum, J. M., and Preston, J.: Early Cretaceous magmatism of Mount Hermon, Northern Israel, *Contributions to Mineralogy and Petrology*, 139(1), 54-67, **2000**.¶
Worden, R. H., and Burley, S. D.: Sandstone diagenesis: the evolution of sand to stone, *Sandstone Diagenesis: Recent and Ancient*, 4, 3-44, **2003**.¶

Appendix A: Results of the REV determination by the classical approach

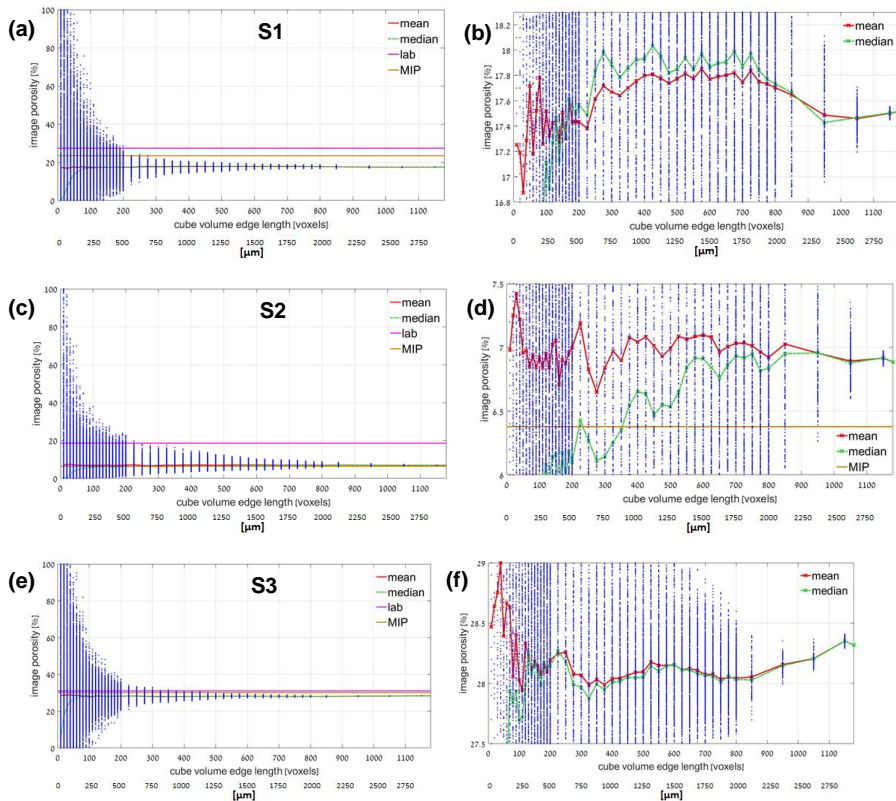


Figure A1: Results of the classic REV analysis for sandstones S1-S3 (a,c,e). (b, d, f) Magnified views of the mean and median porosity trends of S1-S3 calculated for varying edge lengths. The scattering of porosity measured for each sub-volume is shown in blue dots. The laboratory porosities measured by gas porosimetry are shown by a pink line. The image porosity for CT, which was predicted by MIP for the resolution limit, is shown by a yellow line. The mean and median porosity are depicted by red and green lines, respectively.

Deleted: Appendix A: Description of the Hatira Formation¶

The Hatira Fm. is the lower part of the Kurnub Group of Lower Cretaceous (Neocomian – Barremian) age. The Hatira Fm. nomenclature used in Israel and Jordan is equivalent to Grès de Base in Lebanon (Massaad, 1976). This formation occurs in Israel in outcrops from the Eilat area along the rift valley, in the central Negev, and in the northernmost outcrops on Mount Hermon; it forms part of a large Palaeozoic – Mesozoic platform and continental margin deposits in northeastern Africa and Arabia. The Hatira Fm. consists of siliciclastic units, typically dominated by quartz-rich sandstones (Kolodner et al., 2009 and references therein). The underlying Palaeozoic sandstones cover large areas in North Africa and Arabia from Morocco to Oman; these sandstones overlie a Precambrian basement affected by Neoproterozoic (pan African) orogenesis (Garfunkel, 1988, 1999; Avigad et al., 2003, 2005). The lower Palaeozoic sandstones in Israel and Jordan originated from the erosion of that Neoproterozoic basement, the Arabian-Nubian Shield, with contributions from older sources. These lower Palaeozoic sandstones (Cambrian and Ordovician) are described as first-cycle sediments (Weissbrod and Nachmias, 1986; Amireh, 1997; Avigad et al., 2005). Exposures of the Hatira Fm. in the Central Negev, the Arava Valley, Eilat and Sinai were originally defined as the Wadi (Kurnub) Hatira Sandstone (Shaw, 1947). The largely siliciclastic section of the Hatira Fm. is intercalated with carbonates and shales representing marine incursions that increase towards the north (Weissbrod, 2002).¶

The Lower Cretaceous sandstones of the Kurnub Group are described as super mature, cross-bedded, medium- to fine-grained, moderately sorted to well-sorted quartz arenites with a high zircon-tourmaline-rutil (ZTR) index (for more details, see Kolodner (2009)). Earlier observations indicate the relatively scarce occurrence of siltstones and claystones compared to sandstones (Massaad, 1976; Abed, 1982; Amireh, 1997). These Lower Cretaceous sandstones are mainly the recycled products of older siliciclastic rocks throughout the Phanerozoic; the sand was first eroded from the surface of the pan African orogeny ca. 400 Ma prior to its deposition in the Lower Cretaceous sediments (Kolodner et al., 2009).¶

The Mount Hermon block was located at the southern border of the Tethys Ocean during the Early Cretaceous (Bachman and Hirsch, 2006). A paleo-geographical reconstruction indicates that the sandy Hatira Fm. (Fig. 1) was deposited in a large basin, which included both terrestrial and coastal environments such as swamps and lagoons (Sneh and Weinberger, 2003). The Hermon block, located next to the Dead Sea Transform, was rapidly uplifted during the Neogene (Shimron, 1998). The area is marked by intense erosion, which resulted in extensive outcrops such as those near Ein Kinya on the southeastern side of Wadi E' Shatr.¶

Deleted: B

Deleted: B1

Deleted: .

Appendix B: Maximum hydraulic conductance

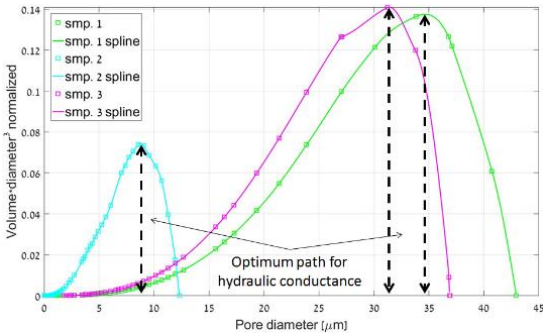


Figure B1: The pore throat length of the maximal hydraulic conductance, l_{max} , is defined from the maximal (normalized) hydraulic conductance (Katz and Thompson, 1987), specified at the vertical axis of the chart. The corresponding pore throat diameters (x-axis) marked by black arrows define the pore throat diameters (or pore throat lengths of maximal conductance), l_{max} , where all connected paths composed of $l \geq l_{max}$ contribute significantly to the hydraulic conductance (see Sect.3.2).

Deleted: ¶

Appendix C: Euler characteristic¶

The Euler characteristic is a number that describes the structure of a topological space. The most intuitive way to think about the Euler characteristic is in terms of its Betti numbers (β_i):¶

$$\chi = \beta_0 - \beta_1 + \beta_2$$

For a 3D object, β_0 is the number of components, β_1 is the number of inequivalent loops and β_2 is the number of cavities (enclosed voids). In describing the topology of the pore space of a porous rock, it can be assumed that the solid matrix is connected such that $\beta_2 = 0$. In this case, the Euler number reduces to the difference between the number of discrete components and the number of inequivalent loops. If all pore spaces are connected via one pathway or another and assuming that there are no isolated pore spaces, then $\beta_0 = 1$. In a pore network of sandstone that can be modeled as a bundle of tubes, the number of loops β_1 is large, and χ is negative. Therefore, the Euler number, χ , is related to the connectivity of the pore space. As the number of loops decreases, the Euler number becomes less negative and eventually becomes positive, where the system will no longer percolate, according to Vogel (2002).¶

¶

Deleted: D

Deleted: C1

Deleted: .

2781
2782
2783
2784
2785
2786
2787
2788
2789
2790
2791
2792
2793
2794
2795
2796
2797
2798
2799
2800
2801
2802
2803

Appendix C: Setup and results of permeability tensor simulations in sub-samples using GeoDict (module FlowDict)

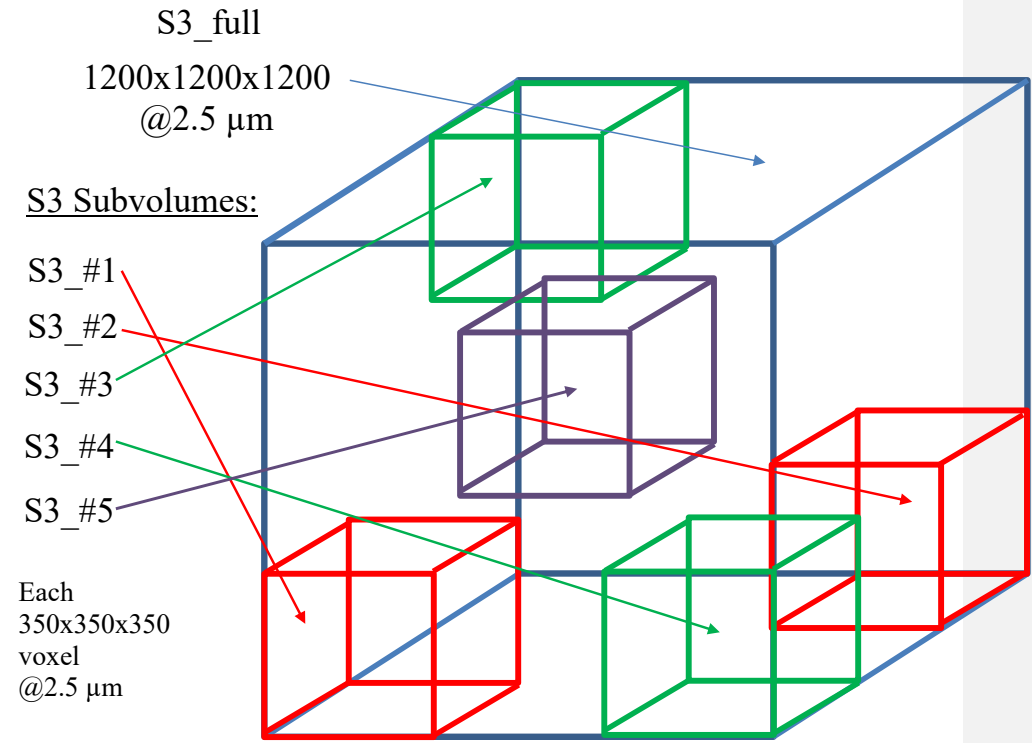


Figure C1: Schematic of sub-volumes location in the full segmented sample of S3.

2804
2805
2806
2807
2808
2809
2810
2811
2812
2813
2814
2815
2816
2817
2818
2819
2820
2821
2822
2823
2824
2825
2826

S3_total

4247	98	116
98	4820	483
117	483	4432

avg. k: ~ 4500 mD
@ ϕ : 26.88 %

S3_#3

5032	9	10
1	4143	10
2	9	5223

avg. k: ~ 4799 mD
@ ϕ : 27.33 %

S3_#1

5485	119	3
130	5882	2
5	1	4504

avg. k: ~ 5290 mD
@ ϕ : 27.47 %

S3_#4

4601	2	3
6	3799	5
4	5	3344

avg. k: ~ 3915 mD
@ ϕ : 26.75 %

S3_#2

4392	179	68
75	3510	185
175	185	3359

avg. k: ~ 3754 mD
@ ϕ : 25.99 %

S3_#5

4397	9	68
10	3825	7
71	5	3858

avg. k: ~ 4027 mD
@ ϕ : 27.53 %

In sub-samples: avg. k: 4381 mD / median k: 4522 mD

Figure C2: Results of permeability tensor simulations using GeoDict (module FlowDict).